



**State of Libya**  
**Ministry of Higher Education**  
**and Scientific Research**  
**University of Benghazi**  
**Faculty of Sciences**  
**Department of Earth Sciences**



**Petrography and Geochemistry of Gargaresh Formation from  
Tajoura to Ras Jdeir, Jifarah plain, NW Libya**

**A thesis**

**Submitted to Department of Earth Sciences**  
**University of Benghazi in Partial Fulfillment of the**  
**Requirements for the Degree of Master of Science in Geology**  
**(Geochemistry)**

**By**

**Mohamed Moftah Omar Buazza**  
**B.Sc. Geology 2009**

**Supervised by**

**Assist. Prof. Osama Shaltami**

Academic Year (2015 – 2016)



جامعة بنغازي  
كلية العلوم  
قسم علوم الارض



الخصائص الصخرية والجيوكيميائية لتكوين قرقارش من تاجوراء الى رأس  
جدير سهل جفارة شمال غرب ليبيا

أطروحة قدمت لقسم علوم الأرض، جامعة بنغازي في تحقيق جزئي لمتطلبات درجة  
الماجستير في علوم الارض (الجيوكيمياء)

بواسطة الطالب:

محمد مفتاح عمر بو عزة

تحت اشراف:

د. أسامة رحيل الشلطي

السنة الدراسية (2015 - 2016)

## المخلص

هذا العمل يهدف لدراسة الخصائص الصخرية والجيوكيميائية لرواسب الحجر الجيري (الكلكارينايت) في الحقب الرابع (تكوين قرقارش) على طول ساحل البحر المتوسط من تاجوراء الى رأس اجدير سهل جفاره شمال غرب ليبيا. تكوين قرقارش يمكن تقسيمه الى عضوين: عضو كعام (العضو الاعلى) وعضو كروت (العضو الاسفل)، كل من هذين العضوين تم تحديدها في منطقته الدراسة، اعلى سمك لعضو كروت في الاجراف البحرية الممتدة من طرابلس الى صبراتة ويقل باتجاه غرب صبراتة. على حسب النسيج والشكل والتراكيب الرسوبية والمحتوى الاحفوري عضو كرووت يمكن تقسيمه الى اربع وحدات، كل الوحدات وعضو كعام ايضا (والتي تتمثل في وحده واحدة فقط) توجد من طرابلس الى صبراتة عدا الوحده الاولى من عضو كرووت تمتد من تاجوراء الى رأس جدير. جيوكيميائيا، اكاسيد الكالسيوم والماغنيسيوم هي المكونات الأساسية لمعدن الكالسيت. السيلكا هي المكون الاساسي لمعدن الكوارتز. احيانا نسب عاليه من السيلكا مع اكاسيد الالومنيوم واليوتاسيوم وجزء من اكاسيد الصوديوم والنتيانيوم والحديد هي المكون الاساسي لمعدن الفلسبار ومعادن الطين. جزء من اكاسيد الصوديوم وعنصر الكلور معا يكونا معدن الهاليت عناصر السترنشيوم والرصاص والعناصر الارضية النادرة مرتبطة بمعادن الكربونات بينما يرتبط كل من النيكل والنحاس والكوبالت والخراسين ارتباطا قويا مع اكاسيد الالومنيوم. يرتبط الثوريوم واليورانيوم ارتباطا قويا وموجبا مع الزكونيوم مما يدل على ان هذه العناصر موجودة في معدن الزيركون. البيانات المؤكسده الساحليه توضحها القيم المنخفضه لليورانيوم مكاني التكوين ونسب العناصر النادرة. عضو كرووت يظهر نمط العناصر الارضية النادره اكثر او اقل من المسطح مع قيمة حيود السيريوم الموجبة والسالبة بينما عضو كعام يظهر نمط العناصر الأرضية النادرة محدب مع القيمه السالبة لحيود السيريوم يدل على ان عضو كعام (العضو العلوي) من ترسيبات ارضيه الاصل و عضو كروت (العضو السفلي) من ترسيبات بحريه الاصل. في عضو كرووت حيود السيريوم يرتبط ارتباطا سالباً مع عنصر الرصاص مما يدل على ان عضو كرووت مترسب في بيئة بحرية ضحلة.

# Dedication

*To the fountain of patience and optimism and hope **my father***

*To each of the following in the presence of God and His*

*Messenger, my mother dear*

*To who has demonstrated to me what is the most beautiful of my  
life my wife*

*To the people who paved our way of science and knowledge*

*All our teachers Distinguished*

*To the taste of the most beautiful moments with my friend*

*Mohamed.M.Buazza*

## ***ACKNOWLEDGEMENT***

First and forever thanks to God for everything. All gratefulness is due to almighty “Allah” the lord of the world who guided and aided me to bring forth this work. Thanks God.

I would like to express my deep thanks to my supervisor, Dr. Osama Shaltami, Assistant Professor of Geochemistry, Department of Earth Science, Faculty of Science, Benghazi University, for his supervision, suggesting the point of research, providing ideas, valuable leading comments, his continuous support and planning of the whole work, and critical reading and reviewing the work.

Special thanks and gratitude are due to Dr. Ahmed El Kawafi, Associated Professor of Paleontology, Department of Earth Science, Faculty of Science, Benghazi University, for his kind assistance in the identification of fossils. Thanks are due to all members of the Department of Earth Science, Cairo University.

Finally, my deepest gratitude must go to my father, my mother, my brothers, my sisters, my wife, my son and my daughter for giving me much valuable assistance and encouragement.

## ABSTRACT

The present work attempts to characterize the petrography and geochemistry of the Quaternary calcarenite (Gargaresh Formation) along the Mediterranean Coast from Tajoura to Ras Jdeir, Jifarah plain, NW Libya. The Gargaresh Formation can be subdivided into two members: Kaam Member (upper member) and Karrot Member (lower member). Both of these members are detected in the studied coast. The Karrot Member on its cliffs on the shoreline of the study area reaches its maximum thickness in the area between Tripoli and Sabratah. It diminishes towards the west of Sabratah. According to texture, morphology, sedimentary structure and fossil content, the Karrot Member could be divided into four units. Except unit 1, all other units are only detected from station no. 2 (Tripoli) to station no. 7 (Sabratah). The Kaam Member is only detected in the area between Tripoli and Sabratah. It is represented by one unit. Geochemically, the major oxides CaO and MgO are the main constituents of the calcite. SiO<sub>2</sub> is mainly in the form of quartz. Sometimes a high quotient of SiO<sub>2</sub> together with the oxides; Al<sub>2</sub>O<sub>3</sub>, K<sub>2</sub>O and partly of Na<sub>2</sub>O, TiO<sub>2</sub> and Fe<sub>2</sub>O<sub>3</sub> are essentially allocated within the structure of the feldspars and clay minerals. Part of Na<sub>2</sub>O and the content of Cl belong mainly to halite. Sr, Pb and REE are basically controlled by the carbonate fraction, while Ni, Co, Cu and Zn are strongly correlated with Al<sub>2</sub>O<sub>3</sub>. Th and U are positively correlated with Zr suggesting that they are contained in zircon. The prevailing well oxidizing coastal environments are well expressed by the low authigenic uranium and low Cu/Zn, Ni/Co and U/Th ratios. Karrot Member shows more or less flat REE pattern with positive and negative Ce anomalies ( $\Delta\text{Ce}$ : 0.68 to 1.45), while Kaam Member shows convex REE pattern with negative Ce anomalies ( $\Delta\text{Ce}$ : 0.86), indicating Kaam Member (upper member) of aeolian origin and Karrot Member (lower member) of marine origin. In Karrot Member,  $\Delta\text{Ce}$  values are negatively correlated with Pb in agreement with shallow marine depositional environments of Karrot Member.

# Contents

<b>Title</b>	<b>Page</b>
<b>- Dedication</b>	<b>I</b>
<b>- Acknowledgements</b>	<b>II</b>
<b>- Abstract</b>	<b>III</b>
<b>- Contents</b>	<b>IV</b>
<b>- List of Figures</b>	
<b>- List of Tables</b>	<b>XIII</b>
<b>1. Introduction</b>	
<b>1.1 Location of the study area</b>	<b>1</b>
<b>1.2 General geomorphology and geology of the study area</b>	<b>2</b>
<b>1.3 Previous Work</b>	<b>8</b>
<b>1.4 Plan and objective of work</b>	<b>11</b>
<b>1.5 Methodology</b>	<b>12</b>
<b>1.5. 1 Sampling</b>	<b>12</b>
<b>1.5.2 Analytical techniques</b>	<b>12</b>
<b>1.5.2.1 Petrographic analysis</b>	<b>12</b>

<b>1.5.2.2 Scanning Electron Microscope</b>	<b>13</b>
<b>1.5.2.3 Loss on Ignition</b>	<b>14</b>
<b>1.5.2.4 Inductively Coupled Plasma-Mass Spectrometry technique</b>	<b>14</b>
<b>2. Regional Geology</b>	
<b>2.1 Introduction</b>	<b>16</b>
<b>2.2 Structural and tectonic setting</b>	<b>16</b>
<b>2.3 Stratigraphic setting</b>	<b>19</b>
<b>2.3.1 Precambrian</b>	<b>19</b>
<b>2.3.2 Paleozoic</b>	<b>21</b>
<b>2.3.3 Mesozoic</b>	<b>22</b>
<b>2.3.4 Cenozoic</b>	<b>23</b>
<b>3. Petrography and Sedimentology</b>	
<b>3.1 Karrot Member</b>	<b>27</b>
<b>3.2 Kaam Member</b>	<b>41</b>
<b>3.3 Morphology of Gargaresh Formation</b>	<b>44</b>
<b>3.3.1 Biogenic calcarenite</b>	<b>44</b>
<b>3.3.2 Non-biogenic calcarenite</b>	<b>45</b>



## **4. Geochemistry**

<b>4.1 Introduction</b>	<b>49</b>
<b>4.2 Statistical Treatment</b>	<b>49</b>
<b>4.3 Major oxides</b>	<b>49</b>
<b>4.4 Trace elements</b>	<b>66</b>
<b>4.4.1 Low field strength elements</b>	<b>66</b>
<b>4.4.2 Heavy metals</b>	<b>67</b>
<b>4.4.3 High field strength elements</b>	<b>70</b>
<b>4.4.4 Rare earth elements</b>	<b>73</b>

## **5. Summary and Conclusions**

<b>Summary and Conclusions</b>	<b>80</b>
<b>References</b>	<b>85</b>

## List of Figures

<b>Fig. No</b>	<b>page</b>
<b>Fig. 1.1: Location map showing the study area and location of the sampled stations</b>	<b>1</b>
<b>Fig. 1.2: Relief map for the study area</b>	<b>3</b>
<b>Fig. 1.3: Landsat image shows the difference between the emerged and submerged shores</b>	<b>4</b>
<b>Fig. 1.4: Aerial photograph shows the irregularity of shoreline which characterizes the emerged shore.</b>	<b>4</b>
<b>Fig. 1.5: High relief shorelines at Al Mayah</b>	<b>5</b>
<b>Fig. 1.6: Example of buildings which are sited above the cliff at Sabratah</b>	<b>5</b>
<b>Fig. 1.7: Landsat image showing the submerged shore</b>	<b>6</b>
<b>Fig. 1.8: Low relief shoreline at Zuwarah</b>	<b>6</b>
<b>Fig. 1.9: Major probable fault system in the study area</b>	<b>7</b>
<b>Fig. 1.10: Geological map of the study area</b>	<b>8</b>
<b>Fig. 1.11: Schematic cross-section showing the general distribution of Quaternary deposits</b>	<b>8</b>
<b>Fig. 1.12: Thin section instrument</b>	<b>13</b>
<b>Fig. 1.13: Scanning electron microscope instrument</b>	<b>13</b>
<b>Fig. 1.14: Loss on Ignition instrument</b>	<b>14</b>
<b>Fig. 1.15: Inductively Coupled Plasma-Mass Spectrometry instrument</b>	<b>15</b>

<b>Fig. 2.1: NE-SW cross-section along the crest of the Jifarah Arch</b>	<b>17</b>
<b>Fig. 2.2: Principal tectonic elements of the Jifarah Arch</b>	<b>18</b>
<b>Fig. 2.3: Pre-Quaternary rocks in the area between west of wadi zarat and east of wadi Ghan</b>	<b>20</b>
<b>Fig. 2.4: Quaternary rocks in Jifarah plain (El Hinnawy and Cheshitev 1975).</b>	<b>21</b>
<b>Fig. 2.5: Pre-Eocene paleogeologic map of the Jifarah Arch</b>	<b>24</b>
<b>Fig. 3.1: Quaternary sequence of the study area</b>	<b>25</b>
<b>Fig. 3.2: Wave cut cliff of calcarenite shows accumulation of gravel and beach sand</b>	<b>26</b>
<b>Fig. 3.3: Wave cut cliff of calcarenite associated with sea stack at Az Zawiyah</b>	<b>26</b>
<b>Fig. 3.4: Generalized lithostratigraphic column of the Gargaresh Formation at Tajoura</b>	<b>27</b>
<b>Fig. 3.5: Generalized lithostratigraphic column of the Gargaresh Formation at Tripoli</b>	<b>28</b>
<b>Fig. 3.6: Generalized lithostratigraphic column of the Gargaresh Formation at Janzour</b>	<b>28</b>
<b>Fig. 3.7: Generalized lithostratigraphic column of the Gargaresh Formation at Al Mayah</b>	<b>29</b>
<b>Fig. 3.8: Generalized lithostratigraphic column of the Gargaresh Formation at Az Zawiyah</b>	<b>29</b>
<b>Fig. 3.9: Generalized lithostratigraphic column of the Gargaresh Formation at El Matered</b>	<b>30</b>
<b>Fig. 3.10: Generalized lithostratigraphic column of the Gargaresh Formation at Sabratah</b>	<b>30</b>
<b>Fig. 3.11: Generalized lithostratigraphic column of the Gargaresh Formation at Marsa Zuwaghah</b>	<b>31</b>
<b>Fig. 3.12: Generalized lithostratigraphic column of the Gargaresh Formation at Zuwarah</b>	<b>31</b>

<b>Fig. 3.13: Generalized lithostratigraphic column of the Gargaresh Formation at Abu Kammash</b>	<b>31</b>
<b>Fig. 3.14: Generalized lithostratigraphic column of the Gargaresh Formation at Ras Jdeir</b>	<b>32</b>
<b>Fig. 3.15: Calcarenite rocks dipping NE at Al Mayah</b>	<b>33</b>
<b>Fig. 3.16: Photomicrographs of grainstone</b>	<b>33</b>
<b>Fig. 3.17: BSE image showing the cement that is completely filling porosity</b>	<b>34</b>
<b>Fig. 3.18: Friable calcarenite overlain by semi-hard calcarenite displays cross bedding at El Matered</b>	<b>34</b>
<b>Fig. 3.19: Hand specimen of unit 2 at Tripoli</b>	<b>35</b>
<b>Fig. 3.20: Photomicrographs of grainstone</b>	<b>36</b>
<b>Fig. 3.21: Moderately hard calcarenite overlain by massive moderately hard calcarenite at Tripoli</b>	<b>37</b>
<b>Fig. 3.22: Photomicrographs of grainstone</b>	<b>37</b>
<b>Fig. 3.23: BSE images showing meniscus cement and isopachous cement</b>	<b>38</b>
<b>Fig. 3.24: Moderately hard calcarenite overlain by wedge shape of massive moderately hard calcarenite at Az Zawiyah</b>	<b>39</b>
<b>Fig. 3.25: Photomicrograph of packstone</b>	<b>39</b>
<b>Fig. 3.26: Photomicrographs of unit 4 from Sabratah</b>	<b>40</b>
<b>Fig. 3.27: Moderately hard calcarenite (Kaam Member) at El Matered</b>	<b>41</b>
<b>Fig. 3.28: Photomicrographs of grainstone</b>	<b>42</b>
<b>Fig. 3.29: Photomicrographs of grainstone</b>	<b>42</b>

<b>Fig. 3.30: Photomicrograph of grainstone</b>	<b>43</b>
<b>Fig. 3.31: BSE images showing isopachous and meniscus cements</b>	<b>43</b>
<b>Fig. 3.32: Tubular voids is a soil filled root molds at Abu Kammash</b>	<b>44</b>
<b>Fig. 3.33: A variety of trails mounds and holes created by unidentified organisms Karrot Member at Az Zawiyah</b>	<b>44</b>
<b>Fig. 3.34: Moderately hard calcarenite by large scale cross beds overlain by teepee structure</b>	<b>45</b>
<b>Fig. 3.35: Moderately hard calcarenite (Karrot Member ) at Janzour</b>	<b>46</b>
<b>Fig. 3.36: Moderately hard calcarenite (Kaam Member) at El Matered</b>	<b>46</b>
<b>Fig. 3.37: Moderately hard calcarenite (Kaam Member) at El Matered</b>	<b>47</b>
<b>Figs. 3.38: Wave-cut cliffs of Karrot Member occupied by large collapsed beach rock slaps</b>	<b>47</b>
<b>Fig. 3.39: Cracks in Karrot Member at El Matered</b>	<b>48</b>
<b>Fig. 4.1: Correlations among the major oxides in the studied samples</b>	<b>62</b>
<b>Fig. 4.2: Relationship between silica and alumina in the study area</b>	<b>63</b>
<b>Fig. 4.3: Relationship between alumina and potash in the study area</b>	<b>64</b>
<b>Fig. 4.4: Relationship between magnesia and lime in the study area</b>	<b>64</b>
<b>Fig. 4.5: Relationship between titanium dioxide and alumina in the study area</b>	<b>65</b>
<b>Fig. 4.6: Relationship between titanium dioxide and iron oxide in the study area</b>	<b>65</b>
<b>Fig. 4.7: Relationship between soda and chlorine in the study area</b>	<b>66</b>

<b>Fig. 4.8: Relationship between Lime and strontium in the study area</b>	<b>67</b>
<b>Fig. 4.9: Relationship between lime and lead in the study area</b>	<b>68</b>
<b>Fig. 4.10: Relationship between alumina and nickel in the study area</b>	<b>68</b>
<b>Fig. 4.11: Relationship between alumina and cobalt in the study area</b>	<b>69</b>
<b>Fig. 4.12: Relationship between alumina and copper in the study area</b>	<b>69</b>
<b>Fig. 4.13: Relationship between alumina and zinc in the study area</b>	<b>69</b>
<b>Fig. 4.14: Relationship between thorium and uranium in the study area</b>	<b>71</b>
<b>Fig. 4.15: Relationship between zirconium and thorium in the study area</b>	<b>71</b>
<b>Fig. 4.16: Relationship between zirconium and uranium in the study area</b>	<b>72</b>
<b>Fig. 4.17: PAAS normalized REE diagram for the studied samples</b>	<b>74</b>
<b>Fig. 4.18: Relationship between lime and total REE in the study area</b>	<b>76</b>
<b>Fig. 4.19: Relationship between Ce-anomaly and uranium in the studied samples</b>	<b>77</b>
<b>Fig. 4.20: Relationship between zirconium and cerium in the studied samples</b>	<b>77</b>
<b>Fig. 4.21: Relationship between thorium and cerium in the studied samples</b>	<b>78</b>
<b>Fig. 4.22: Relationship between Ce-anomaly and lead in the Karrot Member</b>	<b>78</b>
<b>Fig. 4.23: Relationship between zirconium and Eu-anomaly in the studied samples</b>	<b>79</b>
<b>Fig. 4.24: Relationship between thorium and Eu-anomaly in the studied samples</b>	<b>79</b>

## List of Tables

<b>Table No.</b>	<b>Page</b>
<b>Table 4.1: Chemical analysis data of the Gargaresh Formation at Tajoura</b>	<b>50</b>
<b>Table 4.2: Chemical analysis data of the Gargaresh Formation at Tripoli</b>	<b>51</b>
<b>Table 4.3: Chemical analysis data of the Gargaresh Formation at Janzour</b>	<b>52</b>
<b>Table 4.4: Chemical analysis of the Gargaresh Formation at Al Mayah</b>	<b>53</b>
<b>Table 4.5: Chemical analysis data of the Gargaresh Formation at Az Zawiyah</b>	<b>54</b>
<b>Table 4.6: Chemical analysis data of the Gargaresh Formation at El Matered</b>	<b>55</b>
<b>Table 4.7: Chemical analysis data of the Gargaresh Formation at Sabratah</b>	<b>56</b>
<b>Table 4.8: Chemical analysis data of the Gargaresh Formation at Marsa Zuwaghah</b>	<b>57</b>
<b>Table 4.9: Chemical analysis data of the Gargaresh Formation at Zuwarah</b>	<b>58</b>
<b>Table 4.10: Chemical analysis data of the Gargaresh Formation at Abu Kammash</b>	<b>59</b>
<b>Table 4.11: Chemical analysis data of the Gargaresh Formation at Ras Jdeir</b>	<b>60</b>
<b>Table 4.12: Correlation matrix of the studied samples</b>	<b>61</b>
<b>Table 4.13: Descriptive statistics of the studied samples</b>	<b>62</b>

# CHAPTER ONE

## INTRODUCTION

### 1.1. Location of the study area

Northwestern Libya is marked by three main geomorphic units, which include Jifarah plain, scarp and plateau. The present work attempts to characterize the petrography and geochemistry of the Quaternary calcarenite (Gargaresh Formation) along the Mediterranean Coast from Tajoura to Ras Jdeir, Jifarah plain, NW Libya (Fig. 1.1).

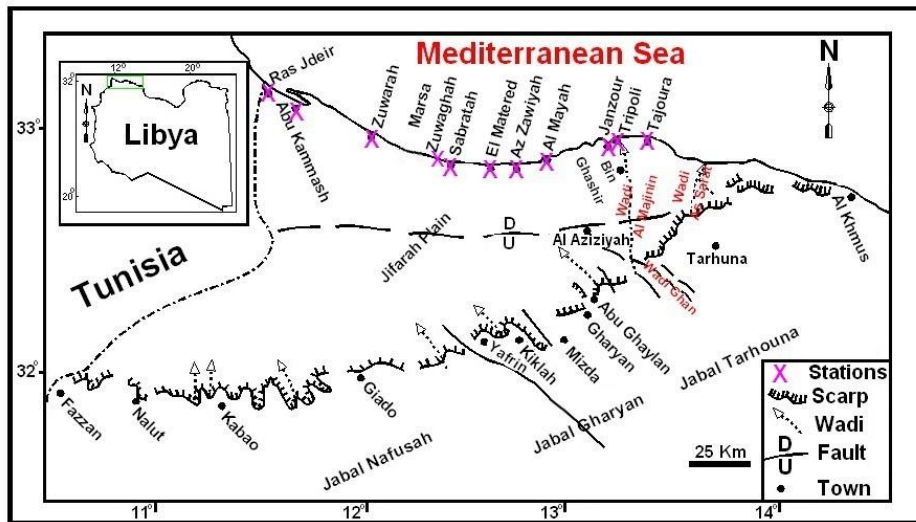


*Fig. 1.1: Location map showing the study area and location of the sampled stations*

The Jifarah plain is a roughly triangular region bounded to the north by the Mediterranean Sea and to the south by a prominent escarpment, Jabal Nafusah. From the east the escarpment drops to meet the coast near Al Khums. The plain widens westward until Libyan-Tunisian borders, for about 20,000 km<sup>2</sup>. It is covered by Pleistocene and Holocene deposits.

The scarp or the Jabal, as known by the native, is one of the common morphological features of northwestern Libya. It runs approximately in an east-west direction, from Al Khums and westwards to beyond the Libyan border. In places, the scarp was given different local names as Jabal Tarhuna (Tarhuna-Gharyan strip), that followed westwards by Jabal Gharyan (Gharyan-Yafrin strip) and Jabal



Nafusah (Yafrin and Nalut strip). The name of Jabal Nafusah is more popular and was frequently applied for all scarps. Jabal Nafusah overlooks the Jifarah plain and has elevation that ranges from 400 to more than 700 m, especially in Gharyan-Yafrin area. The scarp is capped by hard and resistant dolomitic limestone of Upper Cretaceous age, where its slopes are made of Triassic and Jurassic clastic and nonclastic rocks.

The plateau is made of hard and resistant limestone, which belongs to the Cretaceous. It is characterized by gentle dip angles and the elevation ranges from 500-800 m; the low laying areas of the plateau are mainly covered by relative thick sequence of reddish brown Quaternary silts of terra-rossa type, which are mostly cultivated by olives, almond and other vegetations.

In the areas to the southeast of Gharyan, the plateau is covered by volcanic sheets forming flat and broad plains. The northern part of the plateau is highly undulated and is dissected by deep wadis and canyons. Conspicuous black phonolitic hills are noticed on the plateau, they have an average elevation ranging from 500-800 m. The plateau is poorly inhabited and relative small towns are present (e.g., Tarhuna, Gharyan, Mizda, Yafrin, Giado and Nalut).

## **1.2. General geomorphology and geology of the study area**

El Hinnawy and Cheshitev (1975) subdivided the Jifarah plain into three geomorphic subunits. The first subunit is a coastal strip, which is limited to the north by the Mediterranean Sea cliffs and extends landward to about 10-20 km. These cliffs range in elevation from 5 to 30 m, made of calcrete (Jifarah Formation) and calcarenite (Gargaresh Formation). The low topographic areas in this strip are mostly cultivated especially in the area between Tajoura and Al Ajaylat. The area between Al Ajaylat and westwards toward the Tunisian border is covered occasionally by coastal dunes and sabkhas.

The second subunit is a central part that is limited by the southern boundary of the coastal strip and extends to the south for a distance ranges from 60 to 90 km. It rises gradually towards the south to an elevation of 130 m above sea level, where it passes into the foot hills strip. The central part is essentially flat with only minor

topographical changes related to active and stabilized dune fields and a number of wadi courses. Some of the wadis which drain the plateau flow over this part of the Jifarah where they fan out before reaching the sea as wadi As Sarat and wadi Al Majinin.

The third subunit is a foot hill strip; this part is confined to a narrow strip which stretches from the foot of the scarp and northwards to a distance ranging from 10 to 20 km. The Jifarah plain is made, here, of a relatively thick sequence of deposits derived from the scarp which further passes gradually due north into the upper part of the Jifarah sands and silts. In some areas these deposits are capped by a hard calcrete band (El Hinnawy and Cheshitev, 1975). The foot-hill strip is the highest part of the Jifarah plain assuming elevations range from 130 to 200 m above the sea level. This strip is highly dissected by wadis and displays a more rough topography due to outcrops of the Mesozoic rocks which cut through the Quaternary cover.

The study area is a part from the first unit of Jifarah plain which is known as a coastal strip lying between Tajoura and the territorial boundary of Tunisia. The general gradient of the study area is toward northwest as indicated by the constructed relief map (Fig. 1.2).

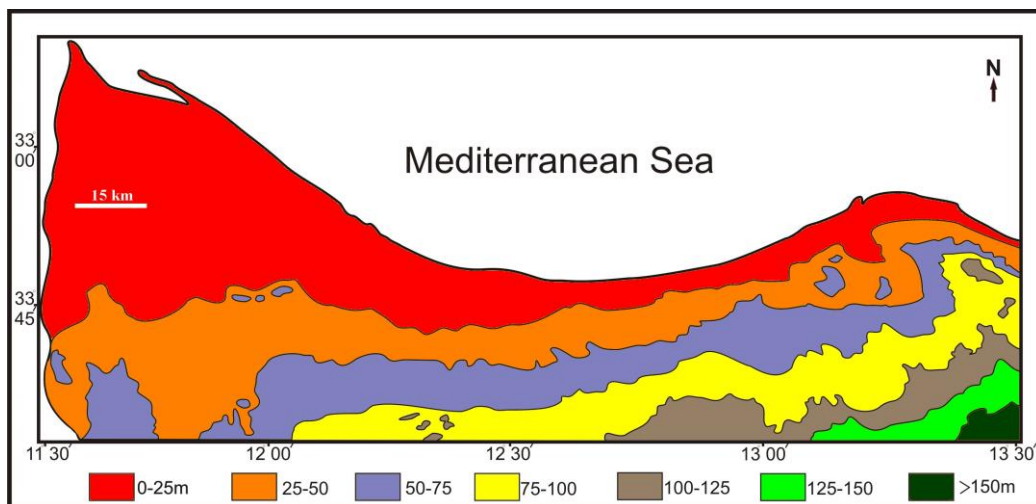


*Fig. 1.2: Relief map for the study area*

Based on the geomorphological characteristics, the studied coastal area can be subdivided into two main physiographic provinces, namely; emerged and submerged shores (Fig. 1.3). The emerged shore extends for about 108 km long, from 5 km east Tajoura (station no. 1) to Marsa Zuwaghah (station no. 8). This area is characterized by irregular shoreline (Fig. 1.4), associated by sea stacks in some places and wave-cut cliffs in others (Fig. 1.5). The wave cut cliffs on the studied area include two formations; Jifarah Formation (calcrete) and Gargaresh Formation (calcarenite).

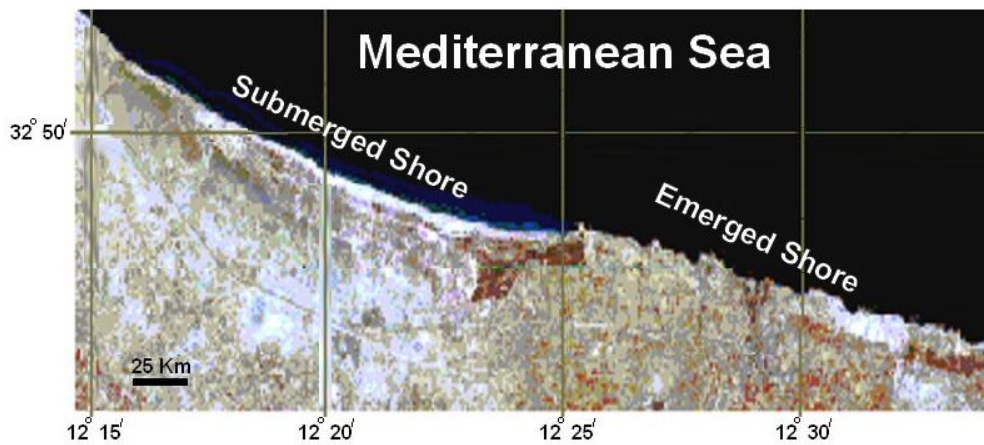


*Fig. 1.3: Landsat image shows the difference between the emerged and submerged shores*



*Fig. 1.4: Aerial photograph shows the irregularity of shoreline which characterizes the emerged shore, (located west Tripoli at co-ordinate 13° 04` E and 32° 59` N)*



*Fig. 1.5: High relief shorelines at station no. 4 (Al Mayah)*

Natural processes such as climate, waves, currents, tides and salt-laden, winds, and wave cause hazards to coastal landstretch and its utilization. Extreme events such as storms, torrents and Tsunami combined with very high tides may cause severe coastal erosion, depleting beaches and threatening buildings and other structures near the shore. Actively eroding cliffs are being progressively cut back, so the coastline is actually receding and consuming land. Roads and buildings which are sited above such cliffs (Fig. 1.6) will eventually be undermined and fall into the sea. Public access and safety must be considered in the management of cliffed coasts.



*Fig. 1.6: Example of buildings which are sited above the cliff at station no.7 (Sabratah), which will be threatening by coastal erosion*

The submerged shore is characterized by its low relief or almost flat coastal area with nearly straight shorelines (Figs. 1.7-8). It extends from Marsa Zuwaghah to the territorial boundary of Tunisia for about 75 km long. This province is characterized by sandy beach, coastal dunes, thin sand sheets, sabkha deposits and scattered patches of Jifarah and Gargaresh formations.

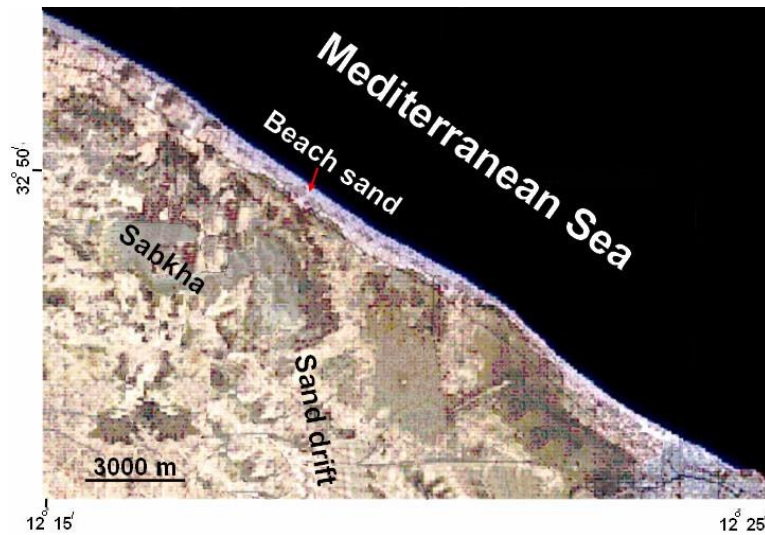


*Fig. 1.7: Landsat image showing the submerged shore*



*Fig. 1.8: Low relief shoreline at station no. 9 (Zuwarah)*

Fig. (1.9) shows that normal fault extending NW–SE with its downthrown toward west is separating the two shore types. Fault zones in which the component faults are arranged en echelon are one of the most characteristic features of Jifarah plain. The zones follow two main trends, E-W and NW-SE. Individual faults are again arranged en echelon, trending either NNE-SSW or NNW-SSE. The Al

Aziziyah fault is one of the coastal faults zones which are mentioned by all previous workers dealing with Tripolitania area. It lies 30 to 40 km south of the present shore line. It crosses the Jifarah plain for a distance of about 100 km extending from Al Aziziyah area to the Tunisian (*see* Fig.1.1). Parallel to the Al Aziziyah fault, Allan (1989) maps reported the presence of another fault line extending from west of Bin Ghashir area to the Tunisian border. It lies 10 km to the south of the present shore line and its downthrown side is towards the north.

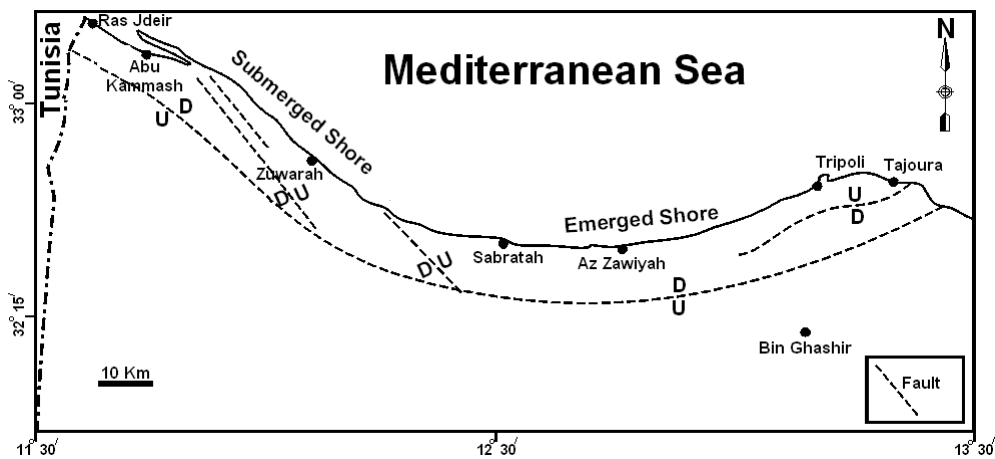


Fig. 1.9: Major probable fault system in the study area

Since the Lower Quaternary to the present, the Jifarah plain is acting as a basin where different types of deposits are distributed (Fig. 1.10, El Hinnaway and Cheshitev, 1975). The sediments reflect different dry and wet phases which predominate over the area during the Quaternary. The post Middle Miocene deposits of Jifarah region have been subdivided by the Industrial Research Centre (I.R.C.) into four formations. The assignment of Al-Assah Formation and the lower member of Qasr Al Haj Formation to the Plio-Pleistocene are based on the assumption that a calcrete which caps these deposits is equivalent to a calcrete dated as Villafranchian in neighboring Tunisia (Fig. 1.11, El Hinnaway and Cheshitev, 1975). Jifarah and Gargaresh formations and the upper members of Qasr Al Haj Formation capped the Plio-Pleistocene deposits. Gargaresh Formation is equivalent to the Strombus Bubonius beds in Italy and Djerba Island in Tunisia. All these deposits have been assigned Pleistocene to Holocene ages which are capped by a veneer of superficial deposits comprising recent sand dunes, wadi sands and

gravels but they are locally capped by coastal and inland sabkhas. All of which have been assigned a Holocene age (El Hinnaway and Cheshitev, 1975).

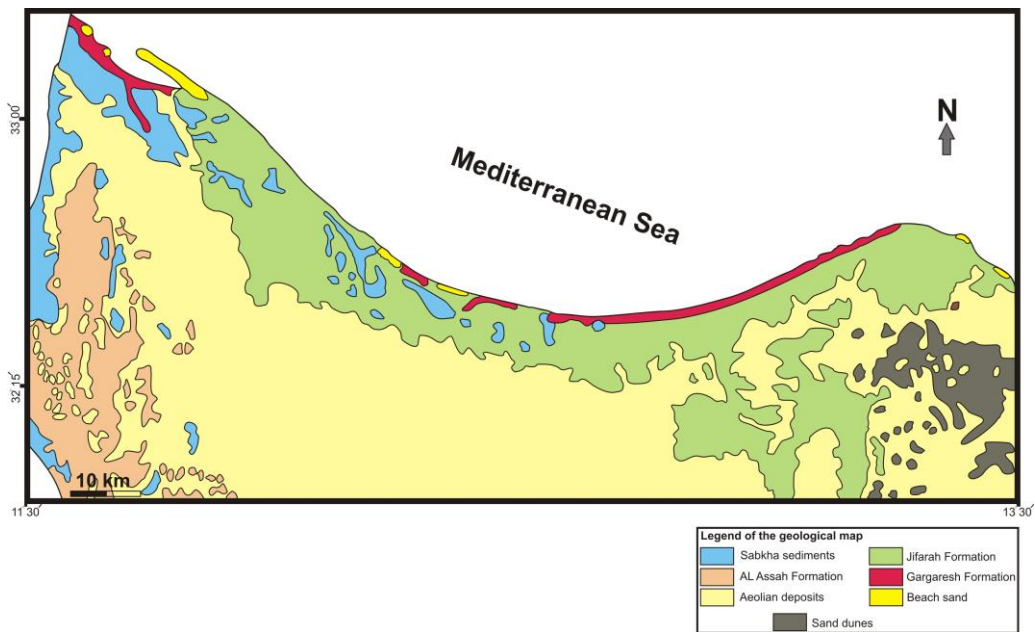


Fig. 1.10: Geological map of the study area

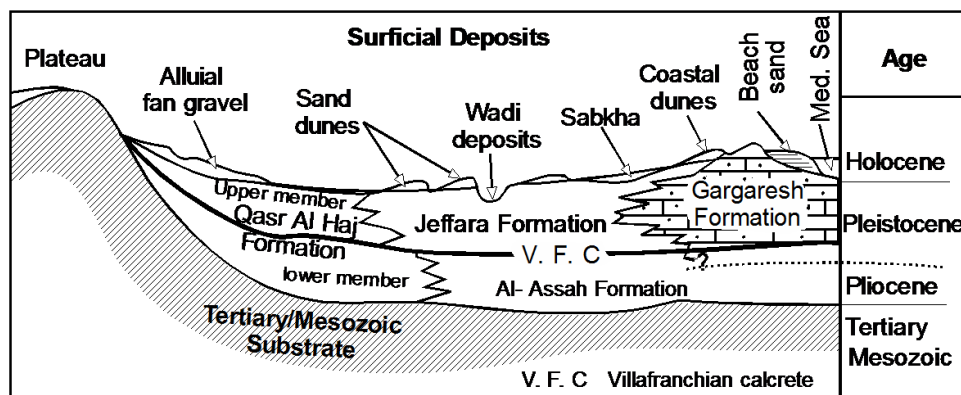


Fig. 1.11: Schematic cross-section showing the general distribution of Quaternary deposits (after Anketell and Ghellali, 1991)

### 1.3. Previous Work

Quaternary studies in the Jifarah Plain are less numerous than those on Mesozoic rocks to the south. Few attentions have been directed towards the northwest Libyan coast. The present thesis attempts to contribute to the available knowledge on the petrography and geochemistry of the Quaternary calcarenite

(Gargaresh Formation) along the Mediterranean Coast from Tajoura to Ras Jdeir, Jifarah plain, NW Libya.

The term Gargaresh Formation was introduced by Lipparini (1940) who was the first to describe the Tyrrhenian coastal deposits from the Tripolitania area. The Stratigraphic Lexicon (Burolet, 1960) named it as Gargaresh Sandstone. Goudarzi (1970) named it as Qarqarish stone and El Hinnawy and Cheshitev (1975) as Gargaresh Formation.

El Hinnawy and Cheshitev (1975) selected the type section of the Gargaresh Formation along the shore to the west of Janzour village (32° 49' N, 12° 55' E), where the formation is approximately 14 m in thickness, but the base is not exposed. They dated the exposed part as Late Pleistocene-Holocene. They mapped the Ajdabiya and Gargaresh formations in the Tripoli area under the name Gargaresh Formation. Francis and Issawi (1977) on the other hand, considered these two units in the Soluq area to be equivalent and mapped them together under the name Ajdabiya Formation. In the other areas along the coast such as in Cyrenaica these units were mapped as marine and aeolian calcarenites (Rohlich, 1974, Klen, 1974).

Mijalkovic (1977) studied the Gargaresh Formation in the Al Qaddahiyah area. He found that Gargaresh Formation occurs along the coastal belt and consists of calcarenites. He added that the presence of *Miliolide* (*Quinqueloculina* spp., and *Triloculina* sp.) confirms shallow marine water, but warm depositional environment. The macro fossils (pelecypods (e.g., *Cardium* (*Cerastoderma*) *edule* Linnaeus and gastropods (e.g., *Bittium* (*Bittium*)) suggest that the Gargaresh Formation deposited mostly in a marine environment of normal or decreased salinity and warm water (from littoral to sublittoral zones). He also added that the fossil content suggests that the Gargaresh Formation was deposited during the Tyrrhenian phase of the Pleistocene.

Giglia (1984) studied the Quaternary formations in the Ajdabiya area. He found that the Ajdabiya Formation is overlain by the Gargaresh Formation.



Anketell and Ghellali (1987) studied stratigraphic aspects of the Gargaresh Formation, Tripolitania, NW Libya. They found that the Gargaresh Formation is shown to be comprised of six units each of which is made up from cross-bedded calcarenite dunes of aeolian origin resting on localized lenses of marine gravels and shallow-dipping, cross-bedded calcarenite of littoral type. The surfaces on which the marine deposits at the base of each member rest are surfaces of discontinuity cut by wave action. Landwards, the surfaces are shaped by fluvial and aeolian erosion, soil formation and solution and delimit an equivalent number of members in quartzose silts of fluvio-aeolian origin making up the Jifarah Formation. Shorewards the Jifarah silts grade into, interdigitate with and, commonly, lap onto the marine deposits so that that within each depositional unit there is an overall sense of progradation reflecting advance of continental facies in response to falling sea level. A progressive seawards stacking of dune deposits with decreasing age suggests that progradation appears to have occurred at formational level also. However, while this may be true, the various elevations of the fossil beach deposits suggest that decreasing age of sea level high stands is not matched by decreasing altitudes, instead, high stands both higher and lower than present day sea level were involved in the overall drop. The possibility that variation in beach elevations may, however, reflect the influence of tectonic uplift and/or downwarp is also noted.

Anketell and Ghellali (1991) studied the Quaternary sediments in the Jifarah Plain. They found that these Quaternary sediments consist of three formations: the Qasr Al Haj Formation, the Jifarah Formation and the Gargaresh Formation. They added that these formations are equivalent and represent a south to north change in facies from alluvial fan gravels near the Jabal Nafusah to fluvio-aeolian sands and silts to aeolian calcarenites and littoral sands and gravels in the coastal areas.

Khomiara (2013) studied the Quaternary coastal deposits between Tripoli and Musrata, Libya. He found that the pre-Quaternary substrate is represented by Cenomanian dolostone (the Sidi As Sid Formation, Ain Tobi Dolostone Member) and/or Middle Miocene limestone (the Al Khums Formation). The Jifarah Formation begins with shallow marine facies, moderately to well cemented massive sandy limestones and sandy conglomerates; followed by well developed cyclic repetition of nodular and platy calcretes. The Gargaresh Formation starts with

marine cross-bedded bioclastic sandstone to sandy limestone, locally with abundant disarticulated marine bivalves. The shallow marine facies is separated from the overlying paleosol by a well defined erosional surface. Both the Pleistocene Jifarah and Gargaresh formations in most of the examined coastal exposures are overlain by Holocene soils and dunal sand.

Hlal and Bennur (2014) studied the sedimentology and stratigraphy architecture of the Late Pleistocene-Holocene succession of the Gargaresh Formation, Sabratah Basin, NW Libya. They found that the Gargaresh Formation outcrop (between Misurata to Tripoli) is represented by prominent carbonate aeolianite exposed in extensive outcrops along the NW Libyan shoreline. Gargaresh Formation outcrop is represented by two Members; Kaam Member (upper member) of aeolian origin and Karrot Member (lower member) of marine origin. It is forming low ridges and cliffs along the coastline of NW Libya and occurs as cliffs continuously attached to the sea tide and occasionally interrupted by broad wadis or deep-cut embayment. The Gargaresh Formation sediments are dominated by calcarenite with skeletal marine fauna and non-skeletal grains of lithoclasts, aggregate, with oolites. In addition, these rocks are characterized by very well aeolian controlling factors represented by wind blown sediments such as large scale cross lamination (aeolianite) . The majority of paleocurrent direction was to SE, on the other hand the dune migration was SE also. Gargaresh Formation sediments show that the original aragonite composition of pelecypods and gastropods fragments are mostly preserved, but partly transformed into granular calcite.

#### **1.4. Plan and objective of work**

The work is done according to the following plan:

- 1) Sampling of the Quaternary calcarenite.
- 2) Petrographic analysis using petrographic microscope and Scanning-Electron Microscope (SEM) investigations.
- 3) Chemical analysis of major oxides and trace elements using Inductively Coupled Plasma Mass Spectrometry (ICP-MS) technique.
- 4) Summary and conclusions.

The work is done to achieve the following:

- 1) To delineate the geologic and geomorphic setting of the study area along traverses extending towards the inland.
- 2) To study the petrography of the Quaternary calcarenite.
- 3) To discuss the depositional environment and paleo-oxygenation of the Quaternary calcarenite.

## **1.5. Methodology**

### **1.5.1. Sampling**

Samples are collected from the Quaternary calcarenite (Gargaresh Formation) along the Mediterranean Coast from Tajoura to Ras Jdeir, Jifarah plain, NW Libya, from 11 stations (about 71 samples). The traverse is parallel to the studied coast.

### **1.5.2. Analytical techniques**

#### **1.5.2.1. Petrographic analysis**

This analysis was done in the Central Laboratories of the Geological Survey of Egypt in Cairo (Fig. 1.12) Petrographic analysis involves taking a sample from field, fixing it to a glass slides, grinding the sample to 0.003 mm, thick (thin section) and observing to polarizing microscope this technique derived from the earth sciences, where it used to identify minerals and textures in the rock. The samples were examined to determine differential sedimentological and diagenetical features according to Dunham classification (1962). The following is, however summary of the preparation:

- 1) Cut the rock with the stone saw.
- 2) Sawing the rock sample.
- 3) Fixing the rock on object slide.
- 4) After cutting the rock, it is grinded to a thickness of 25  $\mu\text{m}$ .
- 5) Polishing the thin sections.



*Fig. 1.12: Thin section instrument*

#### **1.5.2.2. Scanning Electron Microscope (SEM)**

A scanning-electron microscope, housed at the Nuclear Materials Authority of Egypt, has been used in the present study. The scanning electron microscope (SEM) uses a focused beam of high-energy electrons to generate a variety of signals at the surface of solid specimens. The signals that derive from electron-sample interactions reveal information about the sample including external morphology (texture), chemical composition, and crystalline structure and orientation of materials making up the sample. The SEM is also capable of performing analyses of selected point locations on the sample (Fig 1.13).



*Fig. 1.13: Scanning electron microscope instrument*

### 1.5.2.3. Loss on Ignition (LOI)

Loss on Ignition (LOI) analysis is used to determine the organic matter content (OM %) of the studied samples. It does not involve the use of any chemicals, only the use of a muffle furnace. LOI calculates OM % by comparing the weight of a sample before and after the soil has been ignited. Before ignition, the sample contains OM, but after ignition all that remains is the mineral portion of the soil. The difference in weight before and after ignition represents the amount of the OM that was present in the sample (Fig 1.14). The analysis was done in the Nuclear Materials Authority of Egypt. The following is, however summary of the preparation:

- 1) Weight the crucible empty.....A.
- 2) Weight the crucible + sample .....B.
- 3) Install B into oven and heated up to 1000° for an hour.
- 4) Weigh the crucible after heating .....C.
- 5)  $A - B = \text{weigh of sample}.....D.$
- 6)  $\text{Weight loss} = B - C = E.$
- 7)  $\text{LOI} = E / D \cdot 100.$



*Fig. 1.14: Loss on Ignition instrument*

### 1.5.2.4. Inductively Coupled Plasma-Mass Spectrometry technique (ICP-MS)

About 10 major oxides and 23 trace elements are analyzed by the ICP-MS technique (Fig. 1.15), which is widely used, at present, for determination of elements in various materials with high precision. The analytical procedure depends on the decomposition of exact weight of 0.2 g powdered fine sand size sample in 50 ml Teflon beaker. Decomposition was done by 4 ml  $\text{HNO}_3$ , 3 ml  $\text{HClO}_4$  and 5 ml HF, and evaporated to dryness under 200°C. The residue was dissolved with 5 ml

(1:1)  $\text{HNO}_3$  by heating and 5 ml of 4 ppm indium solution was added as an internal standard. The sample, as well as reference, solutions were introduced by peristaltic pump with 0.18 rpm. Before each measurement, nebulizer and spray chamber were washed by introducing the solution for 3 min with 0.5 rpm and 30 seconds with 0.18 rpm. The analysis was done in the Nuclear Materials Authority of Egypt. The obtained data are given in tables (4.1-11).



*Fig. 1.15: Inductively Coupled Plasma-Mass Spectrometry instrument*

## **CHAPTER TWO**

### **REGIONAL GEOLOGY**

#### **2.1. Introduction**

The Jifarah Arch is a prominent structural feature of central North Africa which partly underlies the Jifarah plain in NW Libya and SE Tunisia and partly extends to the offshore area. It is located roughly between latitudes 32"N and 34"N and longitudes 10"E and 14"E. Today the exposed part of the arch is outlined by a continuous carbonate scarp of Late Cretaceous age. This scarp forms a horseshoe shaped cliff that extends from Al Khums in the east to Gabes in the west (*Hammuda, 2000*).

Prior to petroleum exploration activities in Libya and Tunisia, most studies concentrated on the exposed parts of the Jifarah Arch, namely its rimming horseshoe scarp which exhibits oversimplified structures. However, subsurface data from oil wells has revealed that the Jifarah Arch is structurally complex, the complexity being hidden under Neogene sediments (Fig. 2.1) (*Hammuda, 2000*).

Available data from these wells, along with recent developments in rift tectonics, have made it possible to propose a hypothesis explaining the origin of the Jifarah Arch. In addition this explanation should have other geological implications regarding the accumulation of organic matter in the area (*Hammuda, 2000*).

#### **2.2. Structural and tectonic setting**

The main tectonic elements of the Jifarah Arch are summarized in Fig. 2.2. They include the older Caledonian orogenic elements, manifest in the Tibesti-Tripoli Uplift, the Tunisian N-S axis, and the Late Paleozoic Hercynian orogenic elements mainly in an E-W direction. These are the Gharyan-Algerian high, the Dahar, and the Carboniferous-Permian hinge line. The Late Mesozoic to Early Cenozoic tectonics resulted in the Permian hinge line becoming prominent, with consequent extensive subsidence in the offshore basin during Permian and Triassic time. This tectonic subsidence resulted in thick accumulations of sediments in the offshore area while on the Jifarah Arch itself the Permian is missing. However, the

Triassic is more or less of intermediate thickness. By Early Eocene time this imbalance in the sedimentary thickness, namely being thick in the offshore area and thinner on the Saharan platform, was accompanied by excessive subsidence which resulted in the development of step-faulting (*Hammuda, 2000*).

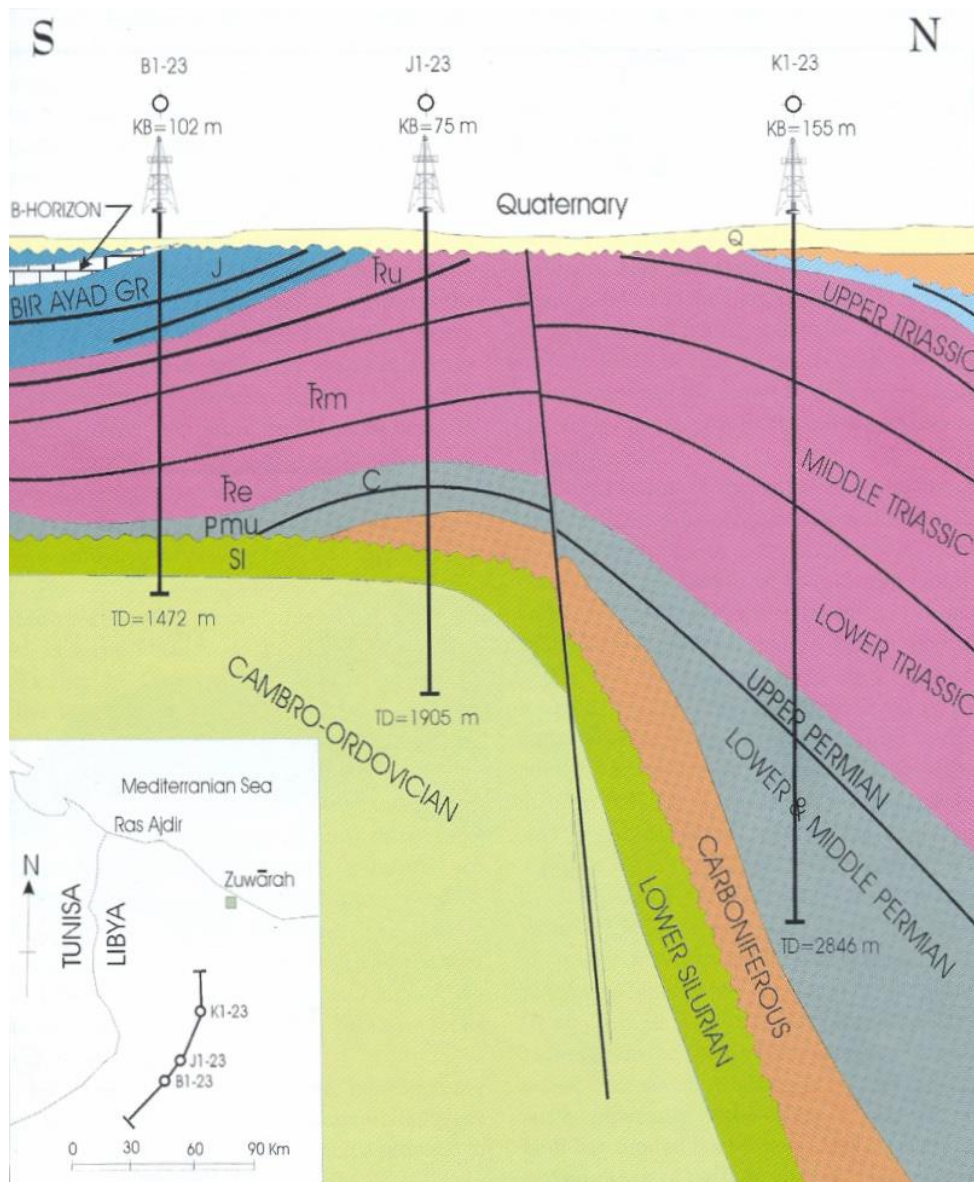


*Fig. 2.1: NE-SW cross-section along the crest of the Jifarah Arch in the faulted continental margin, showing the sedimentary sequence from Early Paleozoic to Quaternary as penetrated by drilling and the major tectonic fracture along the Permian hinge line (after Hammuda, 2000)*



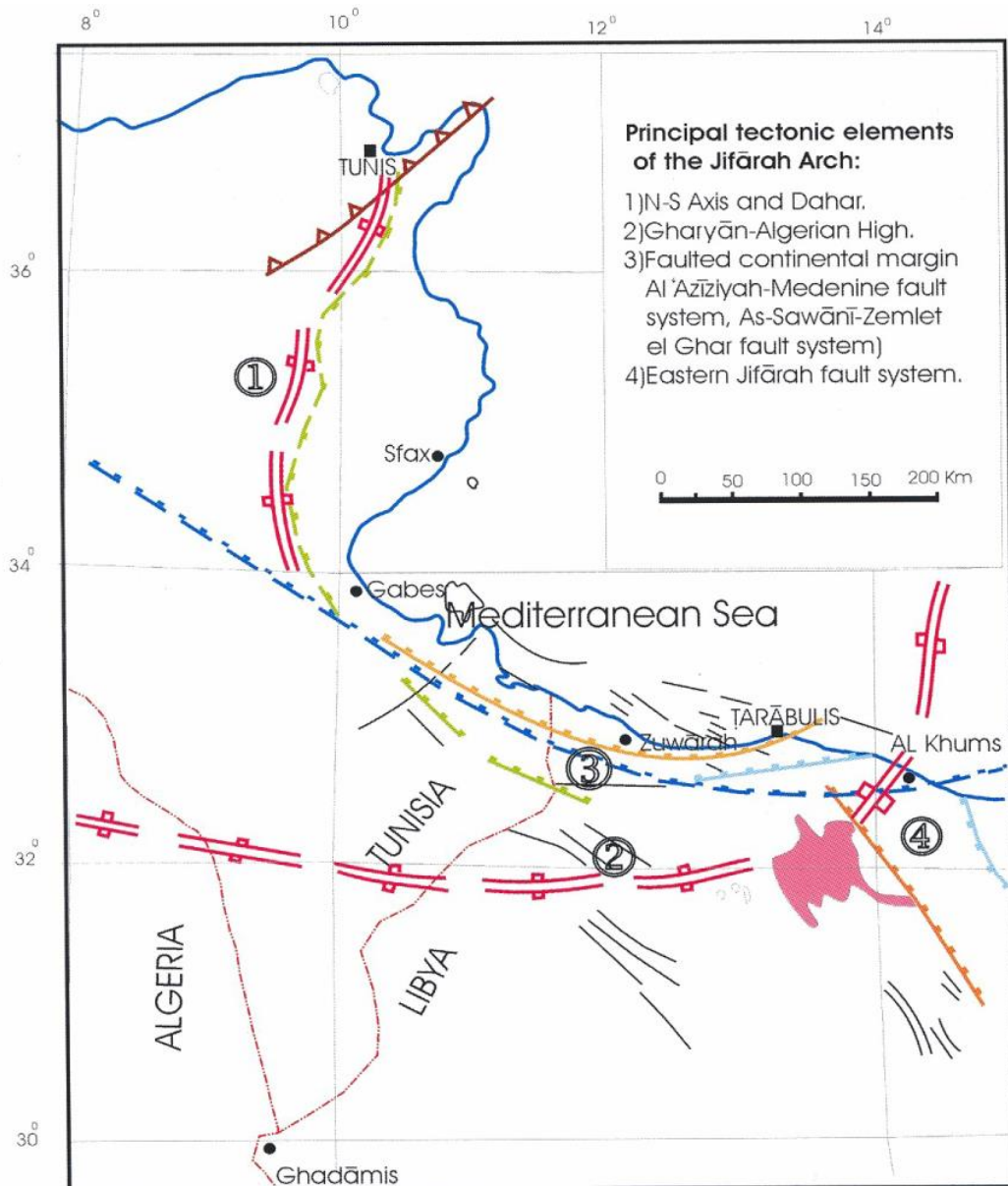


Fig. 2.2: Principal tectonic elements of the Jifarah Arch (after Hammuda, 2000)

In pre-Eocene time, extension faulting resulted in a normal fault in the offshore area which controlled sedimentation of the Lower Eocene nummulitic facies and limited its deposition to the offshore area north of the Jifarah Arch. Continuation of the uplift of the Saharan platform, along with the subsidence and accumulation of sediments in the offshore basin, has resulted in another extension fault along the margin of the African Continent which affected the Jifarah Arch south of the present shoreline, namely the As Sawani fault. Relative movements along this fault to the west extend to the Zemlet el Ghar fault system (Ben Ismail and M'Rabet, 1990). This fault system changes from a normal fault, where the

downthrown side is the northern side in As Sawani fault, to a normal fault where the downthrown side is the southern side in Zemlet el Ghar fault. This pattern forms a graben with A1 Aziziyah fault south of Mednine. This extension faulting forms scissor-type wrench faulting when viewed in an E-W direction (*Hammuda, 2000*).

In pre-Miocene time, A1 Aziziyah fault probably developed due to the continuation of the uplift in the Gharyan high and to the accumulation of very thick sediments in the Jifarah offshore areas. This fault has been active ever since, resulting in further subsidence to the north, especially in the offshore area. In addition, this fault has limited the Miocene sedimentation to the north and northeast of the fault and has exposed the areas to the south and southwest to extensive erosion. This erosion has resulted in the retreat of the A1 Aziziyah fault scarp by over 30 km to the south along the A1 Aziziyah-Gharyan line. Accordingly, the rate of retreat of this scarp, in an N-S direction, has been estimated at about 2 mm per year. The Western Jabal scarp has been described by Miller (1971) as a retreating fault line scarp. However, recent structural evidence suggests that the scarp can be attributed, in addition, to other factors which include erosion resulting from uplift of the Jifarah Arch. Other faults of smaller magnitude have resulted in smaller tectonic trends which are of local exploratory importance (*Hammuda, 2000*).

### **2.3. Stratigraphic setting**

The stratigraphic column overlying the Precambrian crystalline basement in the Jifarah area includes sequences of marine and non-marine rocks ranging in thickness from about 1500 m on the Saharan platform to over 5000 m in the offshore basins. (Figs.2.3-4) show the pre- and Quaternary deposits in Jifarah plain (El Hinnawy and Cheshitev 1975).

#### **2.3.1. Precambrian**

The Precambrian rocks under the Jifarah Arch in both Libya and Tunisia include igneous granites and granodiorites, metamorphic phyllites and schists and sedimentary conglomerates.

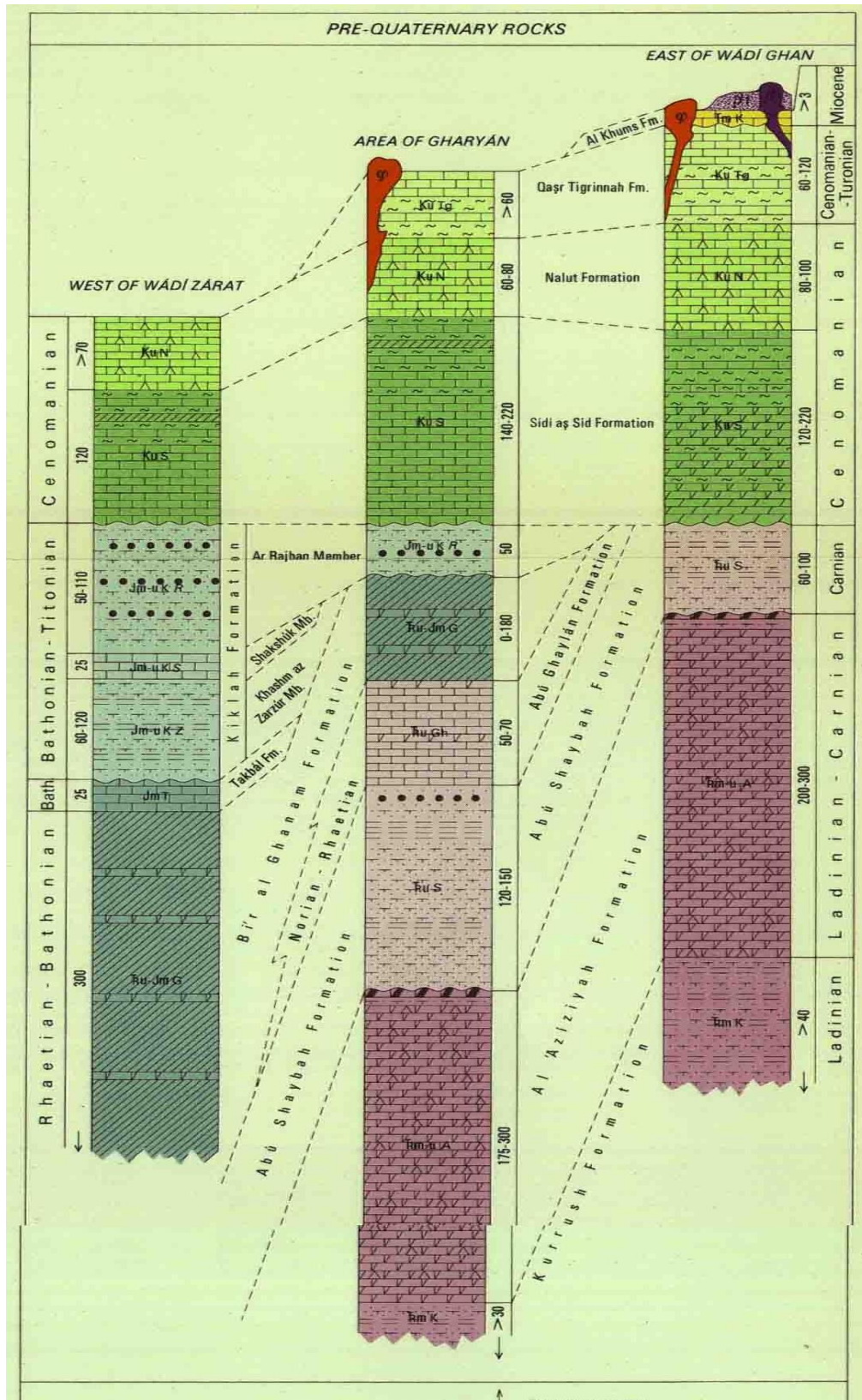


Fig. 2.3: Pre-Quaternary rocks in the area between west of wadi zarat and east of wadi Ghan (El Hinnawy and Cheshitev 1975).

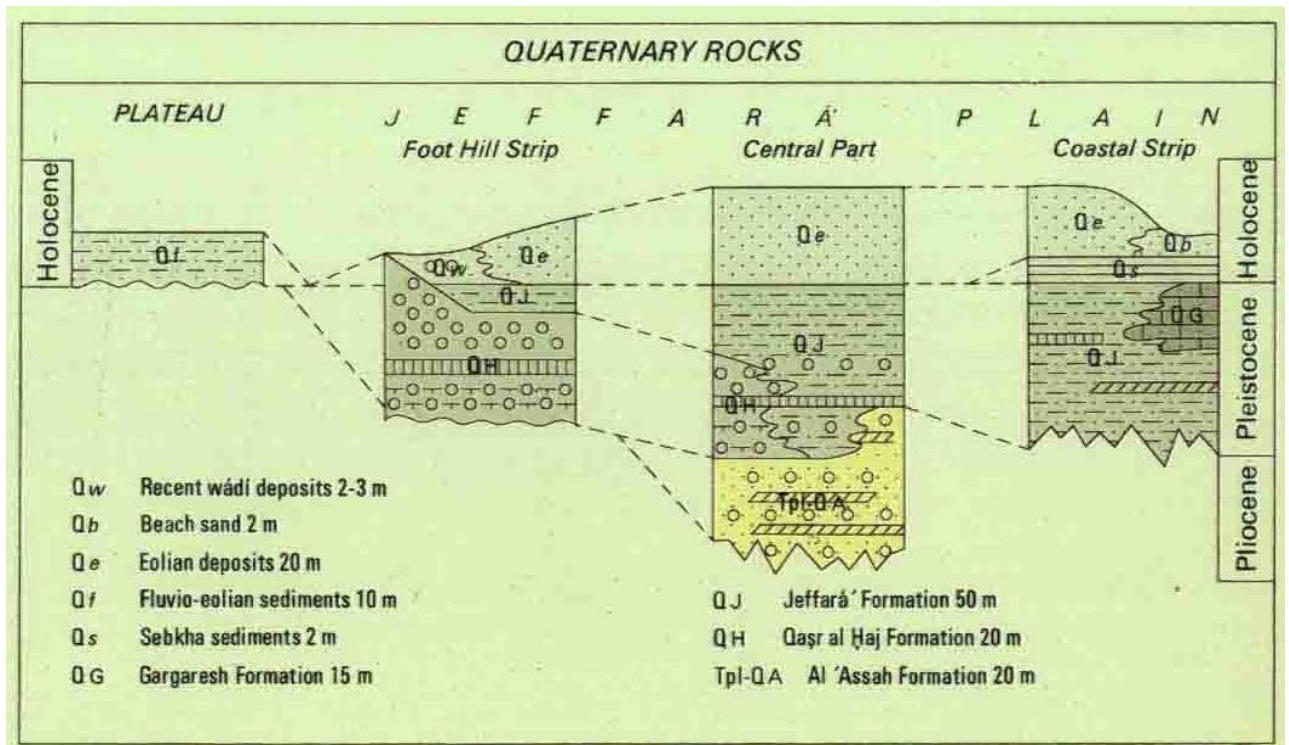


Fig. 2.4: Quaternary rocks in Jifarah plain (El Hinnawy and Cheshitev 1975).

These rocks range in depth from 600 m on the Tripoli nose, which forms an extension of the Tibisti Uplift extending to more than 5000 in Tarabulus Basin offshore (Hammuda, 2000).

### 2.3.2. Paleozoic

The Paleozoic rocks, as reported from exploration wells in the area, represent sequences of epicontinental environments alternating with shallow marine and continental deposits (Hammuda, 2000).

The Cambro-Ordovician rocks include non-fossiliferous burrowed quartzitic sandstones and quartzites which directly overlie the crystalline basement. The sandstones may contain *Tigillites* (Hammuda, 2000).

The Lower Silurian is represented by a transgressive sequence of the Tanezzuft graptolitic silty shales. These shales are widespread in other basins and

form the source beds for most Paleozoic basins. However, the Upper Silurian Acacus Sandstone is missing on the crest of the arch but is found in Ghadames Basin up to the margin of the arch (*Hammuda, 2000*).

The Devonian is also missing in the Jifarah Arch, which is due either to erosion or non-deposition on the Caledonian paleohigh (*Hammuda, 2000*).

The Carboniferous sediments are marked by a transgressive sequence from the north where shallow marine shales, sandstones, dolomites, and evaporates predominate. These beds on the Jifarah Arch cover unconformably the Cambro-Ordovician or Lower Silurian deposits. Most of the Carboniferous sediments were stripped from parts of the Jifarah Arch and from the Gharyan high during the Hercynian movement (*Hammuda, 2000*).

The Permian seas transgressed from the north where the Permian sedimentary thickness thins over the Jifarah Arch and thickens in the offshore basins. These beds directly overlie the Carboniferous over the Jifarah Arch but are missing in the subsurface of the Western Jabal. On the arch the Upper Permian facies of sandstones, shales and carbonates unconformably overlie the Lower Permian clastics. Since Permian time crustal thinning which accompanied the continental drift between Africa and Eurasia has resulted in active subsidence of the offshore basin along the margin of the African land mass. In this offshore basin Permian, Triassic, and Jurassic sediments thickened toward the north(*Hammuda, 2000*).

### **2.3.3. Mesozoic**

The Lower Triassic sediments consist of graywacke, clastics and shallow marine shales. The Middle Triassic sediments include alternation of marine shale carbonates and non-marine clastics. Among these facies there are sequences of red beds and evaporites, along with lateral variations of carbonate facies. These evaporites later contributed to salt doming in the offshore area through salt tectonics (*Hammuda, 2000*).

The Jurassic strata consist of alternating shallow marine, transitional and continental facies where sandstones, shales, anhydrites, carbonates and gypsum were deposited. These Triassic and Jurassic sequences are thin over the Saharan platform, increase in thickness toward the north where they reach several hundred meters on the Jifarah Arch, and over 1500 m in the offshore basin (*Hammuda, 2000*).

Cretaceous rocks are missing from the centre of the Jifarah Arch. However, the eroded horseshoe scarp rimming the Jifarah plain indicates that the Lower Cretaceous sediments were continental where uplift extended to the Jifarah Arch from the Western Jabal. In Late Cretaceous time, Upper Cretaceous rocks which form the cap on the Dahar and Western Jabal escarpment were deposited in shallow marine environments on the Saharan platform, and gradually changing facies in the offshore basins (*Hammuda, 2000*).

#### **2.3.4. Cenozoic**

Paleocene sediments were probably deposited in the Jifarah area as a continuation of the Upper Cretaceous sequence. During the Eocene, uplift in both the Jifarah Arch and the Western Jabal and parts of the Dahar have resulted in removal of Cretaceous and Paleocene sediments and parts of the Jurassic beds (*Hammuda, 2000*).

From Eocene time on sedimentation on the Jifarah Arch and in the offshore basin was controlled by step-faulting. The Eocene sequence is limited by an offshore step-fault. The Oligocene sediments were also controlled by the As Sawani fault to the south, and the Middle Miocene sediments by the A1 Aziziyah fault which extends to Mednine and beyond to the west. A1 Aziziyah fault forms the southern limit of Middle Miocene rocks in the Jifarah plain (Fig. 2.5). During Pliocene and Pleistocene time, interfingering of continental and littoral deposits accumulated over eroded Mesozoic and Miocene deposits and continued to the present (*Hammuda, 2000*).

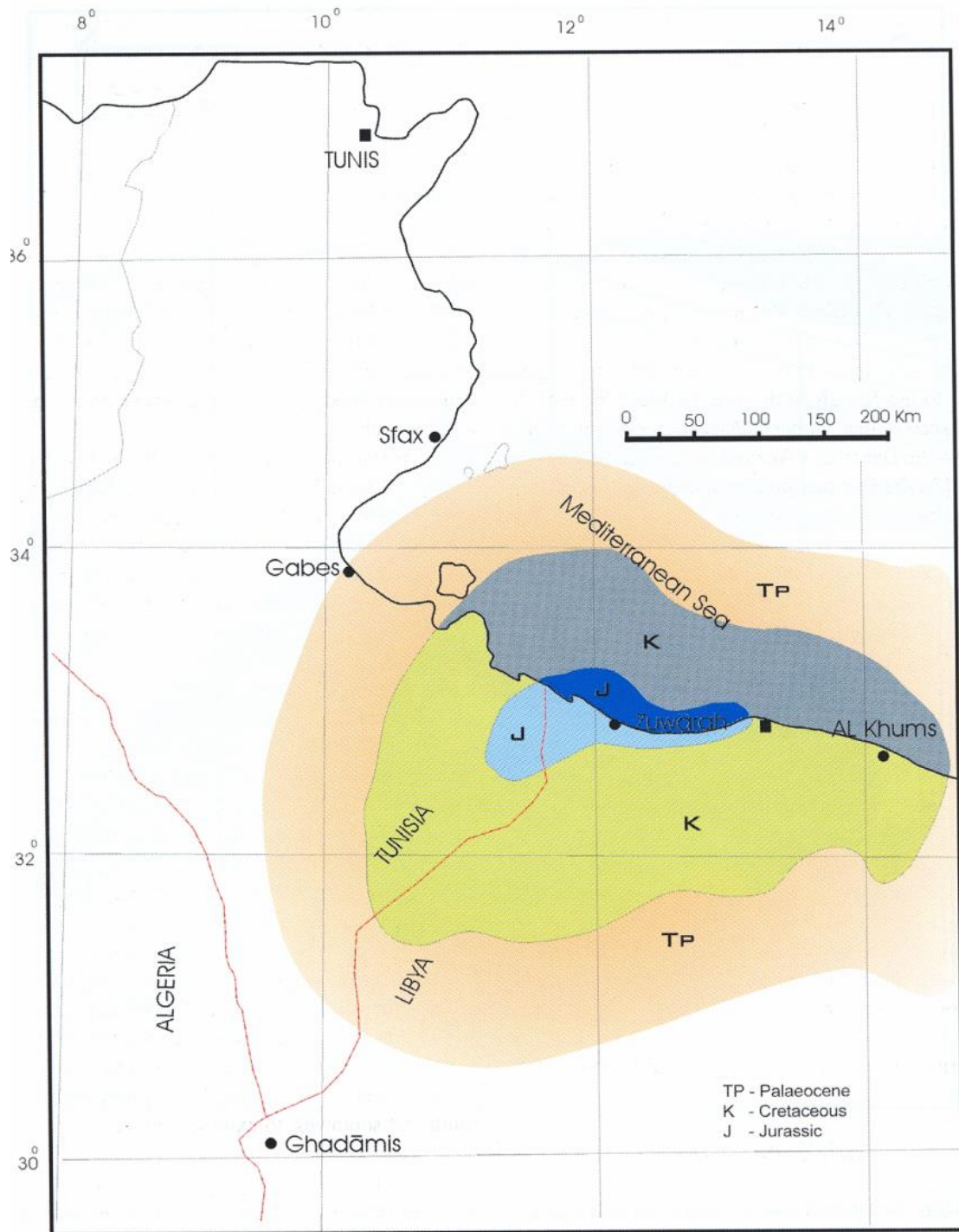


Fig. 2.5: Pre-Eocene paleogeologic map of the Jifarah Arch (after Hammuda, 2000)

## CHAPTER THREE

### PETROGRAPHY AND SEDIMENTOLOGY

About 71 representative samples from the study area were examined for better understanding of their nature, origin and diagenetic history. Petrographic studies comprise microscopic investigations of thin sections and scanning electron microscope (SEM). Microfacies study is achieved following the schemes of Dunham (1962).

The sequence of the Quaternary sediments along the study area is shown in Fig. (3.1). From field investigations the area of Gargaresh Formation make most steep cliffs along the shore of the Mediterranean stretching from Tajoura in the east to Ras Jdeir in the west (Figs. 3.2-3).

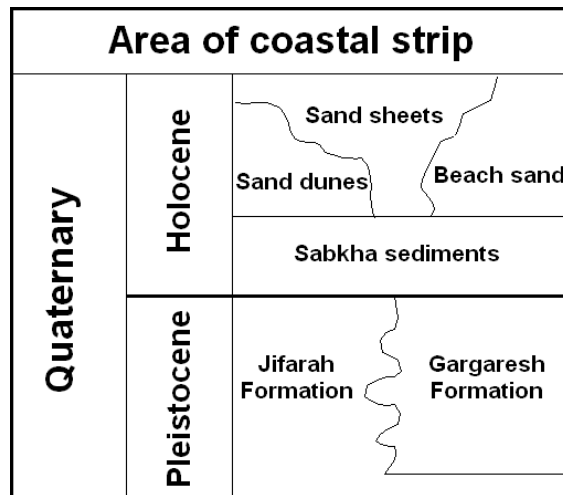


*Fig. 3.1: Quaternary sequence of the study area (after El Hinnaway and Cheshitev, 1975)*



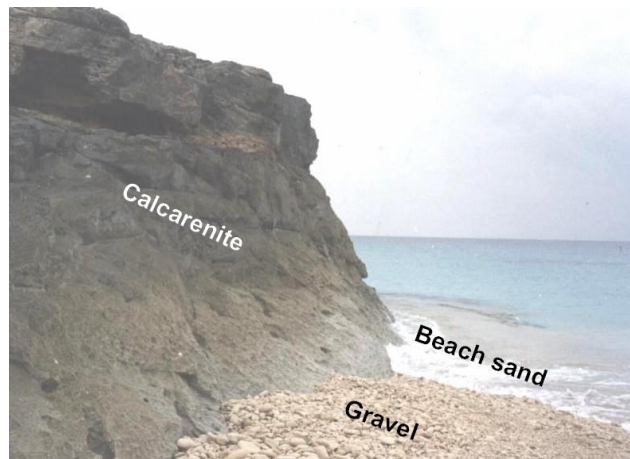


*Fig. 3.2: Wave cut cliff of calcarenite shows accumulation of gravel and beach sand at station no. 4 (Al Mayah)*



*Fig. 3.3: Wave cut cliff of calcarenite associated with sea stack at station no. 5 (Az Zawiyah)*

The fossil content suggests that the Gargaresh Formation was deposited during the Tyrrhenian phase of the Pleistocene (Mijalkovic, 1977). According to Hlal and Bennur (2014) the Gargaresh Formation can be subdivided into two members: Kaam Member (upper member) of aeolian origin and Karrot Member (lower member) of marine origin. Both of these members are detected in the studied coast.

### 3.1. Karrot Member

The Karrot Member on its cliffs on the shoreline of the study area reaches its maximum thickness in the area between Tripoli and Sabratah. It diminishes towards the west of Sabratah. According to texture, morphology, sedimentary structure and fossil content, the Karrot Member could be divided into four units.

**Unit 1:** It is the oldest unit (unexposed base). It is detected in all stations (Figs. 3.4-14). In the field, it is hard and range in color from yellowish gray to yellow. This unit is composed essentially of pellets, lumps, shell fragments and abundant fossils. This unit consists of laminated, graded bedded and considered to be deposited under shore environment. Most outcrops of this unit are dipping seaward and are considered as beach rock (Fig. 3.15). Microscopically, the allochems of this unit are composed of fossils, fossil fragments, pellets and intraclasts with ooids coated by micrite. These are characterized by moderately sorted, medium to coarse grained, well rounded, isopachous and meniscus cements and intergranular porosity (< 5%). The fossil content involves foraminifera (mainly *Elphidium*, *miliolid* and other *rotalid*), bivalve and gastropod shells, echinoderm plate and spine, coralline red algae, bryozoan and ostracoda (Fig. 3.16). The extensive cementation processes such as isopachous bladed calcite crystals growing towards center of pores reduced the porosity (Fig. 3.17).


Series	Stage	Formation	Member	Unit	Thick(m)	Lithology	Hardness	Description
Pleistocene	Tyrrhenian	Gargaresh	Karrot	1	1		S M H	Yellow hard fossiliferous calcarenite

Fig. 3.4: Generalized lithostratigraphic column of the Gargaresh Formation at station no. 1 (Tajoura)

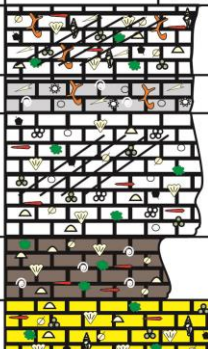
Series	Stage	Formation	Member	Unit	Thick(m)	Lithology	Hardness	Description
<i>Pleistocene</i>	Tyrrhenian	<i>Gargaresh</i>	kaam	1	4		S M H	White, moderately hard, cross bedded calcarenite
			Karrot	4	1			Massive, moderately hard, calcarenite with helix
				3	5			White, moderately hard, cross bedded calcarenite
				2	2			Brown, friable, calcarenite with helix
				1	2			Yellow, hard, fossiliferous calcarenite

Fig. 3.5: Generalized lithostratigraphic column of the Gargaresh Formation at station no. 2 (Tripoli)


Series	Stage	Formation	Member	Unit	Thich(m)	Lithology	Hardness	Description
<i>Pleistocene</i>	Tyrrhenian	<i>Gargaresh</i>	kaam	1	5		S M H	White, moderately hard, cross bedded calcarenite
			Karrot	4	4			Massive, moderately hard, calcarenite with helix
				3	2			White, moderately hard, cross bedded calcarenite
				2	3			Brown, friable, calcarenite with helix
				1	1			Yellow, hard, fossiliferous calcarenite

Fig. 3.6: Generalized lithostratigraphic column of the Gargaresh Formation at station no. 3 (Janzour)






Series	Stage	Formation	Member	Unit	Thick(m)	Lithology	Hardness	Description
Pleistocene	Tyrrenian	Gargaresh	kaam	1	2		S M H	White, moderately hard, cross bedded calcarenite
			Karrot	4	3		S M H	Massive, moderately hard, calcarenite with helix
				3	1		S M H	White, moderately hard, cross bedded calcarenite
				2	1		S M H	Brown, friable, calcarenite with helix
				1	4		S M H	Yellow, hard, fossiliferous calcarenite

Fig. 3.7: Generalized lithostratigraphic column of the Gargaresh Formation at station no. 4 (Al Mayah)
















Series	Stage	Formation	Member	Unit	Thick(m)	Lithology	Hardness	Description
Pleistocene	Tyrrenian	Gargaresh	kaam	1	3		S M H	White, moderately hard, cross bedded calcarenite
			Karrot	4	1		S M H	Massive, moderately hard, calcarenite with helix
				3	4		S M H	White, moderately hard, cross bedded calcarenite
				2	3		S M H	Brown, friable, calcarenite with helix
				1	1.5		S M H	Yellow, hard, fossiliferous calcarenite

Fig. 3.8: Generalized lithostratigraphic column of the Gargaresh Formation at station no. 5 (Az Zawiyah)

Series	Stage	Formation	Member	Unit	Thick(m)	Lithology	Hardness	Description
<i>Pleistocene</i>	Tyrrhenian	<i>Gargaresh</i>	kaam	1	4			White, moderately hard, cross bedded calcarenite
			Karrot	4	1.5			Massive, moderately hard, calcarenite with helix
				3	3			White, moderately hard, cross bedded calcarenite
				2	2			Brown, friable, calcarenite with helix
				1	0.5			Yellow, hard, fossiliferous calcarenite

*Fig. 3.9: Generalized lithostratigraphic column of the Gargaresh Formation at station no. 6 (El Matered)*

Series	Stage	Formation	Member	Unit	Thick(m)	Lithology	Hardness	Description
<i>Pleistocene</i>	Tyrrhenian	<i>Gargaresh</i>	kaam	1	5			White, moderately hard, cross bedded calcarenite
			Karrot	4	2			Massive, moderately hard, calcarenite with helix
				3	1			White, moderately hard, cross bedded calcarenite
				2	1			Brown, friable, calcarenite with helix
				1	0.5			Yellow, hard, fossiliferous calcarenite

*Fig. 3.10: Generalized lithostratigraphic column of the Gargaresh Formation at station no. 7 (Sabratah)*

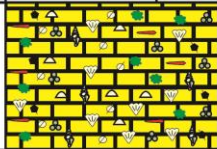
Series	Stage	Formation	Member	Unit	Thick(m)	Lithology	Hardness	Description
Pleistocene	Tyrrhenian	Gargaresh	Karrot	1	3		S M H	Yellow, hard, fossiliferous calcarenite

Fig. 3.11: Generalized lithostratigraphic column of the Gargaresh Formation at station no. 8 (Marsa Zuwaghah)

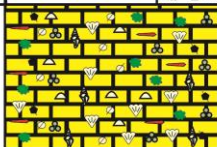
Series	Stage	Formation	Member	Unit	Thick(m)	Lithology	Hardness	Description
Pleistocene	Tyrrhenian	Gargaresh	Karrot	1	1		S M H	Yellow, hard, fossiliferous calcarenite

Fig. 3.12: Generalized lithostratigraphic column of the Gargaresh Formation at station no. 9 (Zuwarah)


Series	Stage	Formation	Member	Unit	Thick(m)	Lithology	Hardness	Description
Pleistocene	Tyrrhenian	Gargaresh	Karrot	1	2.5		S M H	Yellow, hard, fossiliferous calcarenite

Fig. 3.13: Generalized lithostratigraphic column of the Gargaresh Formation at station no. 10 (Abu Kammash)















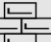
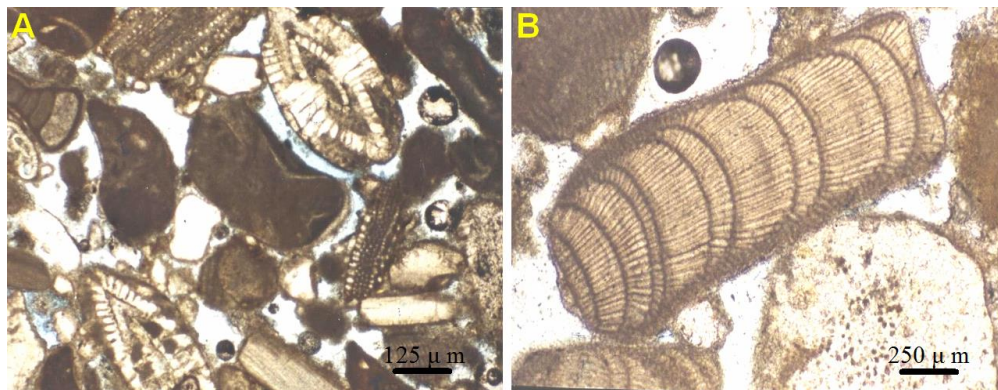
Series	Stage	Formation	Member	Unit	Thick(m)	Sample No.	Lithology	Hardness	Description
Late pleistocene	Tyrrhenian	Gargaresh	Karrot	1	0.5				Yellow, hard, fossiliferous calcarenite

Fig. 3.14: Generalized lithostratigraphic column of the Gargaresh Formation at station no. 11 (Ras Jdeir)

Legend				
	Bryozoan			Benthonic Foraminifera
	Ostracoda			Planktonic Foraminifera
	pelecypoda			algae
	Echinoid			Gastropoda (land snail)
	Shell fragments			Echinoidal spine
	Gastropoda			Burrows
	Cross bedding			calcarenite



*Fig. 3.15: Calcarenite rocks (unit 1) dipping NE (seaward direction) at station no. 4 (Al Mayah)*



*Fig. 3.16: Photomicrographs (A and B) of grainstone contains foraminifera (*Elphidium* sp.), coralline red algae, echinoid spine and bivalves, meniscus cement, intergranular and vuge porosity (samples 1a and 5a from Tajoura and Az Zawiyah, respectively)*



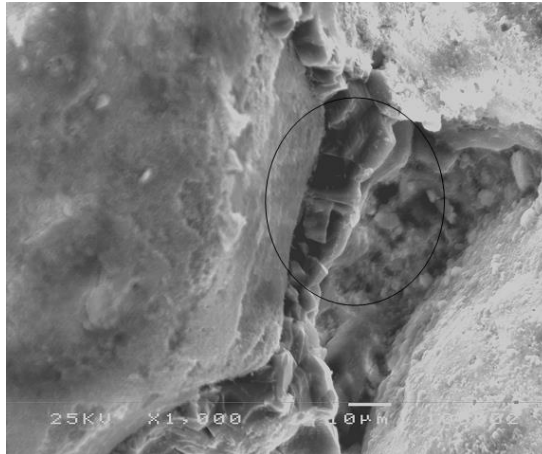


*Fig. 3.17: BSE image showing the cement that is completely filling porosity (sample 2a from Tripoli)*

**Unit 2:** Except unit 1, all other units are only detected from station no. 2 (Tripoli) to station no. 7 (Sabratah, *see* Figs. 3.4-14). In the field, unit 2 is composed of brown friable calcarenite (Fig. 3.18) rich in shell fragments and land snail (*Helix sp.*, Fig. 3.19). This unit is dipping seaward.



*Fig. 3.18: Friable calcarenite (unit 2) overlain by semi-hard calcarenite displays cross bedding (unit 3) at station no. 6 (El Matered)*



Fig. 3.19: Hand specimen of unit 2, at station no. 2 (Tripoli), showing shell fragments and land snail (arrow)

Microscopically, the allochems of this unit are composed of pellets, fossils and shell fragments with few intraclasts, characterized by medium to coarse, rounded and moderately sorted. Subrounded quartz grains coated by micrite are observed. The occurrence of quartz grains in this unit may point to an intermittent seaward wind blowing. The fossil contents are shells of bivalve, land snail (*Helix sp.*), foraminifera (rotalid, miliolid and Elphidium), echinoid spines and plates, bryozoans and algae. This unit is generally weakly cemented by isopachous and meniscus cement (point and contact cements) and intergranular and vuge porosity. The loosely packed fabric of this unit and the absence of well-developed cement can be attributed to lack of source and lack of unsuitable geological condition which may indicate that this unit was deposited under wet condition (moist phase). Uniform thin rim from fringing calcite cement surrounding the grains of this unit is indicative of precipitation in phreatic zone (Fig. 3.20), where all pores are filled with water. Also it is a typical feature of low-intertidal and subtidal cements. No sign of severe diagenesis is noticed, however, few quartz grains suffered from percussion probably during transportation. The transporting agent is possibly wind that could have blown seaward, bringing quartz grains to the site of deposition especially near shore which is otherwise quartz-free.

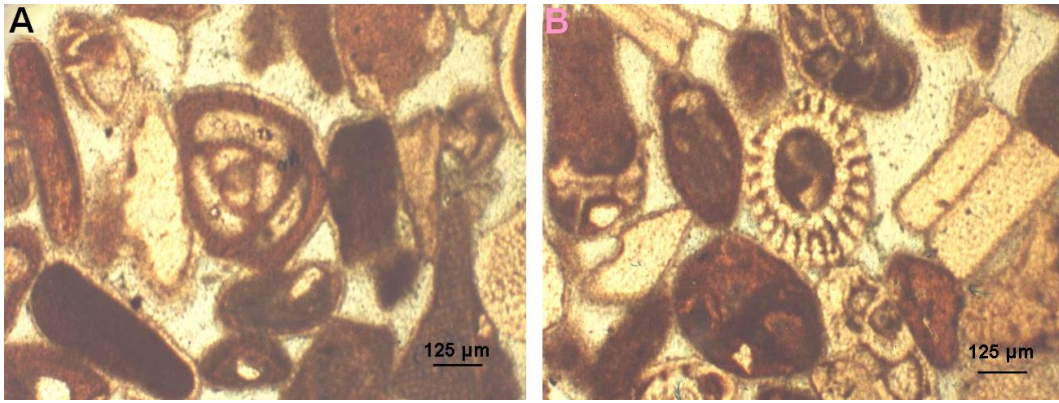


*Fig. 3.20: Photomicrographs (A and B) of grainstone contains subrounded quartz grains coated by micrite. The fossil content includes echinoderm plate and spine, miliolid and rotalid foraminifera, bivalve shells, bryozoans and transverse section parallel to long axis of sponge spicules (upper left part in B, note the thick walls and central canal characteristic of many originally opaline spicules), isopachous and meniscus cement, intergranular and vuge porosity (samples 5c and 7c from Az Zawiyah and Sabratah, respectively)*

**Unit 3:** In the field, it is composed of white semi-hard calcarenite which commonly displays tabular planar cross bedding, laminated graded and cross bedding. It is also characterized by burrows (Fig. 3.21). Microscopically, the allochems composed of algal peloids, fossils and shell fragments, intraclasts, superficial ooliths, subrounded to subangular quartz grains coated by micrite. Most grains of this unit are well sorted and well rounded. The fossil content is mainly benthonic foraminifera, bivalve shells, echinoderm plate and spine, debris of coralline algae, gastropod, ostracod and bryozoans (Figs. 3.22-23).

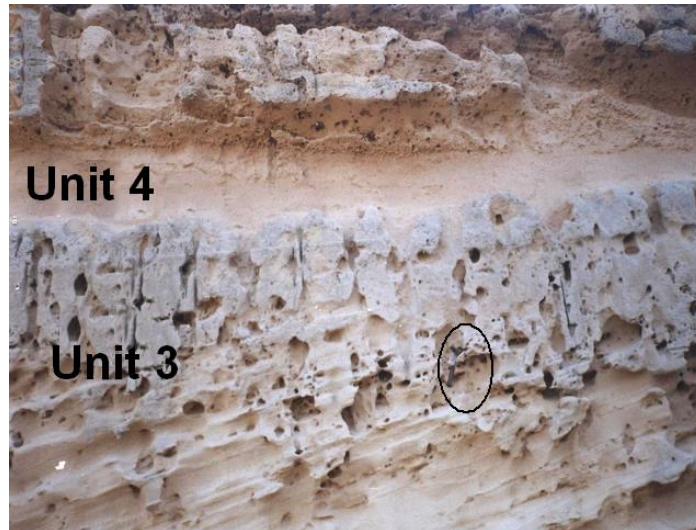


*Fig. 3.21: moderately hard calcarenite (unit 3) displays large scale tabular planar cross bedding (dipping NE) and burrows, overlain by massive semi-hard calcarenite (unit 4) at station no. 2 (Tripoli)*

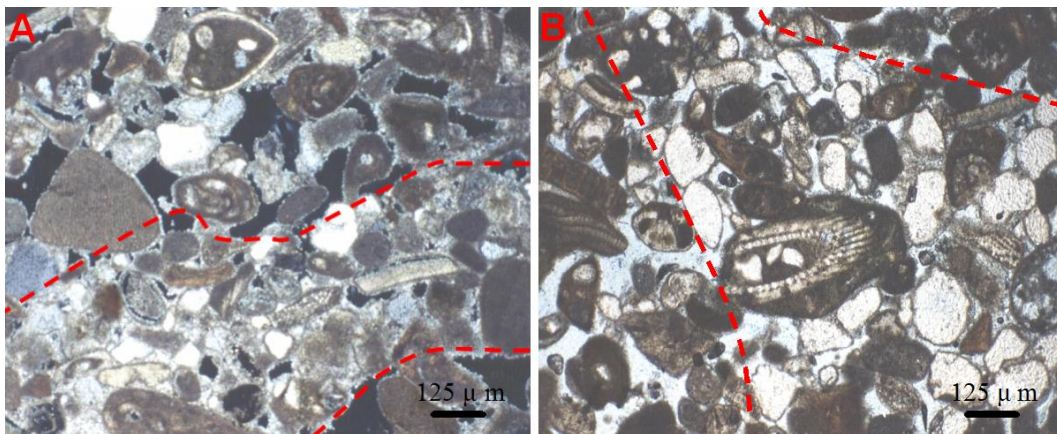


*Fig. 3.22: Photomicrographs (A and B) of grainstone contains laminated graded bedding from medium grains, high porosity to fine grains, low porosity in A, and from lamina rich by subangular quartz grains and the other rich by fossils and shell fragments in B. Isopachous and meniscus cement(samples 2e and 3e from Tripoli and Janzour, respectively)*

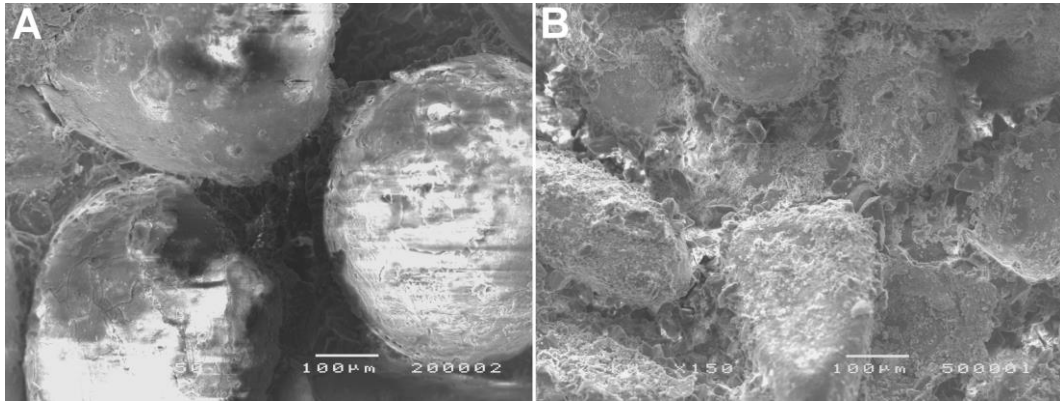


*Fig. 3.23: BSE images showing meniscus cement (A, sample 7e from Sabratah) and isopachous cement (B, sample 4e from Al Mayah)*

**Unit 4:** In the field, it consists of lenses of massive moderately hard calcarenite with abundant land snail (*Helix sp.*). This unit occurs as lenses (wedge shape, Fig. 3.24).

Microscopically, the allochems of this unit are composed of shell fragments, pellets mainly fecal pellets of burrowing shrimp, superficial ooliths and intraclasts. Medium to coarse grains, moderately to poorly sorted and poorly washed in which wind-blown angular quartz are imbedded as a matrix in micrite (Fig. 3.25). The compositions of this unit are affected by severe diagenesis and the grains are weakly cemented, oomouldic, vuge, intra- and intergranular porosity. Most grains of this unit are composed of different varieties, such as quartz grains, rounded intraclasts, superficial ooliths and micritized fossils (Fig. 3.26).

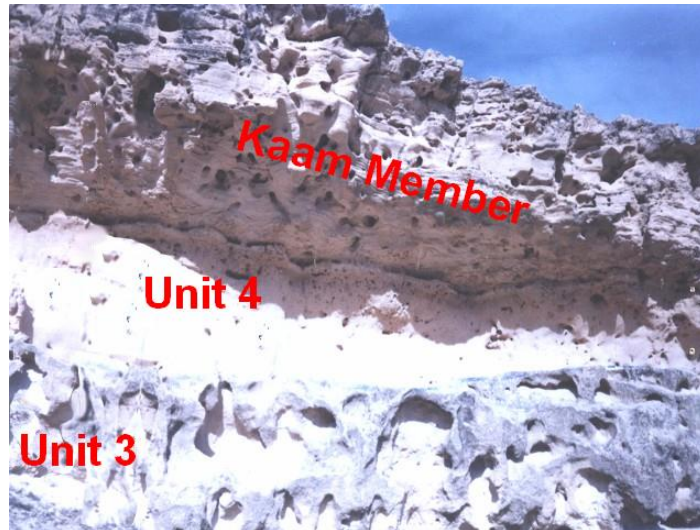


*Fig. 3.24: moderately hard calcarenite (unit 3), overlain by wedge shape of massive semi-hard calcarenite (unit 4) at station no. 5 (Az Zawiyah)*

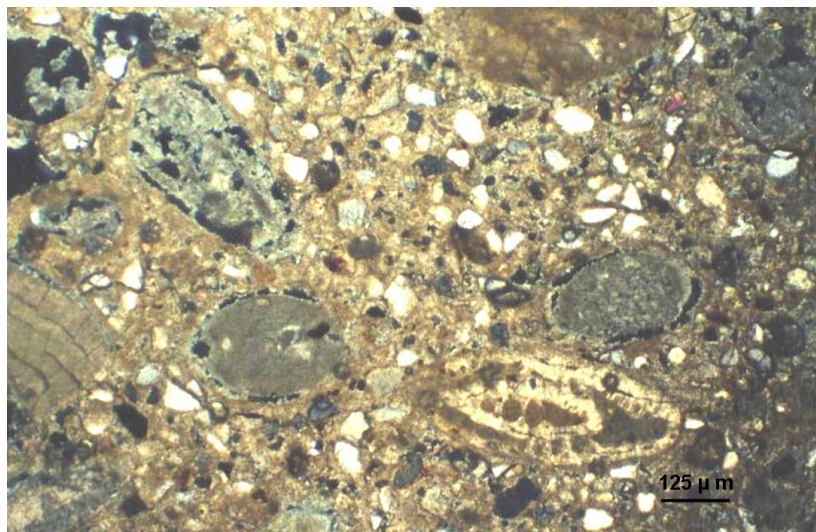


*Fig. 3.25: Photomicrograph of packstone. The matrix is composed of angular quartz grains imbedded in micrite. Oomouldic, inter- and intragranular porosity (sample 7g from Sabratah)*

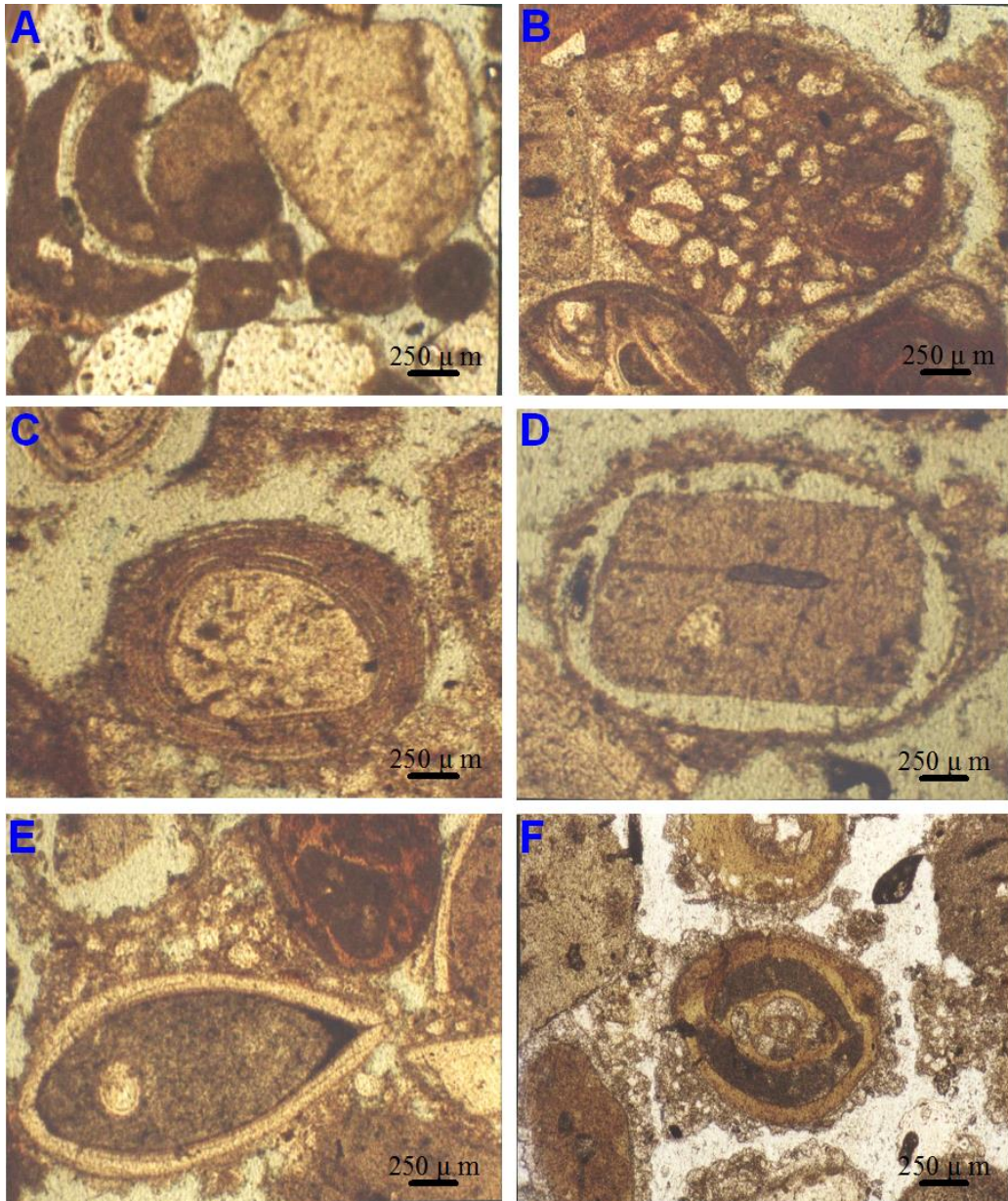


*Fig. 3.26: Photomicrographs of unit 4 shows, subangular quartz grains suffered from percussion arranged as a laminar texture alternating with oriented pellets and fossils (A). Intraclasts and meniscus cement with other high preserved fossils, vuggy and cavern porosity (B). Superficial ooids with concentric structure and thick cortex (C). Very thin cortex with oomouldic porosity (D). Bivalves shell has the original wall and the cavity is packed by micritized material (E). High micritized allochems as shown in miliolid foraminifera (F) (sample 7g from Sabratah)*

### 3.2. Kaam Member

The Kaam Member is only detected in the area between Tripoli and Sabratah. It is represented by one unit (according to texture, morphology, sedimentary structure and fossil content). It is white semi-hard calcarenite consisting of tabular planar cross bedding (Fig. 3.27). According to Hlal and Bennur (2014) this member was deposited under aeolian conditions.



*Fig. 3.27: moderately hard calcarenite (Kaam Member) showing tabular planar cross bedding at station no. 6 (El Matered)*

Microscopically, the allochems of this unit consists of pellets mainly fecal pellets of burrowing shrimp, fossils and shell fragments, superficial ooids and intraclasts. Fine to medium grains, moderately well sorted and well rounded. The fossil contents are foraminifera (miliolid and rotalid), bivalves, coralline algae, echinoid spine and plate, ostracod, bryozoans and gastropods. Mouldic, inter- and intragranular porosities represent 10-15% (Fig. 3.28). This unit is partly characterized by alternating lamina of elongate oriented grains (parallel to stratification) and graded bedded laminar structure (Fig. 3.29). Ooliths nuclei are fossils, quartz grains, rounded micrite fragments or intraclasts (Fig. 3.30). Meniscus and isopachous cements are found in this unit which indicates vadose and phreatic zones precipitation. Meniscus cements grain to grain bridges are shown in Fig. (3.31).



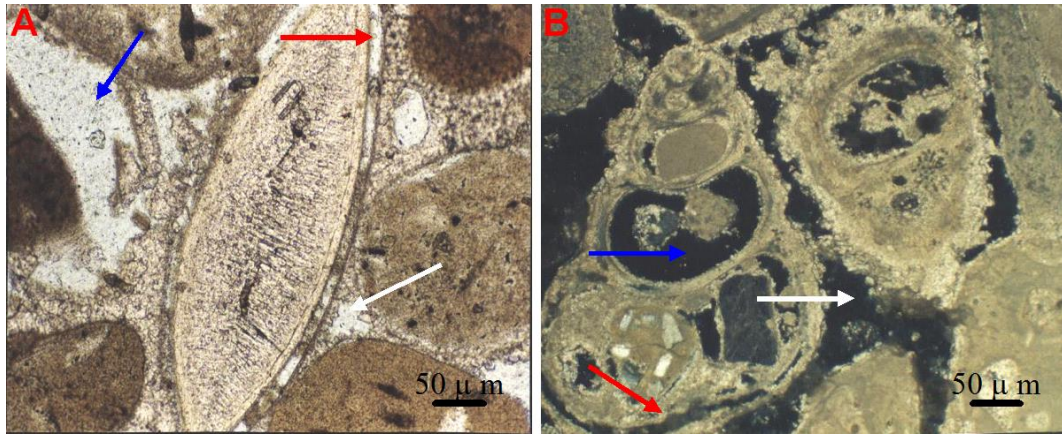


*Fig. 3.28: Photomicrographs of grainstone showing partial alteration of bivalve wall texture and radiaxial fibrous spar filling of its void (A). Longitudinal section of two gastropod fossils, note the chambers are partially filled by intraclasts, ooid grains and micritized fragments (B). Mouldic (red arrows), intergranular (white arrows) and intragranular (blue arrows) porosities are established (sample 7i from Sabratah)*

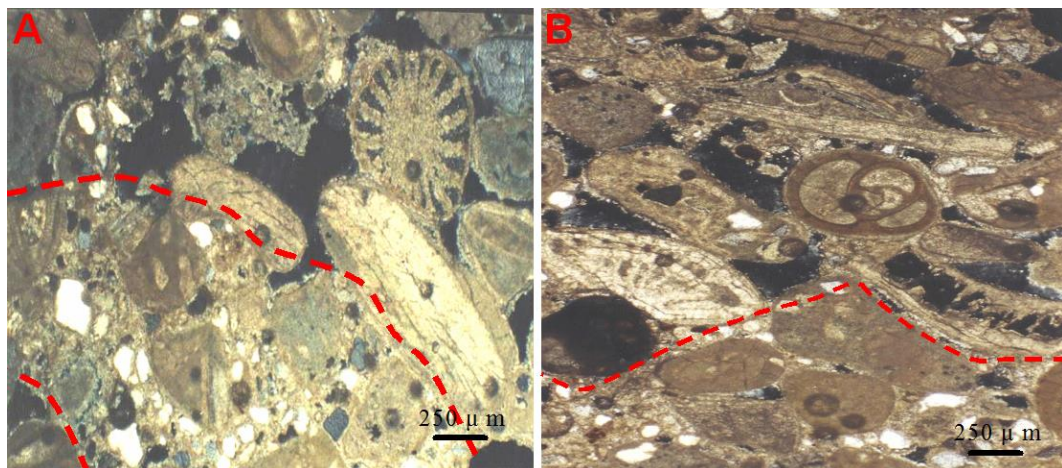


*Fig. 3.29: Photomicrographs of grainstone (A and B) showing laminar texture, alternating between lamina characterized by lacking of matrix, well washed, meniscus cement, mouldic, inter- and intragranular porosity and poorly washed lamina, composed of allochems grains imbedded with angular quartz grains in micrite groundmass and trivial porosity. Note the oriented allochems in the same direction of lamination, (sample 5i from Az Zawiyah)*

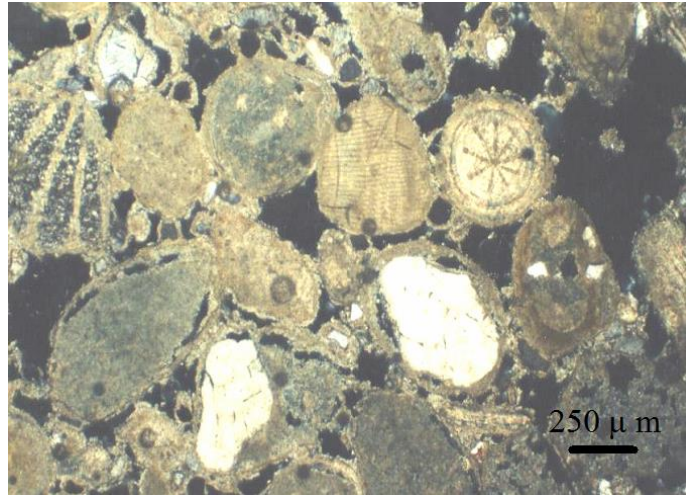


*Fig. 3.30: Photomicrograph of grainstone showing superficial ooids with nuclei from fossils, pellets and quartz grains, meniscus cement, oomouldic, inter- and intragranular porosity (sample 5i from Az Zawiyah)*

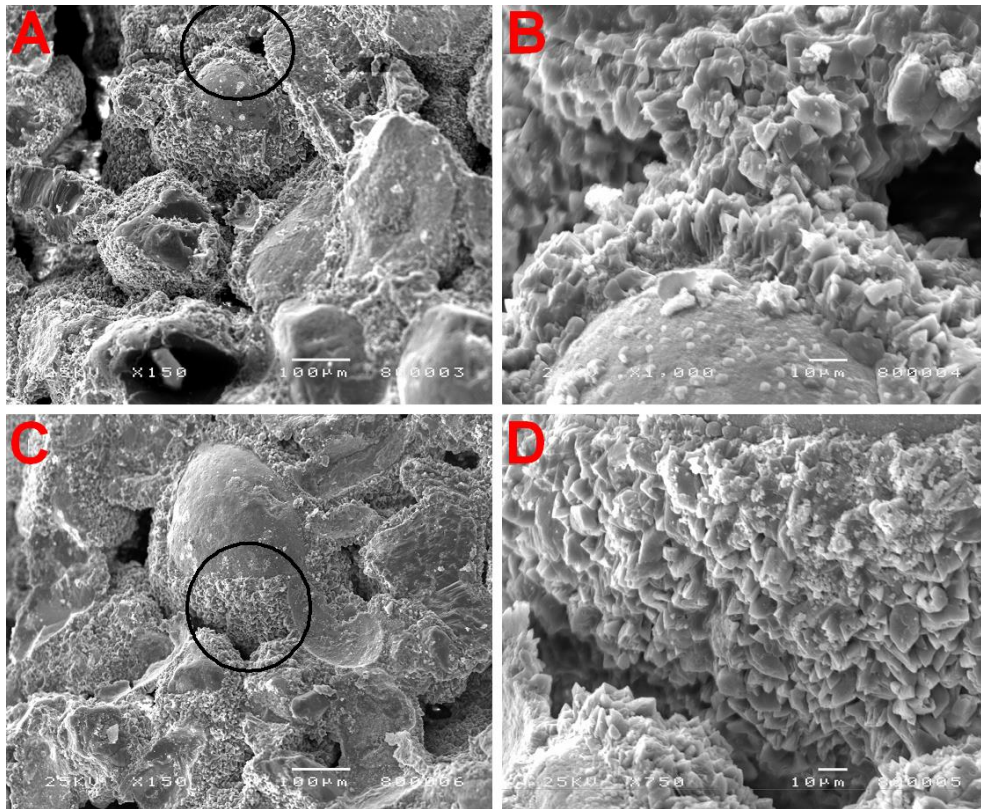


*Fig. 3.31: BSE images showing isopachous and meniscus cements. The meniscus cement (grain to grain bridges) is well observed in A and B. Notice that B and D are enlarged figures of A and C, respectively (sample 5i from Az Zawiyah)*

### 3.3. Morphology of Gargaresh Formation

There are two types of morphology; biogenic and non-biogenic.

#### 3.3.1. Biogenic calcarenite

This calcarenite has a variety of structures and textures including soft sediment burrows and hard rock borings; plant remains (Fig. 3.32), trails mounds and holes (Fig. 3.33).



*Fig. 3.32: Tubular voids (arrow A) is a soil filled root molds and arrow B refers to plant root (Karrot Member (unit 1) at station no. 10 (Abu Kammash))*



*Fig. 3.33: A variety of trails mounds and holes created by unidentified organisms (Karrot Member (unit 3) at station no. 5 (Az Zawiyah))*

### 3.3.2. Non-biogenic calcarenite

There are four groups of non-biogenic morphology and structures in the studied formation, namely:

**1- Pre-depositional (interbed):** this structure occurs on the surface between beds (see Fig. 3.32)

**2- Syn-depositional (intrabed):** the syn-depositional bed occurs as:

A - Massive bedding: there is absence of any form of sedimentary structure. It is observed in units 2 and 4.

B- Cross bedding: It is one of the common sedimentary structures in Gargaresh Formation. It consists of inclined dipping bedding, bounded by sub-horizontal surfaces; each of these units is termed as set. These sets may be tabular, teepee, hummocky, wedge-shaped and convoluted (Figs. 3.34-36).



*Fig. 3.34: moderately hard calcarenite (Karrot Member (unit 3) characterized by large scale cross beds overlain by teepee structure (arrow), general dip toward sea at station no. 4 (Al Mayah)*



*Fig. 3.35: moderately hard calcarenite (Karrot Member (unit 3)) characterized by wedge tabular planar cross bedding and hummocky cross lamination (arrows) at station no. 3 (Janzour)*

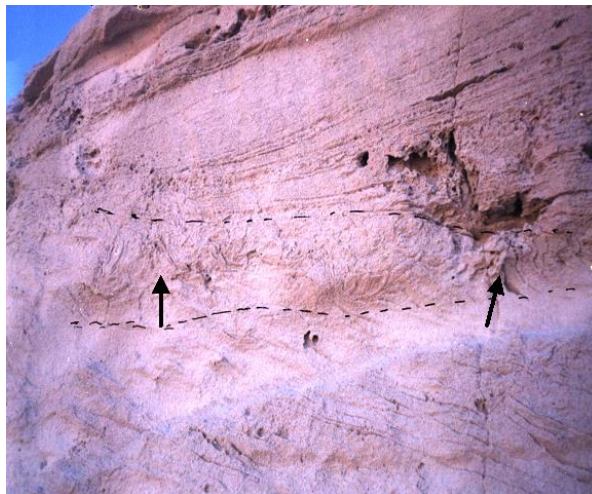


*Fig. 3.36: moderately hard calcarenite (Kaam Member) characterized by convolute lamination (between dashed lines) occurs between herring bone cross bedding due to tidal currents at station no. 6 (El Matered)*

C – Lamination and cross lamination: The rock mass has prominent divisions, each of which is less than 1 cm in thickness (Fig. 3.37).

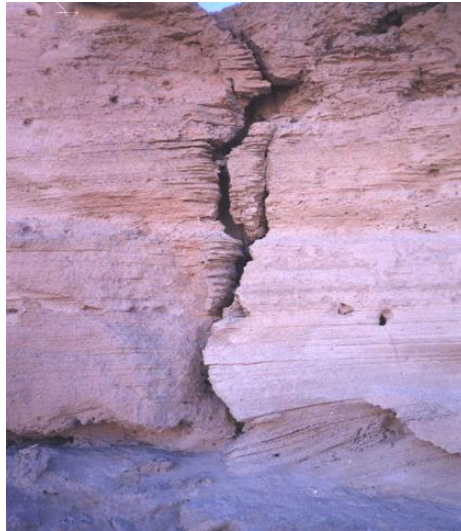


*Fig. 3.37: moderately hard calcarenite (Kaam Member) characterized by lamination and cross lamination at station no. 6 (El Matered)*

**3- Post-depositional (deformed interbed and intrabed structures):** It includes vertical and horizontal plastic deformational structures (Figs. 3.38).



*Figs. 3.38: Wave-cut cliffs of Karrot Member (unit 3) occupied by large collapsed beach rock slabs, dipping landward at station no. 3 (Janzour)*

**4- Miscellaneous:** It includes cracks (Fig. 3.39)



*Fig. 3.39: Cracks in Karrot Member (unit 4) at station no. 6 El Matered*

## **CHAPTER FOUR**

### **GEOCHEMISTRY**

#### **4.1. Introduction**

Elemental concentrations in sediments result from the competing influences of provenance, weathering, diagenesis, and sediment sorting (Quinby-Hunt *et al.*, 1991). The present geochemical study is based on complete chemical analysis data of 71 samples of Gargaresh Formation along the Mediterranean Coast from Tajoura to Ras Jdeir, Jifarah plain, NW Libya (*see* Fig. 1.1). Analysis of major oxides and trace elements was done by inductively coupled plasma-mass spectrometry (ICP-MS) technique. This technique is suitable for determining trace elements in various samples because of its high sensitivity, rapidity, simplicity, multi-elemental and isotopic capability (Itoh *et al.*, 1999). The data include 12 major oxides and 23 trace elements, as quoted in tables (4.1-11).

#### **4.2. Statistical Treatment**

The statistical treatment of the obtained data involves descriptive statistics and correlation matrix using the SPSS<sup>®</sup> program. The correlation matrix (Table 4.12) suggests that the heavy metals are possibly of different sources. The Th and U as well as the REE are essentially related to marine and terrestrial inputs. Table (4.13) indicates that the studied formation may contain high concentrations of some elements such as Sr (5831 ppm), Co (833.78 ppm), Cu (121.39 ppm), Zn (220.7 ppm), Zr (871.15 ppm), Th (172.76 ppm) and REE (151 ppm). These maximum values, besides the high standard deviation values represent derivation from multi-sources and possible contribution from mineralized sources at the hinterland.

#### **4.3. Major oxides**

The major elements are generally considered somewhat mobile during weathering, transportation, and post-depositional processes (McLennan *et al.*, 1993). In the present study, the geochemistry of the major oxides is essentially controlled by the mineral composition of the studied sediments which, in turn, roles the mutual abundance and distribution of the trace elements.



Table 4.1: Chemical analysis data (major oxides in wt%, trace elements in ppm) of the Gargaresh Formation at station no.1 (Tajoura)

Location	Tajoura	
Member	Karrot Member	
Unit	Unit1	
Sample No.	1a	1b
SiO <sub>2</sub>	11.21	11.87
TiO <sub>2</sub>	0.04	0.04
Al <sub>2</sub> O <sub>3</sub>	0.46	0.57
Fe <sub>2</sub> O <sub>3</sub>	0.24	0.33
MgO	2.15	2.07
CaO	47.75	46.51
Na <sub>2</sub> O	0.38	0.24
K <sub>2</sub> O	0.12	0.11
SO <sub>3</sub>	0.01	0.01
Cl	0.19	0.15
P <sub>2</sub> O <sub>5</sub>	0.02	0.03
LOI	37.19	38.00
Total	99.76	99.93
Sr	2386	2259
Ni	6.93	7.70
Co	139.29	148.11
Cu	19.18	21.70
Zn	36.66	38.00
Pb	26.98	26.72
Zr	162.52	171.34
Th	42.41	44.93
U	17.67	18.54
La	22.08	22.27
Ce	40.22	40.41
Pr	5.31	5.50
Nd	19.24	19.43
Sm	3.64	3.83
Eu	1.42	1.61
Gd	2.93	3.12
Tb	0.78	0.97
Dy	2.06	2.25
Ho	0.69	0.88
Er	1.21	1.40
Tm	0.48	0.57
Yb	1.22	1.41
Lu	0.45	0.54

Table 4.2: Chemical analysis data (major oxides in wt%, trace elements in ppm) of the Gargaresh Formation at station no.2 (Tripoli)

Location	Tripoli									
Member	Karrot Member								Kaam Member	
Unit	Unit1		Unit2		Unit3		Unit4			
Sample No.	2a	2b	2c	2d	2e	2f	2g	2h	2i	2j
SiO <sub>2</sub>	7.44	6.78	29.34	30.42	2.93	3.13	27.27	26.09	3.69	3.56
TiO <sub>2</sub>	0.04	0.04	0.15	0.13	0.03	0.03	0.11	0.12	0.02	0.01
Al <sub>2</sub> O <sub>3</sub>	0.28	0.36	2.66	2.81	0.17	0.21	2.23	2.11	0.36	0.31
Fe <sub>2</sub> O <sub>3</sub>	0.20	0.35	0.97	0.73	0.21	0.18	1.03	1.00	0.12	0.14
MgO	2.44	2.69	1.28	1.11	3.02	2.90	1.66	1.74	2.81	2.70
CaO	48.13	48.48	32.00	31.96	54.00	52.12	33.35	33.86	51.90	51.81
Na <sub>2</sub> O	0.17	0.14	1.02	1.00	0.24	0.28	0.93	0.88	0.33	0.31
K <sub>2</sub> O	0.01	0.01	0.54	0.44	0.08	0.08	0.43	0.36	0.03	0.03
SO <sub>3</sub>	0.01	0.01	0.01	0.01	0.01	0.01	0.01	0.01	0.01	0.01
Cl	0.35	0.30	1.03	1.00	0.09	0.11	0.93	0.89	0.26	0.24
P <sub>2</sub> O <sub>5</sub>	0.03	0.03	0.01	0.01	0.02	0.02	0.01	0.01	0.01	0.01
LOI	40.40	40.56	30.90	30.37	39.10	40.93	31.90	32.67	40.41	40.00
Total	99.50	99.75	99.91	99.99	99.90	99.99	99.86	99.74	99.96	99.13
Sr	2472	2568	1297	1007	5831	3416	1296	1352	3289	3195
Ni	3.91	4.41	14.32	16.80	2.72	3.00	11.00	10.50	5.55	5.09
Co	105.13	111.19	389.10	391.06	88.92	96.77	220.10	208.09	129.38	124.12
Cu	11.88	12.82	30.75	32.30	9.51	9.73	27.70	25.25	16.40	14.07
Zn	22.44	23.93	53.50	57.17	17.29	18.09	45.86	43.54	28.21	26.09
Pb	28.93	30.08	18.35	15.93	41.11	38.20	20.81	22.60	34.00	32.32
Zr	128.36	134.42	428.33	430.29	128.15	136	259.33	247.32	184.61	179.35
Th	35.11	36.05	69.98	71.53	48.74	48.96	66.93	64.48	71.63	69.3
U	15.25	15.53	26.88	27.36	19.78	19.84	25.86	25.04	27.43	26.62
La	21.77	21.96	13.84	13.70	29.22	29.09	14.10	13.90	50.36	50.31
Ce	39.91	40.10	41.76	41.62	58.28	58.15	42.00	41.82	55.54	55.49
Pr	5.00	5.19	3.17	3.03	7.31	7.18	3.40	3.23	6.56	6.51
Nd	18.93	19.12	12.38	12.24	29.62	29.49	12.60	12.44	18.64	18.59
Sm	3.33	3.52	2.44	2.30	6.10	5.97	2.70	2.50	2.95	2.90
Eu	1.11	1.30	0.71	0.57	1.81	1.68	0.90	0.77	0.17	0.12
Gd	2.62	2.81	2.29	2.15	5.70	5.57	2.50	2.35	1.16	1.11
Tb	0.47	0.66	0.40	0.26	0.91	0.78	0.60	0.46	0.15	0.10
Dy	1.75	1.94	2.31	2.17	4.82	4.69	2.50	2.37	0.52	0.47
Ho	0.38	0.57	0.55	0.41	1.09	0.96	0.80	0.61	0.19	0.14
Er	0.90	1.09	1.62	1.48	2.72	2.59	1.80	1.68	0.54	0.49
Tm	0.17	0.26	0.27	0.13	0.45	0.32	0.50	0.33	0.12	0.07
Yb	0.91	1.10	1.63	1.49	2.60	2.47	1.80	1.69	0.49	0.44
Lu	0.14	0.23	0.28	0.14	0.41	0.28	0.50	0.34	0.12	0.07

Table 4.3: Chemical analysis data (major oxides in wt%, trace elements in ppm) of the Gargaresh Formation at station no.3 (Janzour)

Location	Janzour									
Member	Karrot Member								Kaam Member	
Unit	Unit1		Unit2		Unit3		Unit4			
Sample No.	3a	3b	3c	3d	3e	3f	3g	3h	3i	3j
SiO <sub>2</sub>	7.74	7.06	29.64	30.72	3.23	3.43	27.57	26.39	3.99	3.86
TiO <sub>2</sub>	0.04	0.04	0.16	0.13	0.03	0.03	0.12	0.12	0.02	0.02
Al <sub>2</sub> O <sub>3</sub>	0.58	0.66	2.96	3.11	0.47	0.23	2.53	2.41	0.66	0.61
Fe <sub>2</sub> O <sub>3</sub>	0.15	0.65	0.87	1.03	0.23	0.48	1.09	0.94	0.17	0.19
MgO	2.14	2.39	0.98	0.81	2.83	2.60	1.36	1.44	2.51	2.40
CaO	47.83	48.18	31.70	31.66	53.70	51.82	33.05	33.56	51.60	51.51
Na <sub>2</sub> O	0.19	0.11	0.88	0.50	0.17	0.21	0.63	1.00	0.42	0.50
K <sub>2</sub> O	0.02	0.02	0.84	0.74	0.08	0.08	0.73	0.66	0.03	0.03
SO <sub>3</sub>	0.31	0.31	0.01	0.01	0.01	0.01	0.01	0.01	0.01	0.01
Cl	0.37	0.27	0.89	0.50	0.32	0.41	0.63	1.05	0.45	0.49
P <sub>2</sub> O <sub>5</sub>	0.03	0.03	0.01	0.01	0.02	0.02	0.01	0.01	0.01	0.01
LOI	40.10	40.26	30.60	30.07	38.80	40.63	31.60	32.37	40.11	39.70
Total	99.50	99.98	99.54	99.29	99.89	99.95	99.33	99.96	99.98	99.33
Sr	2390	2407	1285	1283	5799	5596	1284	1304	3270	3264
Ni	8.74	9.94	15.94	16.74	7.52	3.68	12.48	11.89	10.18	9.40
Co	175.63	199.85	432.98	454.93	245.84	120.30	249.71	237.87	237.20	219.23
Cu	24.18	27.52	34.22	35.95	26.29	12.87	31.43	29.94	30.07	27.79
Zn	46.22	52.60	32.64	37.15	47.80	23.39	52.03	49.56	51.72	47.80
Pb	27.03	27.22	18.18	18.16	40.88	39.45	20.62	20.94	33.80	33.74
Zr	208.86	233.08	496.21	518.16	309.07	183.53	312.94	301.10	278.43	260.46
Th	57.41	60.75	97.45	99.18	89.52	76.10	94.66	93.17	71.30	69.02
U	22.69	23.75	36.00	36.59	33.38	28.90	35.07	34.58	27.28	26.54
La	22.12	22.28	13.71	13.69	29.06	28.04	13.97	14.19	50.07	49.98
Ce	40.29	40.58	41.37	41.32	57.96	55.93	41.62	42.26	55.22	55.12
Pr	5.34	5.36	3.14	3.14	7.27	7.01	3.37	3.42	6.52	6.51
Nd	19.27	19.41	12.26	12.25	29.46	28.42	12.49	12.68	18.53	18.50
Sm	3.65	3.67	2.42	2.41	6.07	5.85	2.68	2.72	2.93	2.93
Eu	1.42	1.43	0.70	0.70	1.80	1.74	0.89	0.91	0.17	0.17
Gd	2.95	2.96	2.27	2.27	5.67	5.47	2.48	2.52	1.15	1.15
Tb	0.78	0.79	0.40	0.40	0.90	0.87	0.59	0.60	0.15	0.15
Dy	2.08	2.08	2.29	2.29	4.79	4.63	2.48	2.52	0.52	0.52
Ho	0.70	0.70	0.54	0.54	1.08	1.05	0.79	0.81	0.19	0.19
Er	1.22	1.22	1.60	1.60	2.70	2.61	1.78	1.81	0.54	0.54
Tm	0.48	0.48	0.27	0.27	0.45	0.43	0.50	0.50	0.12	0.12
Yb	1.22	1.23	1.61	1.61	2.59	2.50	1.78	1.81	0.49	0.49
Lu	0.45	0.45	0.28	0.28	0.41	0.39	0.50	0.50	0.12	0.12

Table 4.4: Chemical analysis data (major oxides in wt%, trace elements in ppm) of the Gargaresh Formation at station no.4 (Al Mayah)

Location	Al Mayah									
Member	Karrot Member								Kaam Member	
Unit	Unit1		Unit2		Unit3		Unit4			
Sample No.	4a	4b	4c	4d	4e	4f	4g	4h	4i	4j
SiO <sub>2</sub>	8.04	7.38	29.94	31.02	3.53	3.73	27.87	26.69	4.29	4.16
TiO <sub>2</sub>	0.04	0.04	0.16	0.13	0.03	0.03	0.10	0.11	0.02	0.01
Al <sub>2</sub> O <sub>3</sub>	0.88	0.96	3.26	3.41	0.77	0.81	2.83	2.71	0.96	0.91
Fe <sub>2</sub> O <sub>3</sub>	0.53	0.88	0.57	0.46	0.31	0.28	0.92	0.79	0.09	0.09
MgO	1.84	2.09	0.68	0.51	2.42	2.30	1.06	1.14	2.21	2.10
CaO	47.53	47.88	31.40	31.36	53.40	51.52	32.75	33.26	51.30	51.21
Na <sub>2</sub> O	0.22	0.19	1.22	1.13	0.40	0.44	1.00	1.10	0.45	0.63
K <sub>2</sub> O	0.01	0.01	1.14	1.04	0.08	0.08	1.03	0.96	0.03	0.03
SO <sub>3</sub>	0.01	0.01	0.01	0.01	0.01	0.01	0.01	0.01	0.01	0.01
Cl	0.40	0.35	1.21	1.13	0.25	0.37	1.00	1.11	0.38	0.56
P <sub>2</sub> O <sub>5</sub>	0.03	0.03	0.01	0.01	0.02	0.02	0.01	0.01	0.01	0.01
LOI	39.80	39.96	30.30	29.77	38.50	40.33	31.30	32.07	39.81	39.40
Total	99.33	99.78	99.90	99.98	99.72	99.92	99.88	99.96	99.56	99.12
Sr	2375	2393	1273	1271	5766	5563	1273	1293	3251	3245
Ni	13.26	14.46	17.55	18.36	12.32	12.96	13.96	13.37	14.80	14.03
Co	266.47	290.69	476.87	498.81	402.76	423.68	279.32	267.48	345.01	327.04
Cu	36.69	40.03	37.69	39.42	43.07	45.31	35.15	33.66	43.73	41.46
Zn	70.13	76.51	49.53	54.03	78.31	82.38	58.20	55.73	75.23	71.31
Pb	26.86	27.05	18.01	17.98	40.65	39.22	20.44	20.75	33.61	33.55
Zr	299.70	323.92	534.10	556.04	459.99	480.91	336.55	324.71	378.24	360.27
Th	69.92	73.26	94.92	96.65	100.30	102.54	92.38	90.89	76.96	74.69
U	26.82	27.94	35.19	35.75	36.97	37.71	34.33	33.83	29.19	28.42
La	21.98	22.14	13.58	13.56	28.90	27.88	13.85	14.06	49.78	49.69
Ce	40.03	40.33	40.98	40.92	57.63	55.60	41.24	41.89	54.90	54.80
Pr	5.29	5.32	3.11	3.11	7.23	6.97	3.34	3.39	6.48	6.47
Nd	19.15	19.29	12.15	12.13	29.29	28.26	12.37	12.57	18.42	18.39
Sm	3.62	3.65	2.39	2.39	6.03	5.82	2.65	2.69	2.92	2.91
Eu	1.41	1.42	0.70	0.70	1.79	1.73	0.88	0.90	0.17	0.17
Gd	2.92	2.94	2.25	2.24	5.64	5.44	2.46	2.49	1.15	1.14
Tb	0.78	0.78	0.39	0.39	0.90	0.87	0.59	0.60	0.15	0.15
Dy	2.05	2.07	2.27	2.26	4.77	4.60	2.46	2.49	0.51	0.51
Ho	0.69	0.69	0.54	0.54	1.08	1.04	0.79	0.80	0.19	0.19
Er	1.20	1.21	1.59	1.59	2.69	2.60	1.77	1.80	0.53	0.53
Tm	0.48	0.48	0.26	0.26	0.45	0.43	0.49	0.50	0.12	0.12
Yb	1.21	1.22	1.60	1.60	2.57	2.48	1.77	1.80	0.48	0.48
Lu	0.45	0.45	0.27	0.27	0.41	0.39	0.49	0.50	0.12	0.12

Table 4.5: Chemical analysis data (major oxides in wt%, trace elements in ppm) of the Gargaresh Formation at station no.5 (Az Zawiyah)

Location	Az Zawiyah									
Member	Karrot Member								Kaam Member	
Unit	Unit1		Unit2		Unit3		Unit4			
Sample No.	5a	5b	5c	5d	5e	5f	5g	5h	5i	5j
SiO <sub>2</sub>	12.00	12.67	30.74	31.82	4.33	4.53	28.67	27.49	5.09	4.96
TiO <sub>2</sub>	0.04	0.04	0.17	0.15	0.03	0.03	0.12	0.12	0.02	0.01
Al <sub>2</sub> O <sub>3</sub>	1.26	1.37	4.06	4.21	1.57	1.61	3.63	3.51	1.76	1.71
Fe <sub>2</sub> O <sub>3</sub>	0.26	0.30	0.41	0.25	0.42	0.31	0.88	0.67	0.11	0.10
MgO	1.35	1.27	0.18	0.11	1.62	1.50	0.26	0.34	1.41	1.70
CaO	46.95	45.71	30.90	30.96	52.60	50.72	31.95	32.46	50.50	50.81
Na <sub>2</sub> O	0.29	0.21	0.84	0.62	0.51	0.61	0.92	1.13	0.66	0.78
K <sub>2</sub> O	0.92	0.91	1.94	1.84	0.08	0.08	1.83	1.76	0.03	0.03
SO <sub>3</sub>	0.01	0.01	0.01	0.01	0.01	0.01	0.01	0.01	0.01	0.01
Cl	0.29	0.21	0.83	0.60	0.55	0.63	0.92	1.15	0.67	0.79
P <sub>2</sub> O <sub>5</sub>	0.02	0.03	0.01	0.01	0.02	0.02	0.01	0.01	0.01	0.01
LOI	36.39	37.20	29.90	29.37	37.70	39.53	30.50	31.27	39.01	39.07
Total	99.78	99.93	99.99	99.95	99.44	99.58	99.70	99.92	99.28	99.98
Sr	2346	2284	1252	1255	5680	5477	1242	1261	3200	3220
Ni	18.98	20.64	21.86	22.66	25.12	25.76	17.91	17.31	27.13	26.36
Co	381.53	414.84	493.89	415.83	421.20	442.12	358.28	346.44	632.52	614.56
Cu	52.54	57.12	46.93	48.67	87.83	90.07	45.09	43.60	80.18	77.90
Zn	100.42	109.18	70.91	77.11	159.68	163.75	74.65	72.18	137.92	134.00
Pb	26.53	25.83	17.72	17.75	40.04	38.61	19.94	20.25	33.08	33.29
Zr	402.76	436.07	550.12	472.06	477.43	498.35	414.51	402.67	669.89	651.93
Th	73.77	78.35	103.16	104.90	144.06	146.30	101.32	99.83	117.55	115.27
U	28.11	29.66	37.91	38.50	51.55	52.29	37.31	36.79	42.72	41.94
La	21.71	21.14	13.36	13.39	28.46	27.45	13.51	13.72	49.00	49.30
Ce	39.55	38.50	40.32	40.40	56.77	54.74	40.24	40.88	54.04	54.37
Pr	5.22	5.08	3.06	3.07	7.12	6.87	3.26	3.31	6.38	6.42
Nd	18.92	18.42	11.95	11.98	28.85	27.82	12.07	12.26	18.14	18.25
Sm	3.58	3.48	2.36	2.36	5.94	5.73	2.59	2.63	2.87	2.89
Eu	1.40	1.36	0.69	0.69	1.76	1.70	0.86	0.88	0.17	0.17
Gd	2.88	2.80	2.21	2.22	5.55	5.35	2.40	2.43	1.13	1.14
Tb	0.77	0.75	0.39	0.39	0.89	0.85	0.57	0.58	0.15	0.15
Dy	2.03	1.97	2.23	2.23	4.70	4.53	2.40	2.43	0.51	0.51
Ho	0.68	0.66	0.53	0.53	1.06	1.02	0.77	0.78	0.18	0.19
Er	1.19	1.16	1.56	1.57	2.65	2.55	1.72	1.75	0.53	0.53
Tm	0.47	0.46	0.26	0.26	0.44	0.42	0.48	0.49	0.12	0.12
Yb	1.20	1.17	1.57	1.58	2.53	2.44	1.72	1.75	0.48	0.48
Lu	0.44	0.43	0.27	0.27	0.40	0.39	0.48	0.49	0.12	0.12

Table 4.6: Chemical analysis data (major oxides in wt%, trace elements in ppm) of the Gargaresh Formation at station no.6 (El Matered)

Location	El Matered									
Member	Karrot Member								Kaam Member	
Unit	Unit1		Unit2		Unit3		Unit4			
Sample No.	6a	6b	6c	6d	6e	6f	6g	6h	6i	6j
SiO <sub>2</sub>	7.57	6.91	29.61	30.69	3.20	3.40	27.54	26.36	3.96	4.12
TiO <sub>2</sub>	0.04	0.04	0.22	0.29	0.04	0.04	0.18	0.19	0.04	0.04
Al <sub>2</sub> O <sub>3</sub>	0.41	0.49	2.93	3.08	0.44	0.48	2.50	2.38	0.63	0.79
Fe <sub>2</sub> O <sub>3</sub>	0.33	0.48	1.24	1.00	0.28	0.20	0.94	0.92	0.19	0.25
MgO	2.31	2.56	1.00	0.84	2.75	2.63	1.39	1.47	2.54	2.38
CaO	48.00	48.35	31.72	31.69	53.73	51.85	33.08	33.59	51.63	51.47
Na <sub>2</sub> O	0.30	0.01	0.75	0.73	0.29	0.28	0.73	0.68	0.16	0.23
K <sub>2</sub> O	0.14	0.14	0.81	0.71	0.09	0.09	0.70	0.63	0.06	0.06
SO <sub>3</sub>	0.02	0.02	0.02	0.02	0.02	0.02	0.03	0.03	0.03	0.03
Cl	0.48	0.17	0.76	0.73	0.28	0.30	0.73	0.69	0.09	0.16
P <sub>2</sub> O <sub>5</sub>	0.03	0.03	0.02	0.02	0.02	0.02	0.02	0.02	0.02	0.02
LOI	40.27	40.43	30.62	30.10	38.83	40.66	31.63	32.40	40.14	39.98
Total	99.90	99.63	99.70	99.90	99.97	99.97	99.47	99.36	99.49	99.53
Sr	2398	2416	1286	1284	5802	5599	1286	1305	3272	3262
Ni	6.18	7.38	15.77	16.58	7.04	7.68	12.33	11.74	9.71	12.18
Co	124.15	148.37	428.60	450.54	230.15	251.07	246.75	234.90	226.42	283.92
Cu	17.10	20.43	33.87	35.61	24.61	26.85	31.05	29.56	28.70	35.99
Zn	32.68	39.05	23.08	27.58	44.75	48.82	51.41	48.94	49.37	61.91
Pb	27.12	27.32	18.19	18.17	40.90	39.47	20.64	20.96	33.82	33.72
Zr	146.52	170.74	505.97	527.91	307.52	328.44	324.12	312.27	263.79	321.29
Th	39.47	42.80	111.24	112.98	101.98	104.22	108.42	106.93	66.07	73.36
U	16.66	17.81	40.60	41.19	37.54	38.27	39.69	39.15	25.57	28.00
La	22.20	22.36	13.72	13.71	29.07	28.06	13.99	14.20	50.10	49.94
Ce	40.43	40.73	41.39	41.36	57.99	55.96	41.66	42.30	55.25	55.08
Pr	5.34	5.38	3.14	3.14	7.27	7.02	3.37	3.42	6.53	6.51
Nd	19.34	19.48	12.27	12.26	29.47	28.44	12.50	12.69	18.54	18.49
Sm	3.66	3.69	2.42	2.42	6.07	5.86	2.68	2.72	2.93	2.93
Eu	1.43	1.44	0.70	0.70	1.80	1.74	0.89	0.91	0.17	0.17
Gd	2.95	2.97	2.27	2.27	5.67	5.47	2.48	2.52	1.15	1.15
Tb	0.78	0.79	0.40	0.40	0.91	0.87	0.60	0.60	0.15	0.15
Dy	2.07	2.09	2.29	2.29	4.80	4.63	2.48	2.52	0.52	0.52
Ho	0.69	0.70	0.55	0.54	1.08	1.05	0.79	0.81	0.19	0.19
Er	1.22	1.23	1.61	1.60	2.71	2.61	1.79	1.81	0.54	0.54
Tm	0.48	0.49	0.27	0.27	0.45	0.43	0.50	0.50	0.12	0.12
Yb	1.23	1.24	1.62	1.61	2.59	2.50	1.79	1.81	0.49	0.49
Lu	0.45	0.46	0.28	0.28	0.41	0.39	0.50	0.50	0.12	0.12

Table 4.7: Chemical analysis data (major oxides in wt%, trace elements in ppm) of the Gargaresh Formation at station no.7 (Sabratak)

Location	Sabratak									
Member	Karrot Member								Kaam Member	
Unit	Unit1		Unit2		Unit3		Unit4			
Sample No.	7a	7b	7c	7d	7e	7f	7g	7h	7i	7j
SiO <sub>2</sub>	12.56	13.23	31.30	32.20	4.89	5.09	29.07	27.89	5.65	5.52
TiO <sub>2</sub>	0.06	0.06	0.15	0.16	0.04	0.04	0.17	0.15	0.03	0.03
Al <sub>2</sub> O <sub>3</sub>	1.82	1.93	4.62	4.59	2.13	2.17	4.03	3.91	2.32	2.27
Fe <sub>2</sub> O <sub>3</sub>	0.29	0.31	0.25	0.28	0.55	0.67	0.76	0.72	0.16	0.19
MgO	0.79	0.71	0.11	0.09	1.06	0.94	0.15	0.23	0.85	1.14
CaO	46.39	45.15	30.90	30.94	52.04	50.16	31.84	32.35	49.94	50.25
Na <sub>2</sub> O	0.15	0.12	0.14	0.06	0.87	0.57	0.58	0.61	1.22	0.73
K <sub>2</sub> O	1.48	1.47	2.50	2.22	0.11	0.12	2.23	2.16	0.09	0.09
SO <sub>3</sub>	0.03	0.03	0.04	0.04	0.04	0.04	0.01	0.01	0.02	0.02
Cl	0.15	0.12	0.13	0.04	0.88	0.59	0.59	0.65	1.23	0.74
P <sub>2</sub> O <sub>5</sub>	0.04	0.04	0.03	0.03	0.03	0.04	0.02	0.02	0.02	0.02
LOI	35.83	36.64	29.81	29.39	37.14	38.97	30.39	31.16	38.45	38.51
Total	99.59	99.81	99.98	100.04	99.78	99.40	99.84	99.86	99.98	99.51
Sr	2318	2256	1252	1254	5619	5416	1237	1257	3165	3184
Ni	27.42	29.08	24.87	24.71	34.08	34.72	19.88	19.29	35.77	35.00
Co	551.10	584.41	675.81	671.42	414.12	435.04	397.76	385.92	833.78	815.81
Cu	75.89	80.47	53.41	53.06	119.15	121.39	50.06	48.57	105.69	103.41
Zn	145.05	153.81	102.44	108.63	216.63	220.70	82.88	80.41	181.80	177.88
Pb	26.21	25.51	17.72	17.74	39.62	38.19	19.87	20.19	32.72	32.92
Zr	568.47	601.78	727.18	722.79	465.49	486.41	449.13	437.29	871.15	853.18
Th	93.26	97.84	104.78	104.43	170.52	172.76	101.43	99.94	143.06	140.78
U	34.65	36.16	38.46	38.33	60.37	61.11	37.33	36.85	51.23	50.48
La	21.45	20.88	13.36	13.38	28.16	27.14	13.46	13.68	48.46	48.76
Ce	39.07	38.03	40.32	40.38	56.16	54.14	40.10	40.74	53.44	53.77
Pr	5.16	5.02	3.06	3.06	7.04	6.79	3.25	3.30	6.31	6.35
Nd	18.69	18.19	11.95	11.97	28.54	27.51	12.03	12.22	17.94	18.05
Sm	3.54	3.44	2.36	2.36	5.88	5.67	2.58	2.62	2.84	2.86
Eu	1.38	1.34	0.69	0.69	1.74	1.68	0.86	0.87	0.16	0.16
Gd	2.85	2.77	2.21	2.21	5.49	5.29	2.39	2.43	1.12	1.12
Tb	0.76	0.74	0.39	0.39	0.88	0.85	0.57	0.58	0.14	0.15
Dy	2.00	1.95	2.23	2.23	4.65	4.48	2.39	2.43	0.50	0.50
Ho	0.67	0.65	0.53	0.53	1.05	1.01	0.76	0.78	0.18	0.18
Er	1.18	1.14	1.56	1.57	2.62	2.53	1.72	1.75	0.52	0.52
Tm	0.47	0.45	0.26	0.26	0.43	0.42	0.48	0.49	0.12	0.12
Yb	1.19	1.15	1.57	1.58	2.51	2.42	1.72	1.75	0.47	0.47
Lu	0.44	0.43	0.27	0.27	0.40	0.38	0.48	0.49	0.12	0.12

Table 4.8: Chemical analysis data (major oxides in wt%, trace elements in ppm) of the Gargaresh Formation at station no.8 (Marsa Zuwaghah)

Location	Marsa Zuwaghah	
Member	Karrot Member	
Unit	Unit I	
Sample No.	8a	8b
SiO <sub>2</sub>	11.68	12.27
TiO <sub>2</sub>	0.05	0.05
Al <sub>2</sub> O <sub>3</sub>	0.93	0.97
Fe <sub>2</sub> O <sub>3</sub>	0.32	0.38
MgO	1.68	1.60
CaO	47.28	46.04
Na <sub>2</sub> O	0.21	0.25
K <sub>2</sub> O	0.59	0.51
SO <sub>3</sub>	0.02	0.02
Cl	0.20	0.26
P <sub>2</sub> O <sub>5</sub>	0.04	0.04
LOI	36.72	37.53
Total	99.72	99.92
Sr	2363	2301
Ni	14.01	14.61
Co	281.61	293.72
Cu	38.78	40.44
Zn	74.12	77.30
Pb	26.71	26.01
Zr	304.98	317.09
Th	62.15	63.81
U	24.27	24.78
La	21.86	21.29
Ce	39.82	38.78
Pr	5.26	5.12
Nd	19.05	18.55
Sm	3.60	3.51
Eu	1.41	1.37
Gd	2.90	2.83
Tb	0.77	0.75
Dy	2.04	1.99
Ho	0.68	0.67
Er	1.20	1.17
Tm	0.48	0.46
Yb	1.21	1.18
Lu	0.45	0.43



Table 4.9: Chemical analysis data (major oxides in wt%, trace elements in ppm) of the Gargaresh Formation at station no.9 (Zuwarah)

Location	Zuwarah	
Member	Karrot Member	
Unit	Unit1	
Sample No.	9a	9b
SiO <sub>2</sub>	7.81	7.15
TiO <sub>2</sub>	0.05	0.05
Al <sub>2</sub> O <sub>3</sub>	0.65	0.73
Fe <sub>2</sub> O <sub>3</sub>	0.27	0.30
MgO	2.07	2.32
CaO	47.76	48.11
Na <sub>2</sub> O	0.60	0.51
K <sub>2</sub> O	0.05	0.05
SO <sub>3</sub>	0.02	0.02
Cl	0.62	0.52
P <sub>2</sub> O <sub>5</sub>	0.04	0.04
LOI	40.03	40.19
Total	99.97	99.99
Sr	2387	2404
Ni	9.79	11.00
Co	196.82	221.05
Cu	27.10	30.44
Zn	51.80	58.18
Pb	26.99	27.18
Zr	220.19	244.42
Th	50.47	53.81
U	20.35	21.46
La	22.08	22.25
Ce	40.23	40.52
Pr	5.31	5.35
Nd	19.24	19.39
Sm	3.64	3.67
Eu	1.42	1.43
Gd	2.93	2.95
Tb	0.78	0.79
Dy	2.06	2.08
Ho	0.69	0.70
Er	1.21	1.22
Tm	0.48	0.48
Yb	1.22	1.23
Lu	0.45	0.45

Table 4.10: Chemical analysis data (major oxides in wt%, trace elements in ppm)  
of the Gargaresh Formation at station no.10 (Abu Kammash)

Location	Abu Kammash	
Member	Karrot Member	
Unit	Unit1	
Sample No.	10a	10b
SiO <sub>2</sub>	8.57	7.91
TiO <sub>2</sub>	0.05	0.05
Al <sub>2</sub> O <sub>3</sub>	1.41	1.49
Fe <sub>2</sub> O <sub>3</sub>	0.70	0.91
MgO	1.31	1.56
CaO	47.00	47.35
Na <sub>2</sub> O	0.75	0.55
K <sub>2</sub> O	0.05	0.05
SO <sub>3</sub>	0.02	0.02
Cl	0.79	0.59
P <sub>2</sub> O <sub>5</sub>	0.03	0.03
LOI	39.27	39.43
Total	99.95	99.94
Sr	2349	2366
Ni	21.24	22.45
Co	426.95	451.18
Cu	58.79	62.13
Zn	112.37	118.75
Pb	26.56	26.75
Zr	450.32	474.55
Th	82.16	85.50
U	30.92	32.00
La	21.73	21.90
Ce	39.59	39.88
Pr	5.23	5.27
Nd	18.94	19.08
Sm	3.58	3.61
Eu	1.40	1.41
Gd	2.88	2.91
Tb	0.77	0.77
Dy	2.03	2.04
Ho	0.68	0.68
Er	1.19	1.20
Tm	0.47	0.48
Yb	1.20	1.21
Lu	0.44	0.45

Table 4.11: Chemical analysis data (major oxides in wt%, trace elements in ppm)  
of the Gargaresh Formation at station no.11 (Ras Jdeir)

Location	Ras Jdeir	
Member	Karrot Member	
Unit	Unit1	
Sample No.	11a	11b
SiO <sub>2</sub>	12.09	12.68
TiO <sub>2</sub>	0.03	0.03
Al <sub>2</sub> O <sub>3</sub>	1.34	1.38
Fe <sub>2</sub> O <sub>3</sub>	0.40	0.33
MgO	1.27	1.19
CaO	46.87	45.63
Na <sub>2</sub> O	0.23	0.30
K <sub>2</sub> O	1.00	0.92
SO <sub>3</sub>	0.03	0.03
Cl	0.24	0.32
P <sub>2</sub> O <sub>5</sub>	0.05	0.05
LOI	36.31	37.12
Total	99.86	99.98
Sr	2342	2280
Ni	20.19	20.79
Co	405.76	417.87
Cu	55.87	57.54
Zn	106.79	109.98
Pb	26.48	25.78
Zr	429.13	441.24
Th	79.24	80.91
U	29.93	30.51
La	21.67	21.10
Ce	39.48	38.43
Pr	5.21	5.07
Nd	18.89	18.39
Sm	3.57	3.48
Eu	1.39	1.36
Gd	2.88	2.80
Tb	0.77	0.75
Dy	2.02	1.97
Ho	0.68	0.66
Er	1.19	1.16
Tm	0.47	0.46
Yb	1.20	1.17
Lu	0.44	0.43

Table 4.12: Correlation matrix of the studied samples

Oxides and Elements	SiO <sub>2</sub>	TiO <sub>2</sub>	Al <sub>2</sub> O <sub>3</sub>	Fe <sub>2</sub> O <sub>3</sub>	MgO	CaO	Na <sub>2</sub> O	K <sub>2</sub> O	SO <sub>3</sub>	Cl	P <sub>2</sub> O <sub>5</sub>	LOI	Sr	Ni	Co	Cu	Zn	Pb	Zr	Th	U	REE		
SiO <sub>2</sub>	1.00																							
TiO <sub>2</sub>	0.91	1.00																						
Al <sub>2</sub> O <sub>3</sub>	0.87	0.79	1.00																					
Fe <sub>2</sub> O <sub>3</sub>	0.67	0.69	0.49	1.00																				
MgO	-0.76	-0.66	-0.93	-0.40	1.00																			
CaO	-0.98	-0.91	-0.86	-0.70	0.75	1.00																		
Na <sub>2</sub> O	0.53	0.47	0.57	0.49	-0.50	-0.55	1.00																	
K <sub>2</sub> O	0.76	0.64	0.83	0.26	-0.83	-0.74	0.18	1.00																
SO <sub>3</sub>	-0.11	-0.08	-0.13	-0.05	0.10	0.09	-0.24	-0.10	1.00															
Cl	0.52	0.47	0.55	0.53	-0.49	-0.55	0.97	0.16	-0.16	1.00														
P <sub>2</sub> O <sub>5</sub>	-0.32	-0.28	-0.29	-0.20	0.06	0.33	-0.57	-0.04	0.24	-0.51	1.00													
LOI	-0.98	-0.89	-0.91	-0.62	0.80	0.96	-0.57	-0.78	0.16	-0.53	0.36	1.00												
Sr	-0.79	-0.66	-0.59	-0.50	0.58	0.81	-0.34	-0.57	-0.02	-0.36	0.12	0.68	1.00											
Ni	0.16	0.11	0.55	0.03	-0.71	-0.14	0.32	0.35	-0.05	0.31	0.15	-0.26	-0.05	1.00										
Co	0.25	0.22	0.60	-0.02	-0.70	-0.23	0.32	0.41	-0.10	0.29	0.01	-0.34	-0.12	0.89	1.00									
Cu	-0.10	-0.11	0.32	-0.08	-0.50	0.11	0.23	0.13	-0.04	0.22	0.21	-0.02	0.21	0.95	0.78	1.00								
Zn	-0.19	-0.24	0.22	-0.16	-0.42	0.21	0.12	0.09	-0.01	0.11	0.31	0.09	0.27	0.91	0.71	0.98	1.00							
Pb	-0.90	-0.79	-0.72	-0.60	0.70	0.91	-0.40	-0.67	-0.01	-0.42	0.13	0.82	0.96	-0.12	-0.19	0.16	0.23	1.00						
Zr	0.29	0.27	0.64	0.02	-0.71	-0.27	0.36	0.43	-0.11	0.33	-0.05	-0.39	-0.11	0.88	0.99	0.76	0.68	-0.20	1.00					
Th	0.15	0.23	0.52	0.17	-0.54	-0.14	0.42	0.23	-0.10	0.40	-0.14	-0.29	0.23	0.78	0.69	0.81	0.73	0.09	0.74	1.00				
U	0.15	0.23	0.52	0.17	-0.54	-0.14	0.42	0.23	-0.10	0.40	-0.14	-0.29	0.23	0.78	0.69	0.81	0.73	0.09	0.74	0.97	1.00			
REE	-0.85	-0.73	-0.65	-0.61	0.65	0.86	-0.31	-0.65	-0.04	-0.36	-0.02	0.76	0.92	-0.08	-0.12	0.17	0.22	0.97	-0.12	0.16	0.15	1.00		

Table 4.13: Descriptive statistics of the studied samples (major oxides in wt%, trace elements in ppm)

Oxides and Elements	N	Minimum	Maximum	Mean	Std. Deviation
SiO <sub>2</sub>	71	2.93	32.20	14.48	11.03
TiO <sub>2</sub>	71	0.01	0.29	0.08	0.06
Al <sub>2</sub> O <sub>3</sub>	71	0.17	4.62	1.76	1.24
Fe <sub>2</sub> O <sub>3</sub>	71	0.09	1.24	0.48	0.31
MgO	71	0.09	3.02	1.59	0.82
CaO	71	30.90	54.00	43.58	8.58
Na <sub>2</sub> O	71	0.01	1.22	0.52	0.32
K <sub>2</sub> O	71	0.01	2.50	0.57	0.67
SO <sub>3</sub>	71	0.01	0.31	0.03	0.05
Cl	71	0.04	1.23	0.54	0.32
P <sub>2</sub> O <sub>5</sub>	71	0.01	0.05	0.02	0.01
LOI	71	29.37	40.93	36.20	4.11
Sr	71	1007.00	5831.00	2689.83	1483.13
Ni	71	2.72	35.77	15.71	8.12
Co	71	88.92	833.78	344.89	167.57
Cu	71	9.51	121.39	43.54	25.18
Zn	71	17.29	220.70	75.94	47.09
Pb	71	15.93	41.11	27.61	7.55
Zr	71	128.15	871.15	388.82	169.41
Th	71	35.11	172.76	87.47	29.57
U	71	15.25	61.11	32.69	9.86
REE	71	80.76	151.04	108.82	24.90

The graphical presentation of the correlation coefficients among the analyzed major oxides points to the intimate coherence among them, except for CaO and MgO (Fig. 4.1). Silica, alumina, iron oxide, chlorine and potash are most probably accommodated within terrestrial admixture.

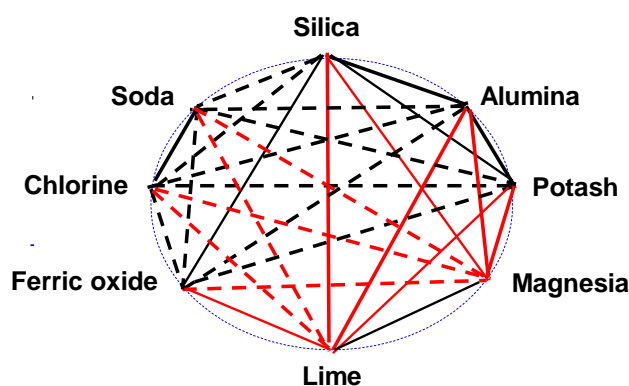


Fig. 4.1: Correlations among the major oxides in the studied samples (intensity of lines corresponds to the strength of the correlation coefficient (< 0.4 to > 0.8)) (red line means inverse relation)

The plot of silica versus alumina suggests that silica and alumina are strongly correlated in the studied formation ( $r = 0.87$ , Fig. 4.2). This reflects the occurrence of silica in both silicate and free silica modes. Preda and Cox (2005) found that quartz and shell-rich sediments tend to have smaller amounts of Al in the shallow marine sediments in the Gulf of Carpentaria, Northern Australia.

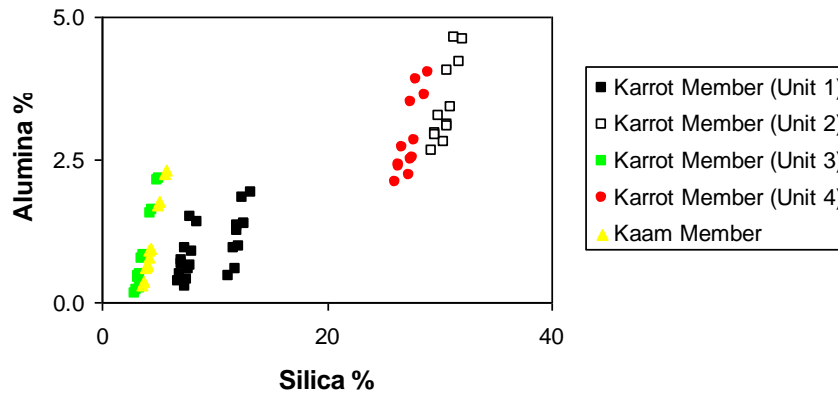


Fig. 4.2: Relationship between silica and alumina in the study area

Aluminum concentration is a reasonably good measure of detrital flux. The studied calcarenite samples, except units 1 and 3 of Karrot Member and some samples of Kaam Member, show higher concentrations of  $\text{Al}_2\text{O}_3$  than the siliciclastic contaminated carbonates ( $\text{Al}_2\text{O}_3$  concentration of 1.59%, in Veizer, 1983).

The positive correlation between  $\text{K}_2\text{O}$  and  $\text{Al}_2\text{O}_3$  ( $r = 0.83$ , Fig. 4.3) suggests in agreement with Zhang (2004) and Nagarajan *et al.*, (2007) that they are bound to alumino-silicate minerals and associated phases and, therefore, they have been concentrated during weathering processes.

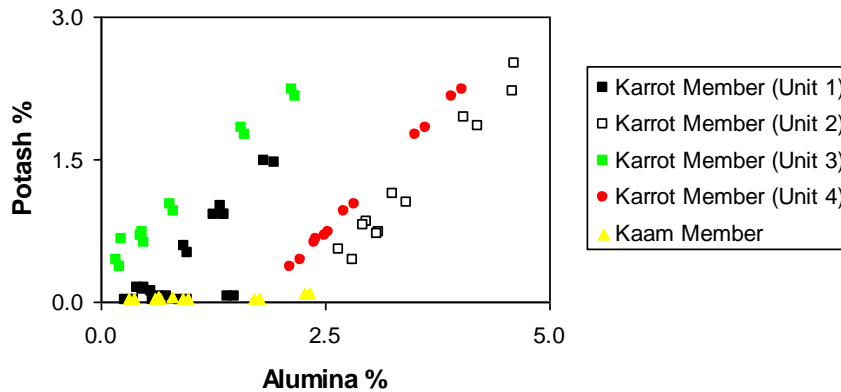


Fig. 4.3: Relationship between alumina and potash in the study area

The  $K_2O/Al_2O_3$  ratio is important in sedimentary rocks in understanding the source of aluminum and its distribution between clay and feldspars minerals (Katongo *et al.*, 2004). The  $K_2O/Al_2O_3$  ratios for clay minerals and feldspars are different (0.0 to 0.3, 0.3 to 0.9, respectively; Cox *et al.*, 1995). In the studied samples, the  $K_2O/Al_2O_3$  ratio ranges from 0.01 to 0.81, indicating that both clay minerals and feldspars have a major role in the distribution of aluminum in the study area.

CaO is strongly correlated with MgO ( $r = 0.75$ , Fig. 4.4). This relationship means that calcite is the sole carrier of MgO. The studied samples show very low MgO/CaO ratio (0.03, in average). This low value indicates that the studied samples are not dolomitized, because dolomitization would necessarily cause a marked increase in the MgO/CaO ratio of the limestone.

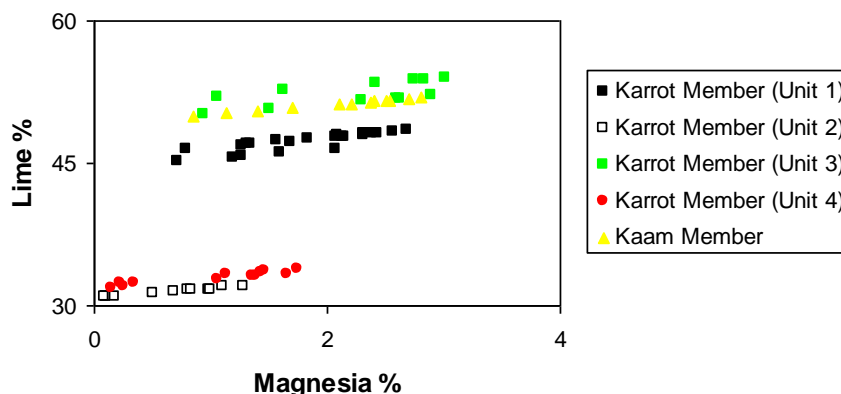


Fig. 4.4: Relationship between magnesia and lime in the study area

Titanium is mainly concentrated in phyllosilicates (Condie *et al.*, 1992) and is relatively immobile compared to other elements during various sedimentary processes and may strongly represent the source rocks (McLennan *et al.*, 1993). The studied samples have low  $\text{TiO}_2$  contents. Figs (4.5-6) show that  $\text{TiO}_2$  is positively correlated with  $\text{Al}_2\text{O}_3$  and  $\text{Fe}_2\text{O}_3$  (except units 2 and 4 of Karrot Member,  $r = 0.79$  and  $0.69$ , respectively) suggesting in agreement with Condie *et al.*, (1992) and Carranza-Edwards *et al.*, (2009) that Ti is contained in both iron minerals and alumino-silicate. In agreement with Shaltami (2012) these correlations may be a result of sorting under control of the depositional environments. In the present study, the  $\text{TiO}_2/\text{Zr}$  ratio ranges from 0.15 to 6.1. According to Garcia *et al.*, (1994), Asiedu *et al.*, (2000) and Malick and Ishiga (2015), mature sediments show a wide range of  $\text{TiO}_2/\text{Zr}$  variations whereas immature sediments show a more limited range of  $\text{TiO}_2/\text{Zr}$  variations.

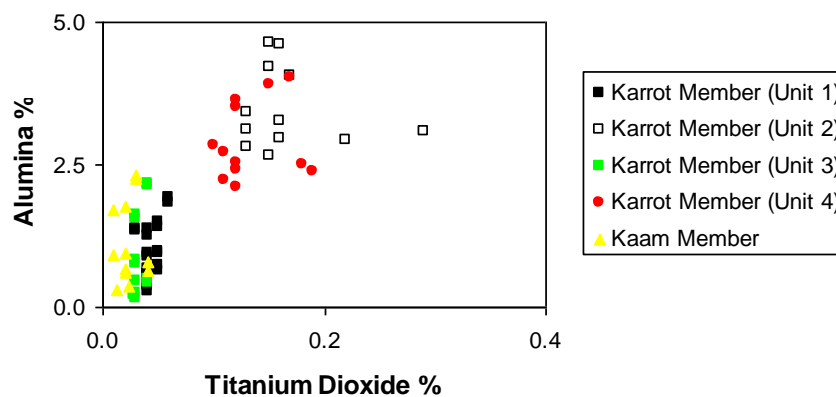


Fig. 4.5: Relationship between titanium dioxide and alumina in the study area

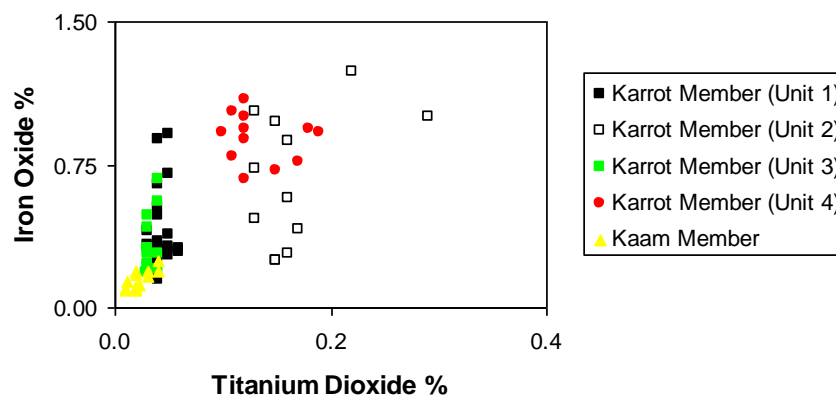


Fig. 4.6: Relationship between titanium dioxide and iron oxide in the study area



Many authors (e.g., Gandhi and Raja, 2014) suggest that Na present in the original carbonate sediments can be modified greatly during diagenesis. The strong positive correlation between Na<sub>2</sub>O and Cl ( $r = 0.97$ , Fig. 4.7) supports their accommodation in the form of halite.

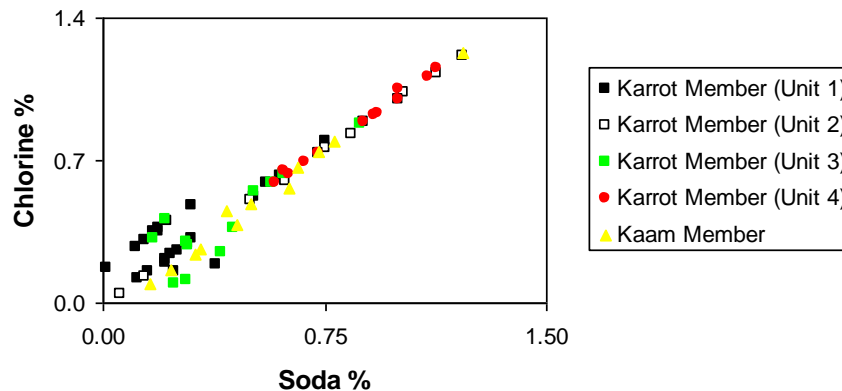


Fig. 4.7: Relationship between soda and chlorine in the study area

#### 4.4. Trace elements

The study of trace elements have become a vital part in modern petrology and more capable for discrimination between petrological processes than the major elements. The behavior of trace elements during sedimentary processes is complex due to many factors including weathering, physical sorting, adsorption, provenance, diagenesis, and metamorphism (Papadopoulos *et al.*, 2015). However, the behavior of trace elements in chemical weathering processes is still not fully understood (Feng, 2011). The geochemical behavior of trace elements during weathering processes cannot easily be generalized because of (1) the wide variation in trace-element-bearing mineral assemblages and their different weathering resistance, and (2) the location-specific weathering environment (Bao and Zhao, 2008).

##### 4.4.1. Low field strength elements (LFSE)

They are large cations of small charge and tend to be compatible with major elements. The low ionic potential (ratio of charge to ionic radius) makes these elements relatively soluble in aqueous solution. Because of their solubility, they are quite mobile during metamorphism and weathering (White, 2001). LFSE include four elements namely, Rb, Cs, Ba and Sr.

The Sr content in carbonate minerals may be used as an important chemical characteristic to identify their genesis. The aragonitic carbonate sediments are better accumulator of Sr than the calcitic ones, essentially because the higher coordination of  $\text{Ca}^{2+}$  ion in the former. On calcite,  $\text{Sr}^{2+}$  sorption occurs by electrostatic attraction as hydrated ions. However, at higher concentrations, precipitation of strontianite ( $\text{SrCO}_3$ ) occurs, and Sr is likely to be less mobile (Parkman *et al.*, 1998). During an X-ray spectroscopic study of coral skeletons, Greigor *et al.*, (1997) found that 40% of Sr present as strontianite and 60% Sr substituted for Ca in aragonite structures.

In the present study, the high Sr content in the calcarenite samples indicates that Sr may be associated with calcite. This assumption is confirmed by the strong correlation between CaO and Sr ( $r = 0.81$ , Fig. 4.8).

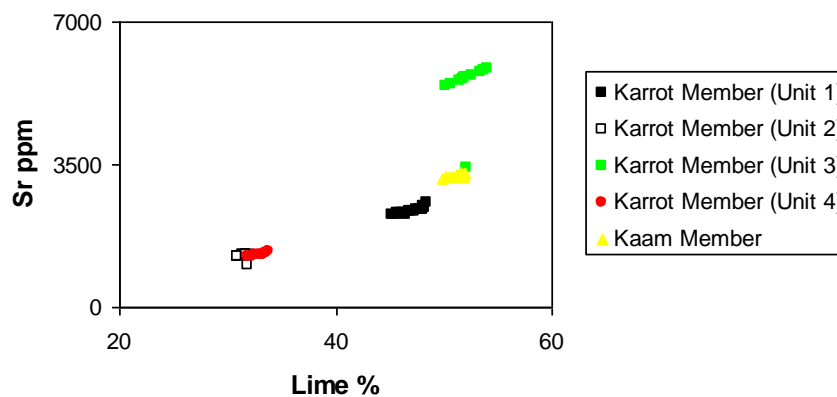


Fig. 4.8: Relationship between Lime and strontium in the study area

#### 4.4.2. Heavy metals

According to Anderson (2003), heavy metals are stable metals or metalloids and cannot be degraded or destroyed. Therefore, they tend to accumulate in soils and sediments. However, anthropogenic activities have drastically altered the biochemical and geochemical cycles and the balance of some heavy metals. The analyzed heavy metals in the studied samples are Ni, Co, Cu, Zn and Pb.

In the studied formation, Pb correlates strongly with CaO ( $r = 0.91$ , Fig. 4.9). This relationship means that calcite is the sole carrier of Pb.

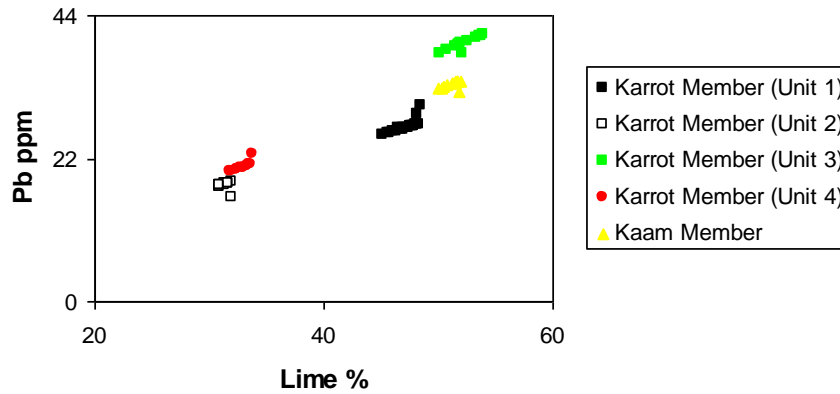


Fig. 4.9: Relationship between lime and lead in the study area

Ni, Co, Cu and Zn are normally associated with mafic rocks and could also be associated with felsic rock. Zn tends to replace Fe and Mg in the rock forming minerals. In the present study, Ni, Co, Cu and Zn are mutually correlated (*see* Table 4.12). The weak negative correlations between Ni, Co, Cu and Zn with  $Fe_2O_3$  indicate that iron minerals are not the sole carrier of these heavy metals (*see* Table 4.12). Ni, Co, Cu and Zn are strongly correlated with  $Al_2O_3$  (Figs. 4.10-13) suggesting, in agreement with Fedo *et al.*, (1996) and Al Shariani (2006), their possible accommodation as aluminosilicates which can be concentrated during weathering.

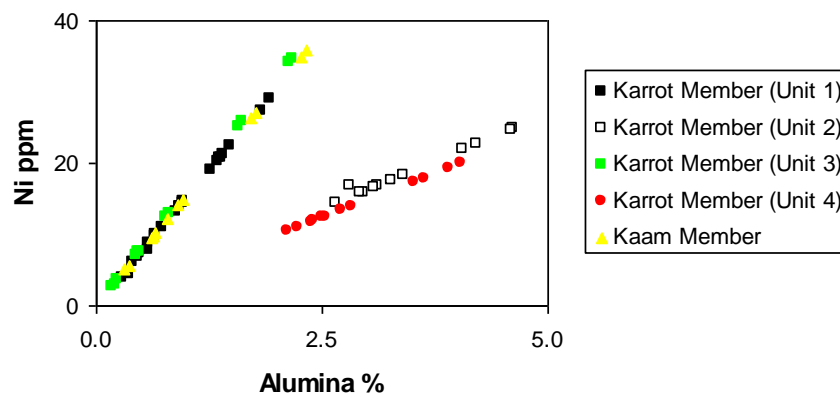


Fig. 4.10: Relationship between alumina and nickel in the study area

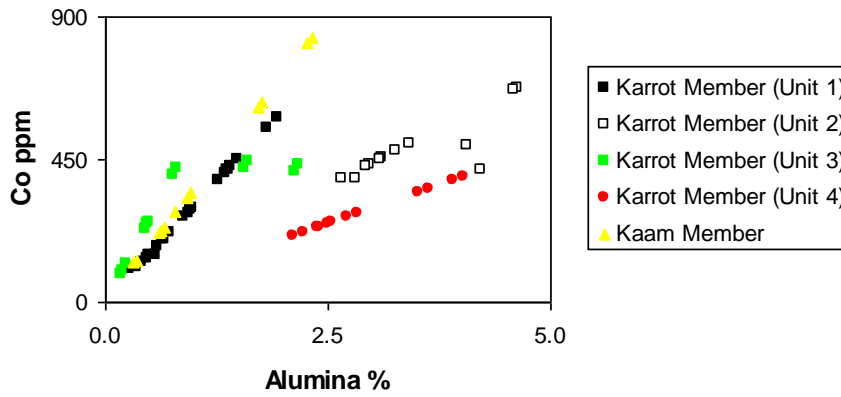


Fig. 4.11: Relationship between alumina and cobalt in the study area

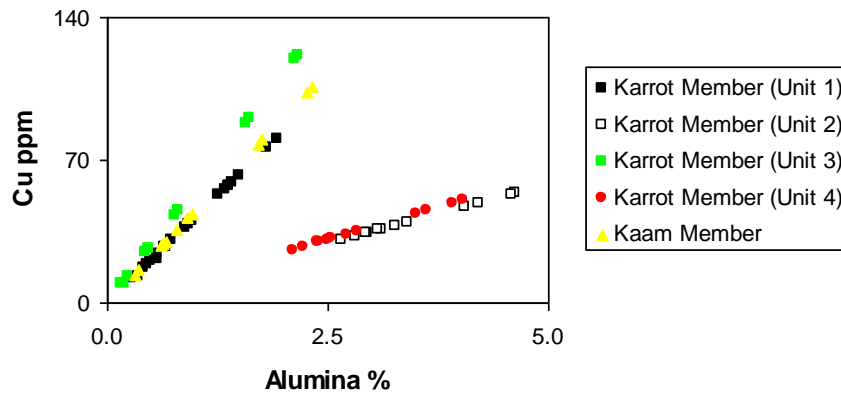


Fig. 4.12: Relationship between alumina and copper in the study area

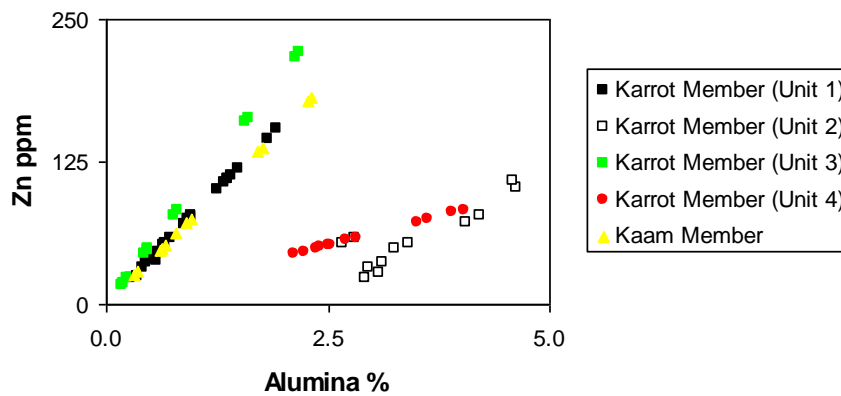


Fig. 4.13: Relationship between alumina and zinc in the study area

The Cu/Zn and Ni/Co ratios are used as a redox parameter in many studies (e.g., Jones and Manning, 1994; El-Kammar *et al.*, 2007; Shaltami, 2012). According to

Hallberg (1976) the increasing value of the Cu/Zn ratio indicates a reducing depositional condition while decreasing Cu/Zn values suggest increased oxidizing conditions. Ni/Co ratios below 5 indicate oxic environments, whereas ratios above 5 suggest suboxic and anoxic environments (Jones and Manning, 1994). The studied calcarenite samples show low Cu/Zn and Ni/Co ratios (0.61 and 0.05, in average, respectively) which suggest that these sediments were deposited in a well oxygenated environment.

#### **4.4.3. High field strength elements (HFSE)**

They are highly charged cations and often have appropriate size for many cation sites in minerals. Their charge is too high and requires one or more coupled substitution to maintain charge balance; this is generally energetically unfavorable (White, 2001). Thus HFSE are incompatible elements as they have high ionic potential, they are insoluble and tend to be very immobile during weathering and metamorphism. HFSE include six elements namely, Zr, Hf, Nb, Ta, Th and U. Lopez *et al.*, (2005) reported that the highest abundance of HFSE associates the silts which imply that accessory minerals, such as zircon and Nb-bearing phases are mainly concentrated in silt lithology. The high silica rocks tend to contain higher concentrations of HFSE than the basic rocks (Chandrajith, *et al.*, 2000). The HFSE provide a series of the geochemical isovalents (Zr-Hf, Nb-Ta and Th-U). The mutual abundance and distribution of these isovalents in most geologic environments follow the popularly known Goldschmidt's rule which is based on the charge and radius control (i.e., CHARAC). The non-CHARAC behavior of the isovalents is important in interpreting geological environments. The ratios between isovalents have the advantage that they do not change with time as isotopic ratios do (Condie, 2005).

In the studied samples, Th always dominates over U. Uranium is mainly fractionated from thorium in near surface environment (Whittaker and Kyser, 1993). Uranium is mobilized as  $U^{+6}$  in oxic environment and precipitated as  $U^{+4}$  in reducing environments (Anderson *et al.*, 1983), as compared to the relatively immobile Th, which is concentrated in residual materials. In the present study, Th and U are strongly correlated ( $r = 0.97$ , Fig. 4.14). The Th/U ratio in the studied formation (2.64, in average) approximately resembles the chondritic value (3, by

McLennan *et al.*, 1993). In most cases, weathering and sedimentary recycling typically result in loss of U, leading to an elevation in the Th/U ratio.

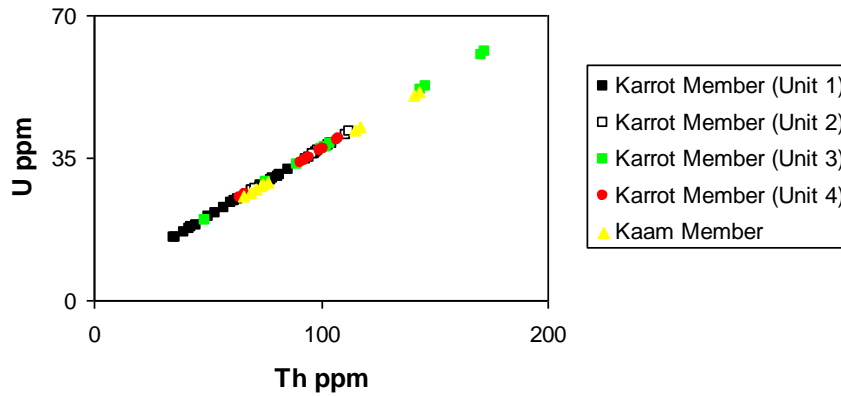


*Fig. 4.14: Relationship between thorium and uranium in the study area*

The weak correlations between Th and U with  $\text{Al}_2\text{O}_3$  ( $r = 0.52$  and  $0.53$ , respectively) indicate that aluminosilicates are not the sole carrier of Th and U. Figs (4.15-16) show that Th and U are positively correlated with Zr ( $r = 0.74$  and  $0.73$ , respectively) suggesting that Th and U are contained in zircon.

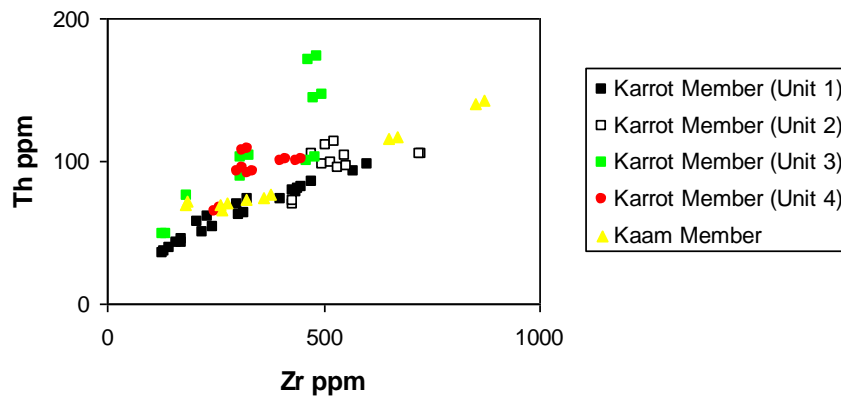


*Fig. 4.15: Relationship between zirconium and thorium in the study area*

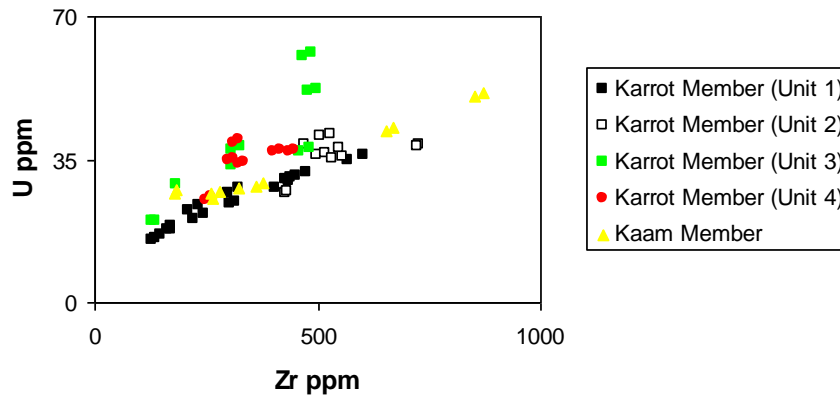


Fig. 4.16: Relationship between zirconium and uranium in the study area

The studied calcarenite samples show low contents of U (from 15.25 to 61.11 ppm). The sediments deposited in oxygenated marine environment generally show low contents of U (Madhavaraju and Ramasamy, 1999), whereas high U contents are generally found in sediments from the oxygen minimum zone (Barnes and Cochran, 1990; Nath *et al.*, 1997). The low contents of U in the studied samples are due to the mobilization of  $U^{+6}$  from sediments to water column under oxic environments.

The U/Th ratio and authigenic uranium are used as a redox parameter in many studies (e.g., Jones and Manning, 1994; Nagarajan *et al.*, 2007; Shaltami, 2012). U/Th ratios below 1.25 suggest oxic conditions of deposition, whereas values above 1.25 indicate suboxic and anoxic conditions (Nath *et al.*, 1997). According to Nagarajan *et al.*, (2007), in the Arabian Sea, sediments below the oxygen minimum zone (OMZ) show high U/Th ( $>1.25$ ) ratios, whereas the sediments above the OMZ exhibit low U/Th ( $<1.25$ ) ratios. The authigenic uranium content is calculated as: (authigenic U) =  $[U - Th/3]$ . Values of authigenic U below 5 are thought to represent oxic depositional conditions, while values above 5 are indicative of suboxic and anoxic conditions (Nagarajan *et al.*, 2007). The studied calcarenite samples show low values of U/Th ratio and authigenic uranium (0.38 and 3.53, in average, respectively), which indicate that these sediments were deposited in oxic conditions.

#### 4.4.4. Rare earth elements (REE)

The term rare earth elements describes the lanthanides (atomic numbers from 57 to 71), except the naturally unstable promethium (Pm, atomic number 61), that occur in Group IIIA of the Periodic Table. The REE include 14 elements namely; lanthanum (La), cerium (Ce), praseodymium (Pr), neodymium (Nd), samarium (Sm), europium (Eu), gadolinium (Gd), terbium (Tb), dysprosium (Dy), holmium (Ho), erbium (Er), thulium (Tm), ytterbium (Yb) and lutetium (Lu). The REE are divided into two groups, namely; the light rare earth elements (LREE), from La to Eu, and heavy rare earth elements (HREE), from Gd to Lu. The REE content of the studied samples follows the order: Ce > La > Nd > Sm > Dy > Gd > Yb > Eu > Ho > Lu. Y and Sc have been recognized as pseudolanthanides. Geochemically, these two elements are traditionally considered as heavy rare earth elements, because their properties are similar to HREE. The commonest oxidation state of the REE is the trivalent, with Eu which may also exist in the divalent state and Ce in the tetravalent state. These two exceptions of Eu and Ce provide a significant tool for interpreting the redox controls. There is a gradual decrease in ionic radii with increasing atomic number, known as the lanthanide contraction.

The distribution of REE in marine waters, sediments and carbonate rocks has been discussed by many workers (Piper, 1974; Klinkhammer *et al.*, 1983; De Baar *et al.*, 1988; Elderfield *et al.*, 1990; Madhavaraju and Ramasamy, 1999; Nothdurft *et al.*, 2004; Madhavaraju and Lee, 2009; Madhavaraju and Gonzalez-Leon, 2012). The concentrations of REE in seawater are principally influenced by different input sources (*e.g.*, terrestrial input from continental weathering and hydrothermal) and scavenging processes related to depth, salinity and oxygen levels (Elderfield, 1988; Greaves *et al.*, 1999). The unique feature of the seawater REE pattern reveals the uniform trivalent behavior of the elements (except Ce and Eu that exhibit multiple valences) and estuarine and marine scavenging processes (Nothdurft *et al.*, 2004).

The analyzed REE include all the naturally occurring 14 rare earth members. In general, the studied samples are enriched in the LREE over the HREE. The REE are normalized to Post-Archean Australian Shale (PAAS, Taylor and McLennan,



1985). PAAS-normalized REE patterns of the studied samples are shown in Fig. (4.17).

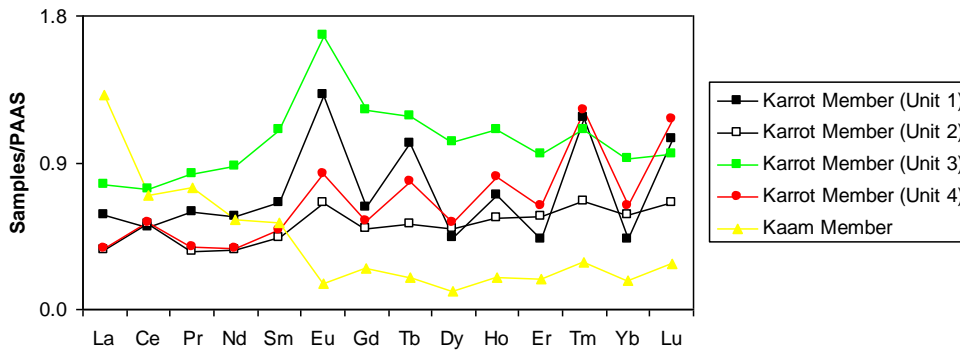


Fig. 4.17: PAAS normalized REE diagram for the studied samples

The REE parameters such as  $\sum\text{REE}$ , LREE/HREE ratios, Ce- and Eu- anomalies (Table 4.14) provide important clues concerning the source, paleo-oxygenation and depositional environment of the studied sediments.

The Ce anomaly ( $\Delta\text{Ce}$ ) content is calculated as:  $\Delta\text{Ce} = \text{Ce}/(\text{La} + \text{Pr})/2$ , while the Eu anomaly ( $\Delta\text{Eu}$ ) content is calculated as:  $\Delta\text{Eu} = \text{Eu}/(\text{Sm} + \text{Gd})/2$ . The contents of La, Pr, Ce, Sm, Eu and Gd used in these equations are PAAS normalized values.

The REE concentrations in the Gargaresh Formation are more than typical marine carbonate value (~28 ppm, by Bellanca, 1997). Karrot Member shows more or less flat REE pattern with positive and negative Ce anomalies ( $\Delta\text{Ce}$ : 0.68 to 1.45, Fig. 4.17 and Table 4.14), while Kaam Member shows convex REE pattern with negative Ce anomalies ( $\Delta\text{Ce}$ : 0.86, Fig. 4.17 and Table 4.14), indicating, in agreement with Hlal and Bennur (2014), Kaam Member (upper member) of aeolian origin and Karrot Member (lower member) of marine origin.

Karrot Member shows both negative and positive Eu anomalies ( $\Delta\text{Eu}$ : 0.39 to 2.05, Fig. 4.17 and Table 4.14), while Kaam Member shows positive Eu anomalies ( $\Delta\text{Eu}$ : 2.05, Fig. 4.17 and Table 4.14).

Table 4.14: REE parameters in the Gargaresh Formation

Location	Member	Unit	LREE	HREE	LREE/HREE	REE	$\Delta\text{Ce}$	$\Delta\text{Eu}$
Tajoura	Karrot Member	Unit1	91.91	9.82	9.36	101.73	0.86	2.05
Tripoli	Karrot Member	Unit1	90.05	7.34	12.27	97.39	0.88	1.77
		Unit2	74.30	9.35	7.95	83.65	1.45	1.41
		Unit3	132.34	18.70	7.08	151.04	0.92	1.44
		Unit4	75.70	11.00	6.88	86.70	1.40	1.63
	Kaam Member	Unit1	134.22	3.29	40.80	137.51	0.68	0.40
Janzour	Karrot Member	Unit1	92.09	9.88	9.32	101.97	0.86	2.04
		Unit2	73.60	9.26	7.95	82.86	1.45	1.40
		Unit3	131.62	18.59	7.08	150.21	0.92	1.44
		Unit4	75.02	10.90	6.88	85.92	1.40	1.62
	Kaam Member	Unit1	133.44	3.28	40.68	136.72	0.68	0.41
Al Mayah	Karrot Member	Unit1	91.48	9.78	9.35	101.26	0.86	2.04
		Unit2	72.91	9.17	7.95	82.08	1.45	1.42
		Unit3	130.87	18.51	7.07	149.38	0.92	1.44
		Unit4	74.33	10.82	6.87	85.15	1.40	1.62
	Kaam Member	Unit1	132.67	3.25	40.82	135.92	0.68	0.41
Az Zawiyah	Karrot Member	Unit1	90.38	9.66	9.36	100.04	0.86	2.05
		Unit2	71.74	9.02	7.95	80.76	1.45	1.42
		Unit3	128.90	18.22	7.07	147.12	0.92	1.44
		Unit4	72.53	10.54	6.88	83.07	1.40	1.62
	Kaam Member	Unit1	130.60	3.22	40.56	133.82	0.68	0.41
El Matered	Karrot Member	Unit1	92.40	9.87	9.36	102.27	0.86	2.05
		Unit2	73.64	9.29	7.93	82.93	1.45	1.40
		Unit3	131.67	18.62	7.07	150.29	0.92	1.44
		Unit4	75.09	10.93	6.87	86.02	1.40	1.62
	Kaam Member	Unit1	133.52	3.28	40.71	136.80	0.68	0.41
Sabratah	Karrot Member	Unit1	89.29	9.56	9.34	98.85	0.86	2.05
		Unit2	71.74	9.02	7.95	80.76	1.45	1.42
		Unit3	127.52	18.03	7.07	145.55	0.92	1.44
		Unit4	72.28	10.51	6.88	82.79	1.40	1.63
	Kaam Member	Unit1	129.15	3.17	40.74	132.32	0.68	0.39
Marsa Zuwaghah	Karrot Member	Unit1	91.00	9.73	9.35	100.73	0.86	2.05
Zuwarah	Karrot Member	Unit1	91.92	9.82	9.36	101.74	0.86	2.05
Abu Kammash	Karrot Member	Unit1	90.47	9.66	9.37	100.13	0.86	2.05
Ras Jdeir	Karrot Member	Unit1	90.21	9.65	9.35	99.86	0.86	2.04

$\Sigma\text{REE}$  correlates strongly with CaO in the calcarenite samples ( $r = 0.86$ , Fig. 4.18), suggesting, in agreement with Fedo *et al.*, (1996) and Nagarajan *et al.*, (2007), that REE may be bound in calcite in the studied samples.

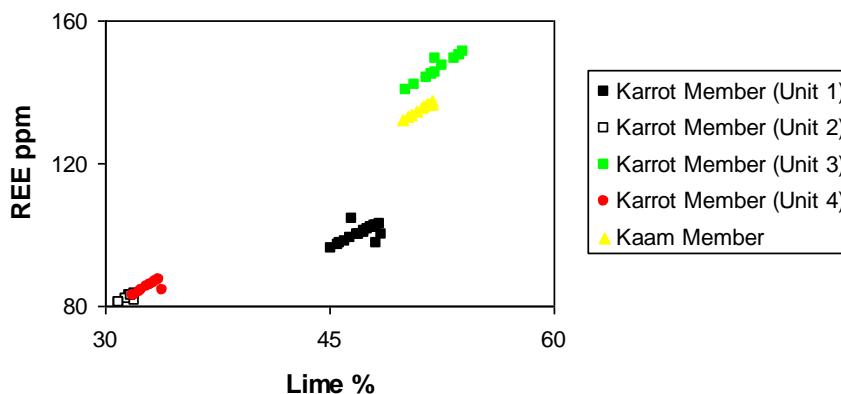
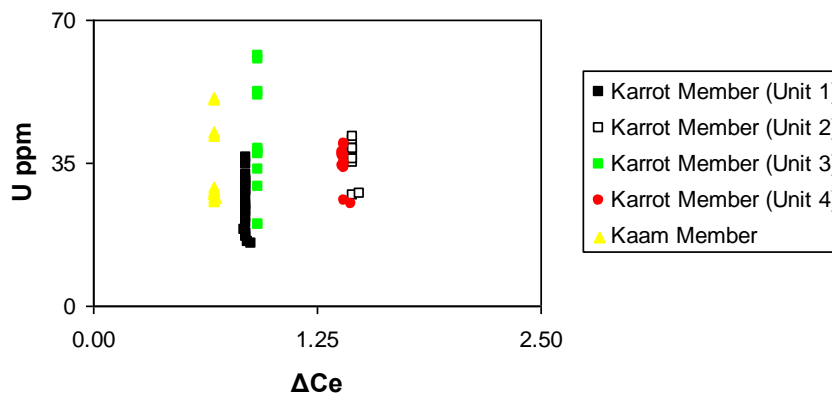


Fig. 4.18: Relationship between lime and total REE in the study area

The Ce anomalies in marine carbonate rocks have been considered as suitable indicator for understanding contemporaneous paleo-redox conditions (Liu *et al.*, 1988). Many studies have been undertaken on Ce behavior in marine phases to unravel paleoceanographic conditions (Liu *et al.*, 1988; Nath *et al.*, 1997; Madhavaraju and Gonzalez-Leon, 2012). As marine water shows negative Ce anomaly, similar Ce anomaly in limestones reveals the inclusion of REE directly from seawater or pore water under oxic condition. The deficiency of Ce relative to neighboring rare earth elements is an important feature of modern seawater. This can be explained by oxidation of trivalent Ce to less soluble tetravalent Ce and successive removal by suspended particles through scavenging process (Sholkovitz *et al.*, 1994). However, Ce is remobilized and released into the water column in the suboxic environment resulting in a less negative to positive anomaly in seawater (De Baar *et al.*, 1991). But, the precise measurements of Ce anomalies in marine sediments may constrain redox conditions at the time and place of deposition (MacLeod and Irving, 1996).

Karrot Member shows both positive and negative Ce anomalies ( $\Delta\text{Ce}$ : 0.68 to 1.45), while Kaam Member shows negative Ce anomalies ( $\Delta\text{Ce}$ : 0.86). Positive Ce anomalies in limestones mainly occur due to detrital input (Madhavaraju and Ramasamy, 1999; Madhavaraju *et al.*, 2010), diagenesis (Armstrong-Altrin *et al.*, 2003), scavenging process (Masuzawa and Koyama, 1989) and paleo-redox conditions (Liu *et al.*, 1988).  $\Delta\text{Ce}$  values are weakly correlated with U ( $r = 0.2$ , Fig. 4.19), which suggest, in agreement with Shaltami (2015), that the  $\Delta\text{Ce}$  values in the

studied samples are not related to the paleo-redox conditions. The extent of diagenetic alterations in the studied samples can be assessed by using immobile trace elements. The samples exhibit a weak correlation between Ce and both Zr and Th ( $r = 0.01$  and  $0.29$ , respectively, Figs. 4.20-21) supporting the diagenetic origin of Ce. In Karrot Member,  $\Delta\text{Ce}$  values are negatively correlated with Pb ( $r = -0.76$ , Fig. 4.22), in agreement with shallow marine depositional environments of Karrot Member.



*Fig. 4.19: Relationship between Ce-anomaly and uranium in the studied samples*

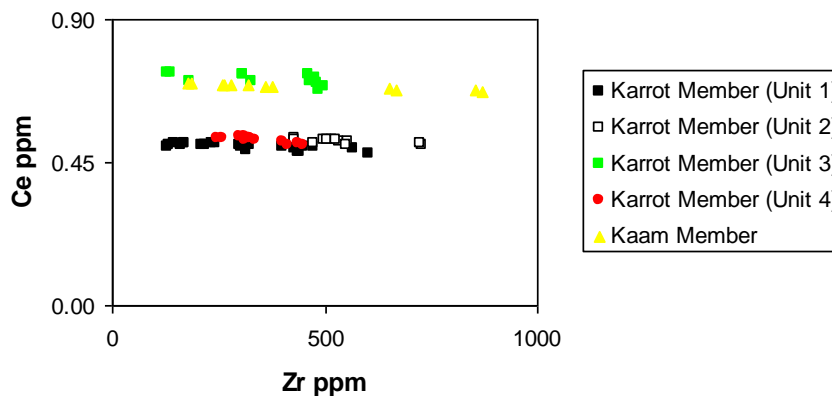


*Fig. 4.20: Relationship between zirconium and cerium in the studied samples*

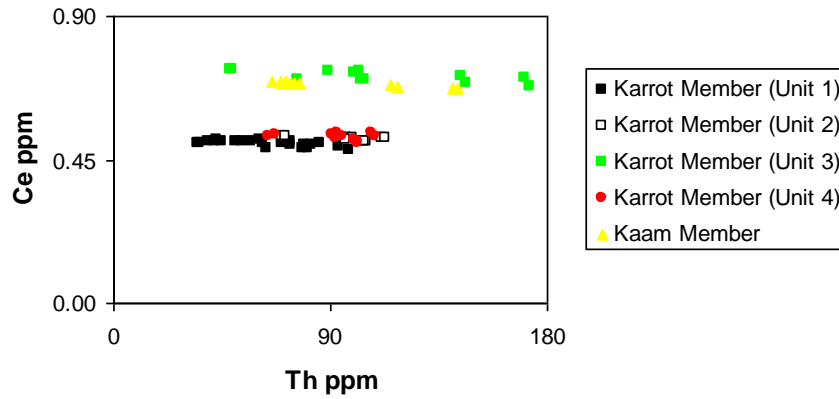


Fig. 4.21: Relationship between thorium and cerium in the studied samples

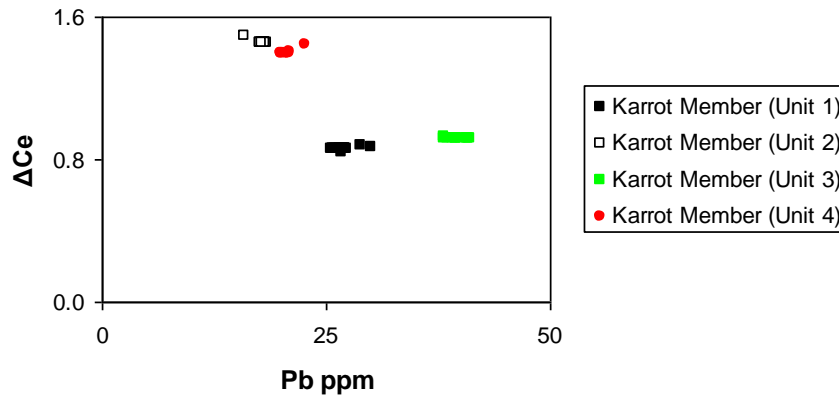


Fig. 4.22: Relationship between Ce-anomaly and lead in the Karrot Member

Most of the studied samples show typical positive Eu anomalies (see Table 4.14). PASS normalized positive Eu anomalies are found in sediments affected by hydrothermal solutions (Michard *et al.*, 1983; German *et al.*, 1993; Kurian *et al.*, 2008), intense diagenesis (MacRae *et al.*, 1992), variations in plagioclase content (Nath *et al.*, 1992) or as result of aeolian input (Elderfield, 1988). The samples exhibit a weak negative correlation between Eu and both Zr and Th ( $r = -0.32$  and  $-0.08$ , Figs. 4.23-24) supporting the diagenetic origin of Eu.

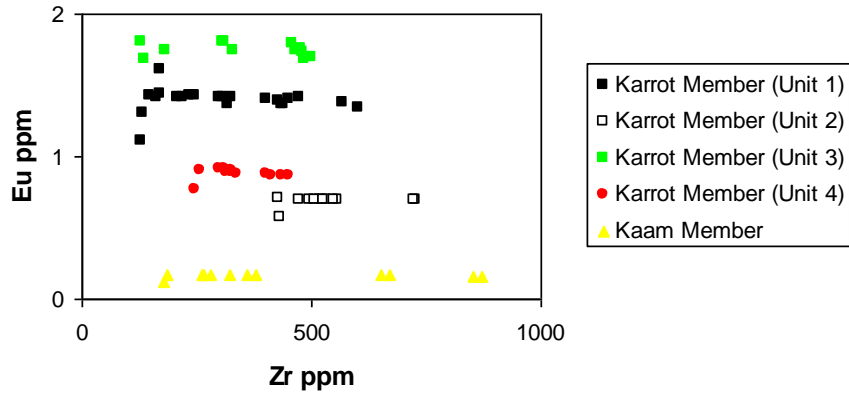


Fig. 4.23: Relationship between zirconium and Eu-anomaly in the studied samples

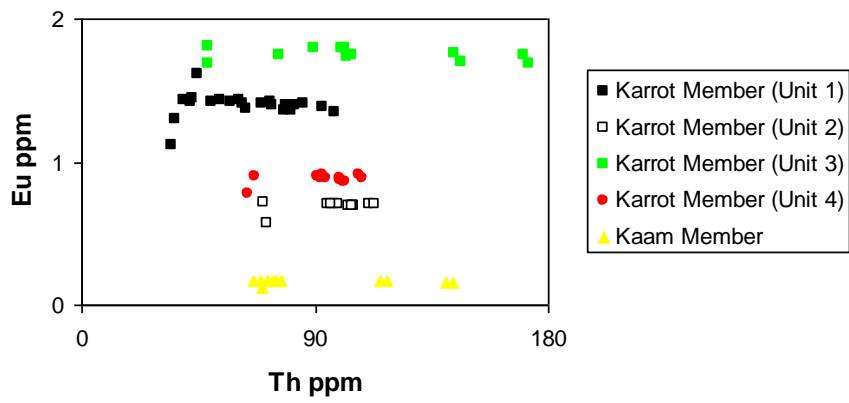


Fig. 4.24: Relationship between thorium and Eu-anomaly in the studied samples

## **CHAPTER FIVE**

### **SUMMARY AND CONCLUSIONS**

The present work attempts to characterize the petrography and geochemistry of the Quaternary calcarenite (Gargaresh Formation) along the Mediterranean Coast from Tajoura to Ras Jdeir, Jifarah plain, NW Libya. Based on the geomorphological characteristics, the studied coastal area can be subdivided into two main physiographic provinces, namely; emerged and submerged shores. The emerged shore extends for about 108 km long, from 5 km east Tajoura (station no. 1) to Marsa Zuwaghah (station no. 8). This area is characterized by irregular shoreline, associated by sea stacks in some places and wave-cut cliffs in others. The wave cut cliffs on the studied area include two formations; Jifarah Formation (calcrete) and Gargaresh Formation (calcarenite). The submerged shore is characterized by its low relief or almost flat coastal area with nearly straight shorelines. It extends from Marsa Zuwaghah to the territorial boundary of Tunisia for about 75 km long. This province is characterized by sandy beach, coastal dunes, thin sand sheets, sabkha deposits and scattered patches of Jifarah and Gargaresh formations.

Samples are collected from the Quaternary calcarenite (Gargaresh Formation) along the Mediterranean Coast from Tajoura to Ras Jdeir, Jifarah plain, NW Libya, from 11 stations (about 71 samples). The traverse is parallel to the studied coast. Petrographic studies comprise microscopic investigations of thin sections and scanning electron microscope (SEM).

The Gargaresh Formation can be subdivided into two members: Kaam Member (upper member) of aeolian origin and Karrot Member (lower member) of marine origin. Both of these members are detected in the studied coast.

The Karrot Member on its cliffs on the shoreline of the study area reaches its maximum thickness in the area between Tripoli and Sabratah. It diminishes towards the west of Sabratah. According to texture, morphology, sedimentary structure and fossil content, the Karrot Member could be divided into four units.

Except unit 1, all other units are only detected from station no. 2 (Tripoli) to station no. 7 (Sabratah).

In the field, unit is hard and range in color from yellowish gray to yellow. This unit is composed essentially of pellets, lumps, shell fragments and abundant fossils. It consists of laminated, graded bedded and considered to be deposited under shore environment. Most outcrops of this unit are dipping seaward and are considered as beach rock. Microscopically, the allochems of this unit are composed of fossils, fossil fragments, pellets and intraclasts with ooids coated by micrite. These are characterized by moderately sorted, medium to coarse grained, well rounded, isopachous and meniscus cements and intergranular porosity (< 5%). The fossil content involves foraminifera (mainly *Elphidium*, *miliolid* and other *rotalid*), bivalve and gastropod shells, echinoderm plate and spine, coralline red algae, bryozoan and ostracoda. The extensive cementation processes such as isopachous bladed calcite crystals growing towards center of pores reduced the porosity.

In the field, unit 2 is composed of brown friable calcarenite rich in shell fragments and land snail (*Helix sp.*). This unit is dipping seaward. Microscopically, the allochems of this unit are composed of pellets, fossils and shell fragments with few intraclasts, characterized by medium to coarse, rounded and moderately sorted. Subrounded quartz grains coated by micrite are observed. The occurrence of quartz grains in this unit may point to an intermittent seaward wind blowing. The fossil contents are shells of bivalve, land snail (*Helix sp.*), foraminifera (*rotalid*, *miliolid* and *Elphidium*), echinoid spines and plates, bryozoans and algae. This unit is generally weakly cemented by isopachous and meniscus cement (point and contact cements) and intergranular and vuge porosity. The loosely packed fabric of this unit and the absence of well-developed cement can be attributed to lack of source and lack of unsuitable geological condition which may indicate that this unit was deposited under wet condition (moist phase). Uniform thin rim from fringing calcite cement surrounding the grains of this unit is indicative of precipitation in phreatic zone, where all pores are filled with water. Also it is a typical feature of low-intertidal and subtidal cements. No sign of sever diagenesis is noticed, however, few quartz grains suffered from percussion probably during transportation. The



transporting agent is possibly wind that could have blown seaward, bringing quartz grains to the site of deposition especially near shore which is otherwise quartz-free.

In the field, unit 3 is composed of white semi-hard calcarenite which commonly displays tabular planar cross bedding, laminated graded and cross bedding. It is also characterized by burrows. Microscopically, the allochems composed of algal peloids, fossils and shell fragments, intraclasts, superficial oololiths, subrounded to subangular quartz grains coated by micrite. Most grains of this unit are well sorted and well rounded. The fossil content is mainly benthonic foraminifera, bivalve shells, echinoderm plate and spine, debris of coralline algae, gastropod, ostracod and bryozoans.

In the field, unit 4 consists of lenses of massive semi-hard calcarenite with abundant land snail (*Helix sp.*). This unit occurs as lenses (wedge shape). Microscopically, the allochems of this unit are composed of shell fragments, pellets mainly fecal pellets of burrowing shrimp, superficial oololiths and intraclasts. Medium to coarse grains, moderately to poorly sorted and poorly washed in which wind-blown angular quartz are imbedded as a matrix in micrite. The compositions of this unit are affected by severe diagenesis and the grains are weakly cemented, oomouldic, vuge, intra- and intergranular porosity. Most grains of this unit are composed of different varieties, such as quartz grains, rounded intraclasts, superficial oololiths and micritized fossils.

The Kaam Member is only detected in the area between Tripoli and Sabratah. It is represented by one unit. It is white semi-hard calcarenite consisting of tabular planar cross bedding. Microscopically, the allochems of this unit consists of pellets mainly fecal pellets of burrowing shrimp, fossils and shell fragments, superficial ooids and intraclasts. Fine to medium grains, moderately well sorted and well rounded. The fossil contents are foraminifera (miliolid and rotalid), bivalves, coralline algae, echinoid spine and plate, ostracod, bryozoans and gastropods. Mouldic, inter- and intragranular porosities represent 10-15%. This unit is partly characterized by alternating lamina of elongate oriented grains (parallel to stratification) and graded bedded laminar structure. Oololiths nuclei are fossils, quartz

grains, rounded micrite fragments or intraclasts. Meniscus and isopachous cements are found in this unit which indicates vadose and phreatic zones precipitation.

There are two types of morphology in the Gargaresh Formation; biogenic and non-biogenic. The biogenic morphology and structures include soft sediment burrows and hard rock borings; plant remains, trails mounds and holes, while the non-biogenic morphology and structures include pre-depositional structures (interbed), syn-depositional structures (intrabed, e.g., massive bedding, cross bedding, lamination and cross lamination), post-depositional structures (deformed interbed and intrabed structures) and miscellaneous structures (cracks).

Analysis of major oxides and trace elements was done by inductively coupled plasma-mass spectrometry (ICP-MS) technique. The data include 12 major oxides and 23 trace elements. The correlation matrix suggests that the heavy metals are possibly of different sources. The Th and U as well as the REE are essentially related to marine and terrestrial inputs. These maximum values, besides the high standard deviation values represent derivation from multi-sources and possible contribution from mineralized sources at the hinterland. The graphical presentation of the correlation coefficients among the analyzed major oxides points to the intimate coherence among them, except for CaO and MgO. Silica, alumina, iron oxide, chlorine and potash are most probably accommodated within terrestrial admixture.

CaO is strongly correlated with MgO, Sr, Pb and  $\sum$ REE. This relationship means that calcite is the sole carrier of MgO, Sr, Pb and REE. The studied samples show very low MgO/CaO ratio (0.03, in average). This low value indicates that the studied samples are not dolomitized.

K<sub>2</sub>O, Ni, Co, Cu and Zn are strongly correlated with Al<sub>2</sub>O<sub>3</sub>, suggesting their possible accommodation as alumino-silicates which can be concentrated during weathering.

The studied calcarenite samples show low authigenic uranium content and low Cu/Zn, Ni/Co and U/Th ratios which suggest that these sediments were deposited in a well oxygenated environment.

The REE concentrations in the Gargaresh Formation are more than typical marine carbonate value (~28 ppm). Karrot Member shows more or less flat REE pattern with positive and negative Ce anomalies ( $\Delta\text{Ce}$ : 0.68 to 1.45), while Kaam Member shows convex REE pattern with negative Ce anomalies ( $\Delta\text{Ce}$ : 0.86), indicating Kaam Member (upper member) of aeolian origin and Karrot Member (lower member) of marine origin.

$\Delta\text{Ce}$  values are weakly correlated with U, which suggest that the  $\Delta\text{Ce}$  values in the studied samples are not related to the paleo-redox conditions. The samples exhibit a weak correlation between Ce and both Zr and Th supporting the diagenetic origin of Ce. In Karrot Member,  $\Delta\text{Ce}$  values are negatively correlated with Pb in agreement with shallow marine depositional environments of Karrot Member.

Karrot Member shows both negative and positive Eu anomalies ( $\Delta\text{Eu}$ : 0.39 to 2.05), while Kaam Member shows positive Eu anomalies ( $\Delta\text{Eu}$ : 2.05). The samples exhibit a weak negative correlation between Eu and both Zr and Th supporting the diagenetic origin of Eu.

## References

- Allan, J.A. (1989): Water resource evaluation and development in Libya 1969–1989. *Libyan Studies*; 20: 235-242
- Al Shariani, T.A.K. (2006): Composition and environmental geochemistry of sediment encroachment controlled by dams in the United Arab Emirates. PH.D. Thesis. Cairo Univ., Cairo, Egypt.
- Anderson, D. (2003): Introduction to heavy metal monitoring. Natural Environmental Research Council. CEH. 1p.
- Anderson, R.; Bacon, M.P. and Brewer, P.G. (1983): Removal of  $^{230}\text{Th}$  and  $^{234}\text{Pb}$  at ocean margins. *Earth and Planetary Science Letters*; 66: 73-90.
- Anketell, J.M. and Ghellali, S.M. (1987): Stratigraphic aspects of the Gargaresh Formation, Tripolitania, NW Libya. *Libyan studies*; 18: 115-127.
- Anketell, J.M. and Ghellali, S.M. (1991): The Jifarah Formation – Aeolian and fluvial deposits of Quaternary age, Jifarah plain. In (Salem, M. J. and Belaid, M. N. editors): *The Geology of Libya, V: 1967-2013*.
- Armstrong-Altrin, J.S.; Verma, S.P.; Madhavaraju, J.; Lee, Y.I. and Ramasamy, S. (2003): Geochemistry of Upper Miocene Kudankulam Limestones, Southern India. *International Geological Review*; 45: 16-26.
- Asiedu, D.K.; Suzuki, S.; Nogami, K. and Shibata, T. (2000): Geochemistry of Lower Cretaceous sediments, Inner Zone of Southwest Japan: Constraints on provenance and tectonic environment. *Geochemical Journal*; 34: 155-173.
- Baair, M.Y.; Rabti, I.; Johnson, B. Miladi, N, N. and Swire, P. H. (2000): The regional geology of the Northwestern edge of the Sirt Basin. *The geology of north*

west Libya .Volume 1. Second Symposium on the Sedimentary Basins of Libya, held in Tripoli; pp.14, 15.

Bao, Z. and Zhao, Z. (2008): Geochemistry of mineralization with exchangeable REY in the weathering crusts of granitic rocks in South China. *Ore Geology Reviews*; 33: 519–535.

Barnes, U.C. and Cochran, J.R. (1990): Uranium removal in oceanic sediments and the oceanic U balance. *Earth and Planetary Science Letters*, 97: 94-101.

Bellanca, A.; Masetti, D. and Neri, R. (1997): Rare earth elements in limestone/marlstone couplets from the Albian-Cenomanian Cismon section (Venetian region, northern Italy): assessing REE sensitivity to environmental changes. *Chemical Geology*; 141: 141-152.

Burollet, P.F. (1960): *Lexique Stratigraphique International, Afrique. Fasc. Libye*, Centre Nat. de la Rech. Sci., pp. 1-62, Paris.

Carranza-Edwards, A.; Kasper-Zubillaga, J.J.; Rosales-Hoz, L.; Morales-de la Garza, E.A. and Lozano-Santa Cruz, R. (2009): Beach sand composition and provenance in a sector of the southwestern Mexican Pacific. *Revista Mexicana de Ciencias Geológicas*; 26(2): 433-447.

Chandrajith, R.; Dissanayake, C.B. and Tobschall, H.J. (2000): Enrichment of high-field strength elements in stream sediments of a granulite terrain in Sri Lanka-evidence for a mineralized belt. *Chem. Geol*; 175: 259-271.

Condie, K.C. (2005): High field strength element ratios in Archean basalts: a window to evolving sources of mantle plumes. *Lithos*; 79: 491-504.

Condie, K.C.; Boryta, M.D.; Liu, J. and Quian, X., (1992): The origin of khondalites: geochemical evidence from the Archean to Early Proterozoic granulitic belt in the North China Craton: *Precambrian Research*; 59(3-4), 207-223.

Cox, R.; Low, D.R. and Cullers, R.L. (1995): The influence of sediment recycling and basement composition on evolution of mudrock chemistry in the southwestern United States. *Geochimica et Cosmochimica Acta*; 59: 2919–2940.

De Baar, H.J.W.; German, C.G.; Elderfield, H. and van Gaans, P. (1988): Rare earth elements distributions in anoxic waters of the Cariaco Trench. *Geochimica et Cosmochimica Acta*; 52: 1203-1219.

De Baar, H.J.W.; Schijf, J. and Byrne, R.H. (1991): Solution chemistry of the rare earth elements in seawater. *European Journal of Solid State Inorganic Chemistry*; 28: 357-373.

Dunham, R.J. (1962): Classification of carbonate rocks according to depositional texture. In: *Classification of carbonate rocks* (Ed. by W.E. Ham), pp. 108-121. *Mem. Am. Ass. Petrol. Geol.* 1, Tulsa.

Elderfield, H. (1988): The oceanic chemistry of the rare earth elements. *Philosophical Transactions of the Royal Society of London.* A325: 105-126.

Elderfield, H.; Upstill-Goddard and R., Sholkovitz, E.R. (1990): The rare earth elements in rivers, estuaries and coastal seas and their significance to the composition of ocean waters. *Geochimica et Cosmochimica Acta*; 54: 971-991.

El Hinnawy, M. and Cheshitev G. (1975): Geological Map of Libya; 1:250 000 Sheet: Tarabulus NI 33-13. Explanatory Booklet. Ind. Res. Cent., Tripoli, 65p.

El Hinnawy, M. and Cheshitev, G. (1975): Geologic map of Libya, 1:250000 sheet Al Khums NI 33-14. Explanatory Booklet. Ind. Res. Cent., Tripoli, 65p.

El-Kammar, A.M.; Arafa, I.H. and El-Sheltami, O.R. (2007): Mineral composition and environmental geochemistry of the beach sediments along the eastern side of the Gulf of Suez, Egypt. *Journal of African Earth Sciences*; 49: 103–114.

Fedo, C.M.; Eriksson, K. and Krogstad, E.J. (1996): Geochemistry of shale from the Archean (~ 3.0 Ga) Buhwa Greenstone belt, Zimbabwe: Implications for

provenance and source area weathering. *Geochimica et Cosmochimica Acta*; 60(10): 1751-1763.

Feng, J.L. (2011): Trace elements in ferromanganese concretions, gibbsite spots, and the surrounding terra rossa overlying dolomite: Their mobilization, redistribution and fractionation. *Geochemical Exploration*; 108: 99-111.

Francis, M. and Issawi, B. (1977): Geological Map of Libya; 1:250,000 sheet: Soluq NI 34-2. Explanatory Booklet, Ind. Res. Centre, Tripoli. 86pp.

Gandhi, M.S. and Raja, M. (2014): Heavy mineral distribution and geochemical studies of coastal sediments between Besant Nagar and Marakkanam, Tamil Nadu, India. *Journal of Radiation Research and Applied Sciences*; 7: 256-268.

Garcia, D.; Fonteilles, M. and Moutte, J. (1994): Sedimentary fractionations between Al, Ti, and Zr and the genesis of strongly peraluminous granites. *J. Geol.*; 102: 411–422.

German, C.R.; Holliday, B.P. and Elderfield, H. (1993): A geochemical study of metalliferous sediment from the TAG hydrothermal mound, 26°08' N, Mid-Atlantic ridge. *Journal of Geophysical Research*; 98: 9683-9692.

Giglia, G. (1984): Geological Map of Libya; 1:250,000 sheet: Ajdabiya NH 34-6. Explanatory Booklet, Ind. Res. Centre, Tarabulus. 93pp.

Goudarzi, G.H. (1970): Geology and mineral resources of Libya-A reconnaissance. *Geol. Surv. Prof. Paper 660*, 104 p., Washington.

Greaves, M.J.; Elderfield, H. and Sholkovitz, E.R. (1999): Aeolian sources of rare earth elements to the Western Pacific Ocean. *Marine Chemistry*; 68: 31-38.

Gregor, R.B.; Pingitore, N.J. and Lyle, F. (1997): Strontianite in coral skeletal aragonite. *Science*; 275: 1452–1454.

Hallberg, R.O. (1976): A geochemical method for investigation of palaeoredox conditions in sediments: *Ambio*, Special Report; 4: 139-147.

Hammuda, O.S. (2000): Mesozoic and Cenozoic history of the Jifarah Arch, NE Libya and SE Tunisia. The geology of north west Libya .Volume 1. Second Symposium on the Sedimentary Basins of Libya, held in Tripoli; pp. 41, 42, 44.

Hlal, O. and Bennur, S. (2014): Sedimentology and stratigraphy architecture of the late Pleistocene-Holocene succession of the Gargaresh Formation, Subratah Basin, NW Libya. *Geophysical Research Abstracts*; Vol. 16, EGU2014-14321.

Itoh, A.; Hamanaka, T.; Rong, W.; Ikeda, K.; Sawatari, H.; Chiba, K. and Haraguchi, H. (1999): Multielement determination of rare earth elements in geochemical samples by liquid chromatography/inductively coupled plasma mass spectrometry. *Anal. Sci.*; 15: 17–22.

Jones, B. and Manning, D.C. (1994): Comparison of geochemical indices used for the interpretation of paleo-redox conditions in Ancient mudstones: *Chemical Geology*; 111(1-4): 111-129.

Katongo, C.; Koeberl, C.; Witzke, B.J.; Hammond, R.H. and Anderson, R.R. (2004): Geochemistry and shock petrography of the Crow Creek Member, South Dakota, USA: Ejecta from the 74-Ma Manson impact structure. *Meteoritics and Planetary Science*; 39(1): 31–51.

Khomiara, S.B.A. (2013): Geological studies on the Quaternary coastal deposits between Tripoli and Musrata, Libya. PH.D. Thesis. Mansoura University, Mansoura, Egypt.

Klen, L. (1974): Geological map of Libya, 1:250000 sheet Benghazi NI 34-14, Explanatory Booklet, Indust. Res. Cent., Tripoli, p 56.



Klinkhammer, G.P.; Elderfield, H. and Hudson, A. (1983): Rare earth elements in seawater near hydrothermal vents. *Nature*; 305: 185-188.

Kurian, S.; Nath, B.N.; Ramaswamy, V.; Naman, D.; Gnaneshwar Rao; Kamesh Raju, K.A.; Selvaraj, K. and Chen, C.T.A. (2008): Possible, detrital, diagenetic and hydrothermal sources for Holocene sediments of the Andaman backarc basin. *Marine Geology*; 247: 178-193.

Lipparini, T. (1940): Tettonica e Geomorfologia della Tripolitania. *Boll. Soc. Geol. Ital.*, Vol. LIX, pp. 221-301, Roma (English translation: *Tectonics and Geomorphology*. Min. of Industry, Geol. Sec. Bull., No. 4. 1968).

Liu, Y.G.; Miah, M.R.U. and Schmitt, R.A. (1988): Cerium: a chemical tracer for paleo-oceanic redox conditions. *Geochimica et Cosmochimica Acta*; 52: 1361-1371.

Lopez, J.M.G.; Bauluz, B.; Fernández-Nieto, C. and Oliete, A.Y. (2005): Factors controlling the trace-element distribution in fine-grained rocks: the Albian kaolinite-rich deposits of the Oliete Basin (NE Spain). *Chemical Geology*; 214 (1-2, 3): 1-19.

MacLeod, K.G. and Irving, A.J. (1996): Correlation of cerium anomalies with indicators of paleoenvironment. *Sedimentary Research*; 66: 948-955.

MacRae, N.D.; Nesbitt, H.W. and Kronberg, B.I. (1992): Development of a positive Eu anomaly during diagenesis. *Earth and Planetary Science Letters*; 109: 585-591.

Madhavaraju, J.; Gonzalez-Leon, C.M.; Lee, Y.I.; Armstrong-Altrin, J.S. and Reyes-Campero, L.M. (2010): Geochemistry of the Mural Formation (Aptian-Albian) of the Bisbee Group, Northern Sonora, Mexico. *Cretaceous Research*; 31: 400-414.

Madhavaraju, J. and Gonzalez-Leon, C.M. (2012): Depositional conditions and source of rare earth elements in carbonate strata of the Aptian-Albian Mural

Formation, Pitaycachi section, northeastern Sonora, Mexico. *Revista Mexicana de Ciencias Geológicas*; 29(2): 478-491.

Madhavaraju, J. and Lee, Y.I. (2009): Geochemistry of the Dalmiapuram Formation of the Uttatur Group (Early Cretaceous), Cauvery basin, southeastern India: Implications on provenance and paleo-redox conditions. *Revista Mexicana de Ciencias Geológicas*; 26(2): 380-394.

Madhavaraju, J. and Ramasamy, S. (1999): Rare earth elements in limestones of Kallankurichchi Formation of Ariyalur Group, Tiruchirapalli Cretaceous, Tamil Nadu: *Journal of the Geological Society of India*; 54: 291-301.

Malick, B.M.L. and Ishiga, H. (2015): Geochemical maturity of pocket beach sands from the Sanin region of southwest Japan. *Earth Science Research*; 4(2): 45-61.

Masuzawa, T. and Koyama, M. (1989): Settling particles with positive Ce anomalies from the Japan Sea. *Geophysical Research Letters*; 16: 503-506.

McLennan, S.M.; Hemming, S.; McDaniel, D.K. and Hanson, G.N. (1993): Geochemical approaches to sedimentation, provenance, and tectonics, in Johnson, M.J., Basu, A. (eds.), *Processes Controlling the Composition of Clastic Sediments*: Geological Society of America, Special Paper; 284: 21-40.

Michard, A.; Albarede, F.; Michard, G.; Minister, J.F. and Charlow, J.L. (1983): Rare earth elements and uranium in high temperature solutions from East-Pacific rise hydrothermal vent field (13°N): *Nature*; 303: 795-797.

Mijalkovic, N. (1977): *Geological Map of Libya*; 1:250,000 sheet: Al Qaddahiyah NH 33-3. Explanatory Booklet, Ind. Res. Centre, Tripoli. 66 pp.

Nagarajan, R.; Madhavaraju, J.; Nagendra, R.; Armstrong-Altrin, J.S. and Moutte, J. (2007): Geochemistry of Neoproterozoic shales of the Rabanpalli Formation, Bhima Basin, Northern Karnataka, southern India: implications for provenance and paleoredox conditions. *Revista Mexicana de Ciencias Geológicas*; 24 (2): 150-160.

Nath, B.N.; Bau, M.; Ramlingeswara-Rao, B. and Rao, C.M., (1997): Trace and rare earth elemental variation in Arabian Sea sediments through a transect across the oxygen minimum zone. *Geochimica et Cosmochimica Acta*; 61: 2375-2388.

Nath, B.N.; Roelandts, I.; Sudhakar, M. and Plueger, W.L. (1992): Rare earth element patterns of the Central Indian Basin sediments related to their lithology. *Geophysical Research Letters*; 19: 1197-1200.

Nothdurft, L.D.; Webb, G.E. and Kamber, B.S. (2004): Rare earth element geochemistry of Late Devonian reefal carbonates, Canning Basin, Western Australia: Confirmation of seawater REE proxy in ancient limestones. *Geochimica et Cosmochimica Acta*; 68: 263-283.

Papadopoulos, A.; Christofides, G.; Pe-Piper, G.; Koroneos, A. and Papadopoulou, L. (2015): Geochemistry of beach sands from Sithonia Peninsula (Chalkidiki, Northern Greece). *Mineralogy and Petrology*; 109: 53-66.

Parkman, R.H.; Charnock, J.M. and Livens, F.R. (1998): A study of the interaction of strontium ions in aqueous solution with the surfaces of calcite and kaolinite. *Geochim Cosmochim Acta*; 62(9): 1481-1492.

Piper, D.Z. (1974): Rare earth elements in the sedimentary cycle. *Chemical Geology*; 14: 285-304.

Preda, M. and Cox, M.E. (2005): Chemical and mineralogical composition of marine sediments, and relation to their source and transport, Gulf of Carpentaria, Northern Australia. *Marine Systems*; 53: 169– 186.

Quinby-Hunt, M.S.; Wilde, P. and Berry, W.B.N. (1991): The provenance of low-calcic black shales. *Mineralium Deposita*; 26: 113–121.

Rohlich, P. (1974): Geological Map of Libya; 1:250,000 sheet: Al Bayda NI 34-15. Explanatory Booklet, Ind. Res. Centre, Tripoli. 70 pp.

Shaltami, O.R. (2012): Mineral composition and environmental geochemistry of the beach sediments along the Mediterranean Coast from Benghazi to Bin Jawwad, Northeast Libya. PH.D. Thesis. Cairo Univ. Cairo, Egypt.

Shaltami, O.R. (2015): Geochemistry of the Shahat Marl Member, Wadi Az Zad, Al Jabal Al Akhdar, NE Libya. *Arabian Journal of Earth Sciences*; 2(3): 23-39.

Sholkovitz, E.R.; Landing, W.M. and Lewis, B.L. (1994): Ocean particle chemistry: the fractionation of rare earth elements between suspended particles and seawater. *Geochimica et Cosmochimica Acta*; 58: 1567-1579.

Taylor, S.R. and McLennan, S.M. (1985): *The Continental Crust: its composition and evolution*. Blackwell Scientific Publishers, Oxford.

Veizer, J. (1983): Trace elements and isotopes in sedimentary carbonates, in Reeder, R.J. (ed.), *Carbonates: Mineralogy and Chemistry: U.S.A*, Mineralogical Society of America, *Reviews of Mineralogy*; 11: 265-299.

White, W. M. (2001): *Geochemistry: An on-line textbook*. John-Hopkins University Press, 700 p.

Whittaker, S.G. and Kyser, T.K. (1993): Variations in the neodymium and strontium isotopic composition and REE content of molluscan shells from the Cretaceous Western Interior Seaway. *Geochimica et Cosmochimica Acta*; 57: 4003-4014.

Zhang, K.J. (2004): Secular geochemical variations of the Lower Cretaceous siliciclastic rocks from central Tibet (China) indicate a tectonic transition from continental collision to back-arc rifting. *Earth and Planetary Science Letters*; 229: 73- 89.